From bubbles and filaments to cores and disks: gas gathering and growth of structure leading to the formation of stellar systems

Jaime E. Pineda, Doris Arzoumanian, Philippe André, Rachel K. Friesen, Annie Zavagno, Seamus D. Clarke, Tsuyoshi Inoue, Che-Yu Chen, Yueh-Ning Lee, Juan D. Soler, et al.

From Bubbles and Filaments to Cores and Disks: Gas Gathering and Growth of Structure Leading to the Formation of Stellar Systems

Jaime E. Pineda[1], **Doris Arzoumanian**[2,3], **Philippe André**[4], **Rachel K. Friesen**[5], **Annie Zavagno**[3], **Seamus D. Clarke**[6], **Tsuyoshi Inoue**[7], **Che-Yu Chen**[8], **Yueh-Ning Lee**[9], **Juan D. Soler**[10], **Michael Kuffmeier**[11]

[1]*Max-Planck-Institut für extraterrestrische Physik,*[2]*National Astronomical Observatory of Japan,* [3]*Aix-Marseille Université & IUF,* [4]*CEA Paris-Saclay,* [5]*University of Toronto,* [6]*Academia Sinica Institute of Astronomy and Astrophysics,* [7]*Konan University,* [8]*Lawrence Livermore National Laboratory,* [9]*National Taiwan Normal University,* [10]*Max Planck Institute for Astronomy,* [11]*University of Virginia*

Abstract The study of the development of structures on multiple scales in the cold interstellar medium has experienced rapid expansion in the past decade, on both the observational and the theoretical front. Spectral line studies at (sub-)millimeter wavelengths over a wide range of physical scales have provided unique probes of the kinematics of dense gas in star-forming regions, and have been complemented by extensive, high dynamic range dust continuum surveys of the column density structure of molecular cloud complexes, while dust polarization maps have highlighted the role of magnetic fields. This has been accompanied by increasingly sophisticated numerical simulations including new physics (e.g., supernova driving, cosmic rays, non-ideal magneto-hydrodynamics, radiation pressure) and new techniques such as zoom-in simulations allowing multi-scale studies. Taken together, these new data have emphasized the anisotropic growth of dense structures on all scales, from giant ISM bubbles driven by stellar feedback on ∼50–100 pc scales through parsec-scale molecular filaments down to < 0.1 pc dense cores and < 1000 au protostellar disks. Combining observations and theory, we present a coherent picture for the formation and evolution of these structures and synthesize a comprehensive physical scenario for the initial conditions and early stages of star and disk formation.

1. INTRODUCTION

Studying the growth of structures on multiple scales in the cold interstellar medium (ISM) is crucial for improving our understanding of the general inefficiency of the star formation process, the origin of the stellar initial mass function (IMF), and ultimately the birth of protoplanetary disks. This field of research has thrived in the past decade, thanks to both high dynamic range observations and multi-scale numerical simulations. In particular, spectral line studies at (sub-)millimeter wavelengths over a wide range of physical scales with, e.g., GBT and ALMA, have provided unique probes of the kinematics of dense gas in star-forming regions, complementing deep, extensive dust continuum surveys of the column density structure of molecular cloud complexes with, e.g., *Herschel*. Dust polarization maps from *Planck* and JCMT have also highlighted the role of magnetic fields. With theoretical support from advanced numerical models, we review how these newly-acquired observations of gas structure and dynamics impact our understanding of the physics of star formation. Taken together, the new data enabled the community to establish clear physical connections between a broad hierarchy of cold interstellar structures ranging from giant ISM bubbles driven by stellar feedback on ∼50–100 pc scales (Sect. 2) through parsec-scale molecular filaments (Sect. 3) down to < 0.1 pc dense cores (Sect. 4) and < 1000 au protostellar disks (Sect. 5). The observational results emphasize the anisotropic growth of dense structures on all scales, with shell-like accretion of gas from bubbles to filaments (Sects. 2 and 3), axial contraction from filaments to cores (Sects. 3 and 4), followed by non-axisymmetric accretion through streamers from cores to disks (Sect. 5). We follow the flow of material throughout the different levels of the ISM hierarchy, with each level accreting from its parent level and funnelling material to its sub-level. While each level in the hierarchy is interconnected in this way, different geometries and physical processes dominate on each size scale, meaning that there exists a partial decoupling between consecutive levels. It is therefore productive to discuss each level separately as a set of discrete structural entities. The chapter sections follow the flow of dense gas from large to small scales, or from bubbles to disks. To conclude the chapter, we synthesize a comprehensive updated paradigm for the initial conditions and early stages of star and disk formation.

2. INTERSTELLAR BUBBLES AND THEIR CONNECTIONS TO THE FORMATION OF FILAMENTARY STRUCTURES

The cold interstellar medium is observed to be organized in bubbles and filamentary structures. Interstellar bubbles

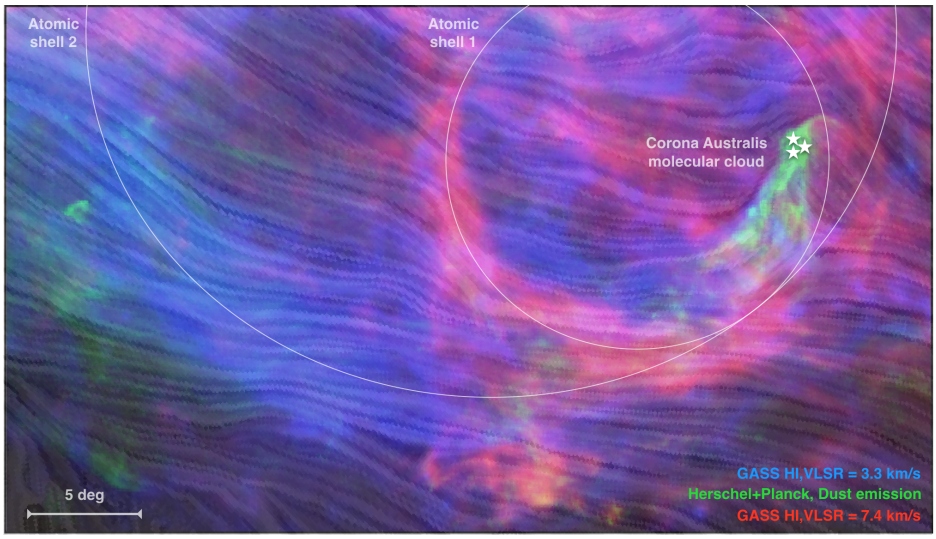

Fig. 1.— Colour composite image showing the HI emission at 7.4 $\mathrm{km\,s^{-1}}$ (red) and at 3.3 $\mathrm{km\,s^{-1}}$ (blue) and the column density map derived from combined *Herschel+Planck* data (green). The white circles trace the two HI shells associated with the CrA molecular cloud traced in green. The magnetic field structure derived from *Planck* polarization observations is shown as a drapery pattern (from *Bracco et al.* 2020a). The 5 deg scale corresponds to 13 pc at the 150 pc distance of the CrA cloud.

of both neutral and ionized gas are associated with high-mass stars at different phases of their evolution. The expanding nature of these bubbles shapes the surrounding medium and possibly plays a role in the formation and evolution of interstellar filaments. In this section we present recent observations of both neutral and ionized bubbles and their relationship with filamentary structures identified in atomic and molecular clouds. We then review existing theories of filament formation and discuss the important role of expanding bubbles in the formation process of molecular filaments in shock-compressed layers.

2.1. Observations of Bubbles and Filamentary Structures in the Interstellar Medium

2.1.1. Observations of Bubbles and their Relation with the Local Interstellar Medium

In our Galaxy, bubbles of both neutral and ionized gas are ubiquitously observed. The expanding nature of bubbles, with velocities ∼5–20 $\mathrm{km\,s^{-1}}$ (*Spitzer* 1978), means that bubbles may sweep up and gather diffuse gas and participate in the formation of new dense filamentary structures, but may also compress or disrupt existing structures. It is important to note that the neutral and ionized bubbles have markedly different origins and also affect different size scales. We present recent observations and description of the two types of bubbles below.

HI shells, observed in 21 cm HI atomic emission (*Daigle et al.* 2007; *Ehlerová and Palouš* 2013), are generated mainly by supernovae or multiple HII regions and result from the expansion, recombination, and cooling of the hot and ionized expanding gas (*Tomisaka et al.* 1981). HI supershells interact with the ISM at large-scales (∼100 pc) and can drive strong large-scale compressive flows, which has been observationally suggested to help the formation of molecular gas (*Ehlerová and Palouš* 2016; *Robitaille et al.* 2018). In the early 90's, HI filaments and arcs delineating the Orion-Eridanus bubble were observed, and they suggested a relation between the wind-blown bubble and the form and structures of the surrounding medium (*Brown et al.* 1995). The spatial distribution of CO clumps, correlated with and observed in excess toward the walls of HI shells, reinforces the idea of the role of HI shells in the formation (and shaping) of molecular clouds (*Dawson et al.* 2008). Recent observations support a scenario of filamentary molecular cloud formation triggered by supersonic compression of cold magnetized HI gas from at least two expanding bubbles (*Bracco et al.* 2020a, see Fig. 1). The formation of many nearby molecular clouds may have been driven by the expansion of the Local Bubble resulting from multiple supernova explosions (**?**).

HII regions, detected in Hα, infrared, and/or radio emission, interact with the nearby matter of the parental cloud (∼1–5 pc scales) and trace the present-time stellar feedback due to stellar winds, ionizing radiation, and outflows of massive stars. The *Herschel* far-infrared survey of the Galactic Plane, Hi-GAL (*Molinari et al.* 2010), clearly reveals the importance of ionized bubbles and their key role in shaping their surrounding material and influencing subsequent star formation (*Palmeirim et al.* 2017) and especially the formation of new generations of high-mass stars (as shown by *Zhang et al.* 2020b, 2021). HII regions are observed to be surrounded by dense molecular gas. The interaction between possibly pre-existing dense molecular gas and the expansion of HII regions is revealed by the variation of the abundance ratio of CO isotopologues (^{13}CO/C^{18}O) that results from the selective photodissociation by the FUV radiation from embedded OB stars, since this variation can-

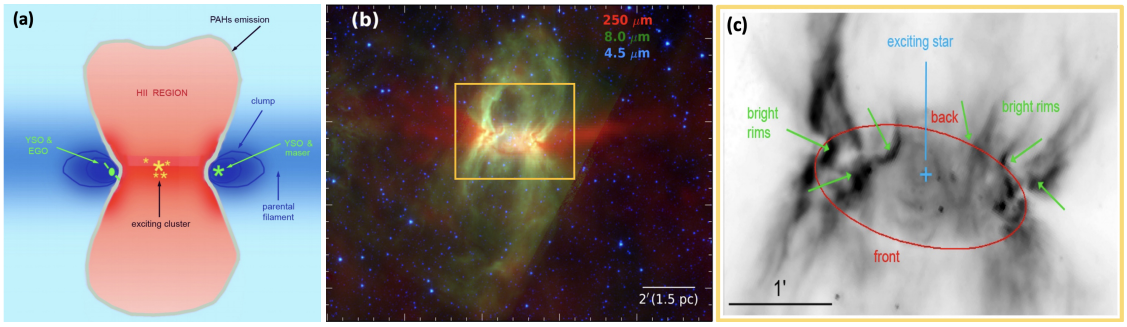

Fig. 2.— **a)** Illustration of a generic bipolar HII region and its environment. The ionized gas, the molecular gas, and the PAH emission of the PDR are shown in red, blue, and grey, respectively. **b)** Composite image of G319.88 + 00.79, which is an observed example of a bipolar HII region. **c)** Centre of G319.88 + 00.79 at 8.0 μm showing the dense waist of the nebula (detected in absorption) the bright rims, and the position of the exciting star. Panels a, b, and c are adapted from *Deharveng et al.* (2015) and *Samal et al.* (2018).

not be explained solely by the effect of the interstellar radiation field (*Shimajiri et al.* 2014; *Areal et al.* 2019).

The impact of ionized regions on their surrounding medium strongly depends on the evolutionary stage of the ionized region, the ionized gas geometry, and the original configuration of the molecular gas that gave birth to the ionizing stars (see Fig. 2). Classical ionized regions (Strömgren spheres) collect their surrounding material between their expanding ionization front and the shock front that precedes it into the surrounding neutral medium. Compression of the surrounding medium by the ionized region is accompanied by a local density increase and by the formation of filamentary structures (see Fig. 3). Ionized regions might also expand in a pre-existing filamentary medium and play a role in compressing the already formed filaments, dispersing them or preventing their dispersion (*Xu et al.* 2018). There are examples of bipolar HII regions (see Fig. 2) where the ionizing stars form in and impact the parental sheet-like filamentary molecular cloud (*Xu et al.* 2017), which itself have been formed at the edge of an expanding HI shell. Hub-filament systems, which are centrally converging networks of filaments into high density hubs, have been proposed to be the main sites of star-clusters and high-mass star formation (*Myers* 2009; *Baug et al.* 2018; *Williams et al.* 2018; *Kumar et al.* 2020; *Dewangan* 2021; *Liu et al.* 2021). The hub-filament configuration may allow the ionizing pressure and radiation from the high-mass stars formed in the hub to escape through the inter-filamentary gaps, while dense material continues flowing along the filaments onto the hub. These flows replenish the hub with matter allowing the formation of massive clusters and high-mass stars (*Kumar et al.* 2020, 2022). At an evolved stage, the parental filamentary cloud is always observed to be associated with the particular morphology of a bipolar ionized region. The waist of these bipolar regions hosts young and active high-mass star formation (see Fig. 2), possibly as a direct consequence of the ionized region expansion in the parental filaments (*Deharveng et al.* 2015; *Samal et al.* 2018). In other cases, HII regions are observed to expand into filamentary molecular clouds but the ionizing stars are not observed to be directly associated with the presently observed dense molecular material. This is the case, for example, of the RCW 120 HII region (see Fig. 3 and *Zavagno et al.* 2010, 2020). These different configurations of the matter structure and of the local density of the material associated with the ionizing star may be linked to the evolutionary stage of the expanding HII region and of the star formation event (*Kumar et al.* 2020).

These observations pose the question of the *original* density distribution of the surrounding material prior to both HI and HII bubbles' expansion. If the material is organized into filaments from its origin, the bubble's expansion may mostly have a shaping role and be probably in turn shaped by the filamentary structures (e.g., in hub-filament systems as explained above); whereas if the material is not filamentary at its origin, then the bubble's expansion can have a direct role in the formation of filaments.

2.1.2. *Observations of the Filamentary Interstellar Medium*

Both the atomic and molecular phases of the Galactic ISM are observed to be filamentary (e.g., *McClure-Griffiths et al.* 2006; *Clark et al.* 2014; *Ragan et al.* 2014; *Mattern et al.* 2018). In the diffuse atomic ISM, some of these filamentary structures correspond to elongated structures "crawling away from the Galactic plane" (*Heiles* 1984) or parallel to the Galactic plane (*Soler et al.* 2020). Others are hair-like extended structures aligned with the interstellar magnetic field (*Clark et al.* 2014; *Kalberla et al.* 2016). Some of these structures are probably embedded in a warm ionized medium, as suggested by their correlation with radiopolarimetry observations (*Kalberla et al.* 2017; *Bracco et al.* 2020b). More descriptions on current filament identification and characterizing methods are presented in Sect. 4.2.1.

As for the molecular ISM, it is comprised of complex filamentary networks (see review in *André et al.* 2014) from large to small scales in a diversity of environments. On average, ∼15% of the total mass of molecular clouds is observed to be in the form of molecular filaments, while up to ∼60–90% of the dense gas mass (defined as the mass of gas with column density $N_{\rm H_2} > 7 \times 10^{21}\,{\rm cm}^{-2}$) is in the form of filaments (*Arzoumanian et al.* 2019; *Roy et al.*

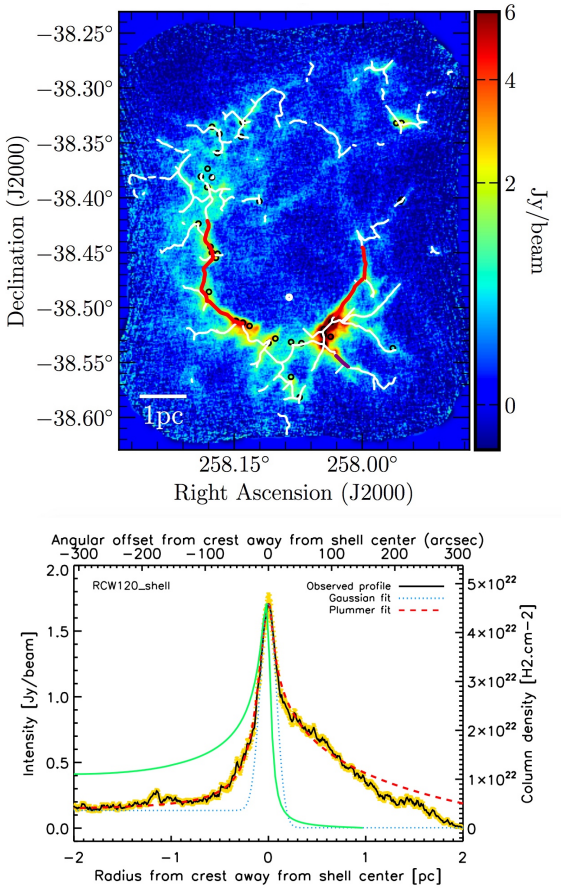

Fig. 3.— Top: Combined ArTéMiS+*Herschel*-SPIRE 350 μm map of the HII region RCW 120. The crests of the filaments are overlaid in white. The black circles show the *Herschel* young sources. The white circle shows the location of the ionizing star. Bottom: The observed mean radial column density profile (black curve) of the RCW 120 dense shell (measured across and averaged along the crest shown in red in the top panel), with positive offsets going away from the shell center. The Gaussian fit (blue dotted curve) and the Plummer fit (red dashed curve) are shown. The green full line shows the profile expected for a spherical shell, which does not reproduce well the observations. This suggests that RCW 120 might be a 3D ring, rather than a spherical structure (from *Zavagno et al.* 2020).

2019; *Kumar et al.* 2022). In the literature, various names have been used to describe the multitude of filaments observed at different scales and using different tracers. These different types of filamentary structures are discussed in detail by Hacar *et al.* in this volume. At scales $\gtrsim$ 10 pc and distances $\gtrsim$ 1 kpc, filamentary structures have been referred to as giant molecular filaments (e.g., *Ragan et al.* 2014) or Galactic bones (e.g., *Goodman et al.* 2014; *Zucker et al.* 2015), including (collections of) extraordinarily elongated infrared dark clouds (IRDCs). At scales of $\sim$1–10 pc and at distances of $\lesssim$1 kpc, the term of interstellar or molecular filaments has mostly been used (e.g., *André et al.* 2014; *Arzoumanian et al.* 2019). Molecular filaments as traced in the dust continuum may further break down into filamentary substructures in position-position-velocity space when observed in emission from molecular lines. These velocity-coherent substructures are sometimes termed fibers when they are filamentary and overlapping in projection (*Hacar et al.* 2013, 2018).

Filaments are not isolated objects, but are observed to form systems with multiple junctions and intersections. These systems may be identified as: 1) ridge–filament systems when side-filaments are connected from the side to a (usually denser and more massive) star-forming main-filament sometimes referred to as a "ridge" (e.g., *Hennemann et al.* 2012), or 2) hub–filament systems when multiple filaments join from various directions into a hub (e.g., *Myers* 2009; *Kirk et al.* 2013a; *Peretto et al.* 2014, see also Sect. 2.1.1). Some side-filaments are star-forming (as in, e.g., the DR21 filament system, *Hennemann et al.* 2012), while others, similar to HI filaments, are magnetically-aligned thin, hair-like linear structures, referred to as "striations" (*Goldsmith et al.* 2008; *Palmeirim et al.* 2013; *Cox et al.* 2016; *Malinen et al.* 2016). When observations of the velocity field are available, side-filaments appear to be channels of gas flows feeding a main-filament (see reviews in *André et al.* 2014; *Motte et al.* 2018, or see e.g., *Williams et al.* 2018; *Treviño-Morales et al.* 2019; *Chen et al.* 2020a; *Liu et al.* 2021 for more recent observations). Indeed, the physical intersections between filaments usually exhibit multiple velocity components, which trace the individual velocities of each of the merging filaments.

Most of these different filament names are based on the apparent morphology of the systems, and are not well defined in terms of measurable physical properties such as mass per unit length (or line mass, denoted by M/L or $M_{\rm line}$). Nevertheless, filaments with line masses below and above the thermal value of the critical mass per unit length $M_{\rm line,crit} = 2\,c_s^2/G$ (e.g., *Ostriker* 1964) are usually called thermally subcritical and thermally supercritical, respectively (e.g., *André et al.* 2014, see also *Arzoumanian et al.* 2019 and Sect. 3.3 below for a refined classification based on $M_{\rm line}$). The term 'striations' is typically used to refer to fainter subcritical structures aligned with the magnetic field, while filaments, filamentary substructures, (molecular) fibers, and side-filaments are generally indistinguishable in terms of their line mass and other properties.

2.2. Theoretical Models of Filament Formation

The expansion of bubbles compresses the ISM, which drives not only the evolution of the diffuse ISM into cold HI and molecular clouds, but also induces filament formation in the compressed molecular cloud (*Inutsuka et al.* 2015). *Ntormousi et al.* (2011) demonstrated that collisions of super-bubbles triggers the formation of highly structured filamentary molecular gas ($\sim$100 cm^{-3}). Recent kpc-scale galactic simulations allowed for bubble formation by including supernova explosions, radiation, and winds from massive stars, and concluded that bubbles are critical in

controlling the evolution of the ISM (e.g., *Padoan et al.* 2017; *Kim and Ostriker* 2018; *Rathjen et al.* 2021). Although large-scale simulations can capture the global ISM evolution, detailed processes of filament formation and evolution are often outside the resolvable scales. In the following, we focus on the formation of parsec-scale atomic and molecular filaments, which have more direct relations to star formation. In particular, the parsec scale studies of filamentary cloud formation by shock compression reported below describe the impact of expanding bubbles on the ISM.

2.2.1. *Overview of Recent Models for Filament Formation*

While several formation mechanisms have been proposed for different types of filaments, the fact that filamentary structures appear in both 2D and 3D simulations of clouds with or without turbulence, magnetic field, and/or self-gravity (e.g., *Inoue and Fukui* 2013; *Gómez and Vázquez-Semadeni* 2014; *Smith et al.* 2014; *Van Loo et al.* 2014; *Kirk et al.* 2015; *Federrath* 2016, also see review in *André et al.* 2014) renders the dominant mechanism for filament formation uncertain. In addition, filaments in simulations are often dynamic structures that are continuously evolving (*Smith et al.* 2014; *Li and Klein* 2019). This makes the characterization of filament properties in simulations challenging.

In the HI phase of the interstellar medium, it is generally recognized that filamentary structures are created in shock compressed layers (*Inoue and Inutsuka* 2009; *Heitsch et al.* 2009). In such layers, *Inoue and Inutsuka* (2016) showed that HI clouds created via shock induced thermal instability are stretched by turbulent shear flows along the magnetic field (see also *Hennebelle* 2013; *Soler and Hennebelle* 2017). The resulting filamentary HI clouds resemble the observed HI filaments (*Clark et al.* 2014).

In the denser regions of the ISM, molecular filaments have been considered to be the products of either direct compression by interstellar turbulence or gravitational fragmentation at the cloud scale (see review in *André et al.* 2014). The earliest models of filament formation often considered the semi-analytic fragmentation of sheet-like clouds due to gravitational instability (see references for the 'type-G' mechanism described in Sect. 2.2.2 below). It has also been shown that thermal instability in quiescent clouds can lead to the formation of clumpy and filamentary structures (*Wareing et al.* 2016, 2019).

With the advances in computational capability over the past decade, fully-3D simulations with prescribed turbulence have become the common approach to studying the formation and evolution of star-forming clouds. Simulations considering the evolution of individual clouds usually start with uniform gas in a cubic simulation box or as a spherical clump with scale-dependent velocity perturbation, and with either periodic or open boundary conditions (e.g., *Smith et al.* 2014; *Kirk et al.* 2015; *Li et al.* 2015; *Federrath* 2016). These simulations successfully produce filaments and show that filamentary structures are the inevitable outcome of cloud evolution. In the scenario of global hierarchical collapse (GHC; *Vázquez-Semadeni et al.* 2019), filaments are described as dynamic structures that continuously accrete from the ambient gas while feeding dense cores within them, with gravity being the main driving force of filament formation (see also *Gómez and Vázquez-Semadeni* 2014; *Naranjo-Romero et al.* 2015; *Vázquez-Semadeni et al.* 2017). Without invoking global gravitational collapse, the combination of large-scale compressive flows and local self-gravity can lead to similarly dynamic filaments continuously accreting and feeding their cores (see more details in Sect. 2.2.2 below).

As for the formation of the faint, thermally subcritical and periodically spaced linear striations often observed in the immediate surroundings of star-forming filaments (e.g., *Cox et al.* 2016; *Malinen et al.* 2016, see also a review in *André et al.* 2014), recent theoretical studies have proposed various scenarios. The models include anisotropy in magnetized turbulence (*Vestuto et al.* 2003; *Heyer et al.* 2008; *Xu et al.* 2019), density oscillations induced by MHD waves (*Heyer et al.* 2016; *Tritsis and Tassis* 2016; *Heyer et al.* 2020), and the corrugation of ultra-thin shock-compressed layers (*Chen et al.* 2017). Numerical simulations also suggest that striations could be more commonly present in star-forming clouds than what has been observed, because these faint structures are easily washed out due to projection overlapping (*Chen et al.* 2017; *Li and Klein* 2019).

2.2.2. *Anisotropic Filament Formation in Shock-compressed Layers*

With increasing observational evidences of the lack of symmetry between the plane-of-sky extent and the line-of-sight depth of molecular clouds (e.g., *Storm et al.* 2014; *Lee et al.* 2014b; *Arzoumanian et al.* 2018; *Shimajiri et al.* 2019a), it has been suggested that filaments form in sheet-like gas structures rather than from spherical gas clouds (*Heitsch* 2013a; *Chen and Ostriker* 2015; *Auddy et al.* 2016). Hence, simulations with convergent flows or colliding clumps that generate shock-compressed dense gas layers became an alternative way to numerically investigate the star formation process in the ISM (e.g., *Inoue and Fukui* 2013; *Gómez and Vázquez-Semadeni* 2014; *Chen and Ostriker* 2014, 2015; *Gong and Ostriker* 2015; *Wu et al.* 2017; *Inoue et al.* 2018). In this view, filament formation is still directly connected to shock compression but as a two-step process. Firstly, a large-scale shock wave (e.g. an expanding HI bubble) or a supersonic turbulent flow in the molecular cloud compresses the gas to form a dense layer (a 2D structure). String-like 1D filaments then form within this locally flat region via gas accretion in a preferred direction parallel to the shock-compressed layer (*Inoue et al.* 2018; *Chen et al.* 2020a).

In *Abe et al.* (2021), existing filament formation models associated with shock-compressed layers were classified into five types, as follows (see Fig. 4). **Type-C**: fil-

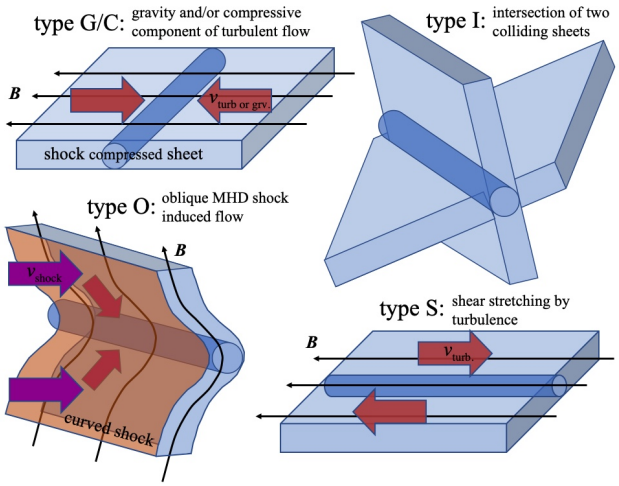

Fig. 4.— Schematics of the filament formation mechanisms, where the blue sheets are shock compressed layers in which filaments are formed, the black thin arrows represent the magnetic fields, and the thick arrows show the gas flow orientations.

ament formation induced by local velocity perturbations within shock-compressed layers (*Padoan and Nordlund* 1999; *Chen and Ostriker* 2014; *Gong and Ostriker* 2015). **Type-O**: Filaments formed at the convergent point of material flows within bent oblique MHD shock fronts induced by the clumpiness of the medium (*Inoue and Fukui* 2013; *Vaidya et al.* 2013). **Type-G**: Gravity-induced fragmentation of sheet-like clouds (*Tomisaka and Ikeuchi* 1983; *Nagai et al.* 1998; *Kitsionas and Whitworth* 2007). **Type-S**: Shear flows associated with turbulence stretching existing clumps, which become elongated structures (*Hennebelle* 2013; *Inoue and Inutsuka* 2016). Filaments formed in this way generally have small line-masses, like HI filaments. **Type-I**: Filaments formed at the intersection of two shock-compressed sheets (*Padoan and Nordlund* 1999; *Pudritz and Kevlahan* 2013; *Matsumoto et al.* 2015). This mode works only in highly super-Alfvénic or unmagnetized turbulence. Note that type-G filaments could also grow alongside type-C and type-O filaments within shock-compressed layers after a few free-fall times of the sheet formation, and gravity-induced accretion is also seen in type-C and type-O filaments, as described in the two-step, gravity-induced preferred-direction accretion picture by *Chen et al.* (2020a).

By performing MHD simulations of shock-compressed molecular clouds under various conditions (see e.g., top panel of Fig. 5), *Abe et al.* (2021) investigated which mechanism is primarily responsible for filament formation in shock compressed layers. They found that the type-O mechanism accounts for the majority of filament formation, when the velocity of the shock that compresses the molecular cloud is higher than $v_{\rm cr}$ $\sim$5 km s^{-1} (dependent on the density and magnetization level). At shock velocities lower than $v_{\rm cr}$, type-C becomes the dominant mechanism of filament formation. Because of this dependence on the shock velocity, the type-O mechanism creates more massive filaments than the type-C. Pure type-G filament formation can only be clearly seen when the initial structure of the molecular cloud is featureless (no initial density fluctuations and weak turbulence). It is important to note that while type-G formation is rarely dominant with realistic initial conditions, gravity-assisted accretion helps the growth of filaments formed via type-C/O and may collect separately-formed filaments into bundles. Type-S filaments appear everywhere due to turbulence, but filaments formed by shear motions do not become dense enough to form stars, and type-I is not clearly observed in a medium with a realistic magnetization level.

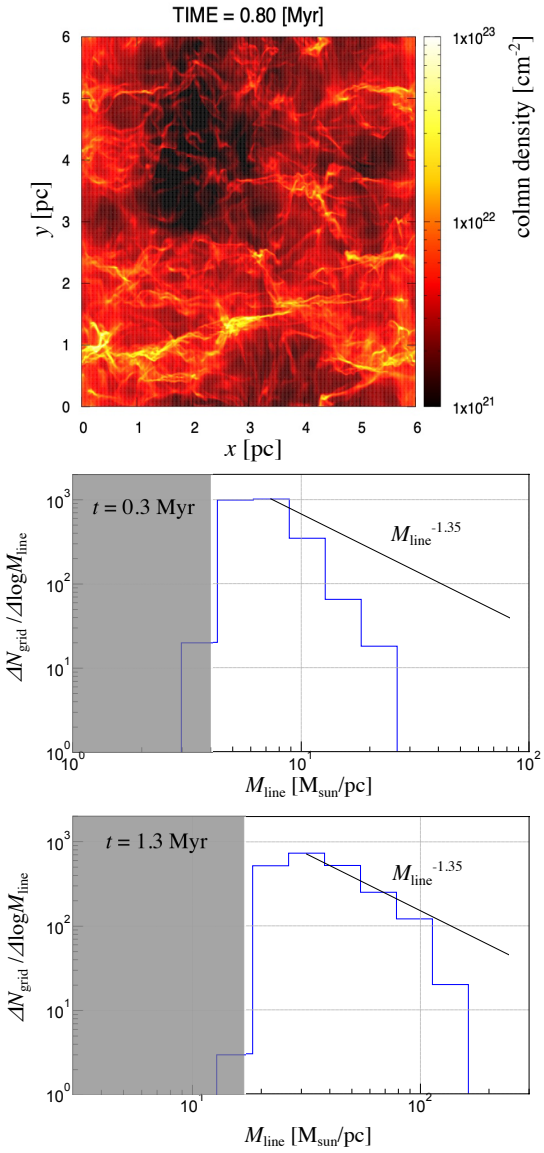

Fig. 5.— Top: face on view of a simulated shock compressed layer by *Abe et al.* (2021), where most major filaments are created by type-O mechanism. Middle (bottom): Filament line mass function (FLMF) at $t = 0.3$ ($t = 1.3$) Myr in the shocked layer. The grey regions show the range below the filament detection threshold.

Remarkably, the line-mass distribution of filaments (or

FLMF) created by both type-O and type-C mechanisms (cf. Fig. 5) resembles the observed, Salpeter-like FLMF (*André et al.* 2019, see Fig. 11a and discussion in Sect. 3.6 below). The middle and bottom panels of Fig. 5 show the FLMF obtained at two time steps in a simulation of the dominant (type-O) filament formation mechanism (*Abe et al.* 2021). Throughout the evolution, smaller line-mass filaments always dominate in mass. Once the shock wave attenuates, many subcritical filaments stop evolving due to the finite type-O accretion duration and eventually disappear due to shear out or expansion. The type-O accretion duration depends on the scale of the pre-shock molecular clumps, which have a broad size distribution in turbulent molecular clouds. However, once a filament evolves into the supercritical regime, it is long-lived and can continue to accumulate mass due to gravitational accretion (cf. Sect. 3.1). Since the type-O formation mechanism is induced by a high-velocity shock, the resulting filaments can become as massive as $\gtrsim$ 100 $M_\odot$ pc^{-1} on a timescale of a fraction of a Myr, which is reminiscent of recent works connecting high-velocity gas flows and massive star/cluster formation (*Fukui et al.* 2021).

2.3. Synergy of Observations and Theory

Numerical simulations of molecular cloud formation out of the magnetized atomic medium stress the necessity of multiple compressions for the formation of the cold molecular medium (e.g., *Inoue and Inutsuka* 2009, 2012; *Inutsuka et al.* 2015, and see above). Such multiple compressions from expanding HI shells (see Fig. 1) are suggested by observations showing sheet-like extended structures connected in velocity (as seen in PV diagrams) to cylindrical filaments (*Arzoumanian et al.* 2018, 2022; *Shimajiri et al.* 2019a). The sheet-like geometry of molecular clouds is also suggested by the column density structure of compressed shells observed around HII regions. These shells are better described by a 3D ring geometry rather than a spherical geometry (see Fig. 3 and *Zavagno et al.* 2020). The 3D cylindrical structure of *Herschel* (star-forming) filaments is supported by the successful detection of dense molecular gas tracers (such as N_2H^+, $H^{13}CO^+$, HC_3N, and NH_3, cf., *Li and Goldsmith* 2012). This favours a truly high density in these filaments, rather than high column density sheet-like structures seen edge-on. In addition, *Bonne et al.* (2020) used radiative transfer modelling of two transitions of the ^{13}CO emission (3–2) and (2–1) observed with APEX and showed that the Musca filament (*Cox et al.* 2016) is a cold ($\sim$10 K), dense ($n_{\rm H_2} \sim 10^4$ cm^{-3}) velocity-coherent (*Hacar et al.* 2016) 10 pc long structure, which is best described with a $\sim$0.1 pc-width cylindrical geometry.

The theoretical classification of filament formation mechanisms helps in understanding some observations. In the early filament formation stage of the type-O mechanism, a characteristic V-shaped structure can be seen in the position-velocity (PV) map across the filament, and a curved magnetic field around the filament can be observed. Such signatures have been reported recently in observations of velocity structure (*Arzoumanian et al.* 2018; *Kandori et al.* 2020; *Bonne et al.* 2020) and magnetic field structure (*Tahani et al.* 2018, 2019). The different curvature of the velocity pattern in the PV maps (V-shaped or Λ-shaped) toward filaments in the same region may suggest different episodes of compressions (*Arzoumanian et al.* 2022). In this scenario of filament formation, one would expect to observe a population of subcritical, low-column-density filaments oriented perpendicular to the B-field. This seems in contradiction with previous results derived from polarization data (e.g., *Planck Collaboration Int. XXXII* 2016; *Planck Collaboration Int. XXXV* 2016; *Palmeirim et al.* 2013; *Cox et al.* 2016; *Soler et al.* 2016) that subcritical filaments almost always align parallel to the surrounding magnetic field lines on the plane-of-the-sky. This discrepancy may be due to the rapid transition of a newly formed, young filament from the thermally subcritical to the thermally transcritical/supercritical regime resulting from the fast accretion of surrounding matter onto the evolving filament ($\sim$10 $M_\odot$ pc^{-1} in $\sim$0.2 Myr, cf., *Arzoumanian et al.* 2018). For statistical reasons, such short timescales may be difficult to observe.

In the type-C/G models, velocity gradients across the filaments are generated as a consequence of anisotropic gas accumulation from a flattened layer. This preferred-direction of gas accretion is a distinguishing kinematic feature of such a filament formation scenario, which has been reported in observations of both nearby star-forming clouds and distant IRDCs (see Fig. 6 and Sect. 3.1 below). Overall, the available observations seem to be consistent with a scenario in which dense molecular filaments form initially through the type-O or type-C mechanisms and subsequently grow in mass due to gravity-induced accretion. *Chen et al.* (2020a) proposed that, by comparing the ratio between the kinetic energy of the flow transverse to the filament and the gravitational potential energy of the filament gas, one could distinguish between filaments formed purely due to direct turbulent compression and those formed due to gravity-induced accretion (type-O/C/G). Following this theoretical argument, *Dhabal et al.* (2019) proposed that the large velocity gradient observed across the south-east filament of NGC 1333 is due to the collision between a large-scale turbulent cell and the cloud, and that this filament is likely at the front-end of an expanding bubble.

The proposed type-C/O filament formation models are also compatible with statistical results on the relative orientation between filament axis and magnetic field lines, as derived from observations of dust polarized emission with *Planck* and starlight polarization (*Planck Collaboration Int. XXXII* 2016; *Planck Collaboration Int. XXXIII* 2016; *Planck Collaboration Int. XXXV* 2016; *Palmeirim et al.* 2013; *Cox et al.* 2016; *Soler et al.* 2016; *Wang et al.* 2020b). These studies show that the plane-of-the-sky (POS) B-field orientations are mostly perpendicular to high column density supercritical filaments. Recently, higher sensitivity and angular resolution observations with

SOFIA/HAWC+ and JCMT/POL2 revealed the complex but organized small-scale structures of the B-field within filaments, where the B-field has locally ordered configurations varying in connection with the underlying column density structures (e.g., *Doi et al.* 2020; *Li et al.* 2022). Toward hub-filament systems, the B-fields are observed mostly perpendicular to the filaments in their outer parts, away from the hubs. In the inner parts, where filaments merge with the hubs, the POS B-field becomes mostly parallel to the filaments (*Wang et al.* 2020a; *Pillai et al.* 2020; *Arzoumanian et al.* 2021). This changes of the relative B-field orientation from perpendicular to parallel in the interior of dense filaments connected to hubs suggests a coupled evolution of the B-field and the filaments. Such a reorganization of the B-field along the filaments, due to local velocity flows of matter in-falling onto the hubs, is also suggested by MHD simulations (e.g., *Gómez et al.* 2018).

As mentioned above, the HI medium is itself filamentary, as seen in observations (*Clark et al.* 2014; *Clark and Hensley* 2019) and simulations (*Inoue and Inutsuka* 2016). The conditions under which HI filaments, formed by thermal instability, may evolve into molecular star-forming filaments are still poorly known. However, since these HI filaments are thermally stable and long-lived, they might be gathered and merged by type-O/C/G flows induced by other HI shocks, and potentially evolve into molecular filaments as observations suggest (see Sect. 2.1.2). Similarly, the shock wave associated with an HII region expanding in an already filamentary atomic and molecular medium may induce the formation of new filaments, as well as reshape, compress, and gather pre-existing filaments playing an important role in the evolution, star formation history, and properties of the cores formed from filament fragmentation (see Sect. 3 below). Future observational and theoretical studies (*Haid et al.* 2019) are needed to refine our understanding of the possible evolutionary link between atomic and molecular filaments and the role of HI and HII regions (i.e., formation and/or feedback) on the surrounding atomic and molecular filamentary ISM.

3. EVOLUTION AND FRAGMENTATION OF DENSE MOLECULAR FILAMENTS

3.1. Inflow from Cloud to Dense Filaments

3.1.1. *Evidence of Non-isotropic Inflow of Ambient Gas in Sheet-like or Bubble-like Parent Cloud Structures*

In agreement with the scenario of filament formation favored in the previous section, molecular line studies of the projected velocity field observed within nearby filament systems support the view that dense star-forming filaments continuously grow through accretion or inflow from flattened cloud layers. Velocity gradients both along and perpendicular to the major axis of molecular filaments have been detected (e.g., *Peretto et al.* 2006; *Kirk et al.* 2013a; *Friesen et al.* 2013; *Shimajiri et al.* 2019a; *Chen et al.* 2020c), but the gradients across filaments often dominate in amplitude (e.g., *Fernández-López et al.* 2014; *Dhabal et al.* 2018). Such transverse velocity gradients, sometimes seen consistently along the entire length of the filamentary structure (*Beuther et al.* 2015a), would not be observed if the filaments were embedded in (and isotropically accreting from) a spherical or cylindrical ambient cloud (see Fig. 6b). Transverse velocity gradients which switch directions several times over the length of a filament are nevertheless consistent with *anisotropic* cylindrical inflow (*Clarke et al.* 2018).

These transverse gradients may a priori arise from large-scale inflow, rotation, shearing motions, or a combination of these types of motions. However, large-scale solid-body rotation of filaments around their main axis at the level implied by the observed gradients is unlikely, as it would severely distort the filaments and their radial density structure (*Recchi et al.* 2014; *Zhang et al.* 2020a). Shearing motions can produce filamentary structures with transverse velocity gradients, but the resulting filaments are expected to be non-self-gravitating or subcritical (*Hennebelle* 2013). Therefore, transverse velocity gradients across self-gravitating filaments are most readily explained if these filaments are forming and growing inside sheet-like or shell-like structures (see Fig. 6b).

Numerical MHD simulations of filament formation within shock-compressed layers generated by large-scale supersonic flows (e.g., *Inoue et al.* 2018; *Chen et al.* 2020a) can reproduce this kinematic pattern (cf. model types C/O in Sect. 2). The observed transverse gradients appear to be roughly aligned with the large-scale magnetic field (e.g., *Palmeirim et al.* 2013; *Bonne et al.* 2020) and in some cases, such as Orion A, there are hints that the magnetic field has a bow-shaped morphology (e.g., *Tahani et al.* 2019). This is consistent with a picture of magnetically-aligned inflow of matter from a shell-like parent cloud.

3.1.2. *Models and Simulations of Accreting Filaments*

Accretion from inflowing gas in the surrounding medium is highly important to filaments as it provides an external pressure via ram pressure, as well as delivering mass and energy into the filament. The presence of an external pressure acts to confine filaments to finite radii and to produce shallower density profiles, $\rho(r)$, which are consistent with the observed logarithmic slopes $p \equiv -d\ln\rho/d\ln r \sim 2$ (*Fischera and Martin* 2012); without such a pressure filaments extend to infinite radii and possess a steep $p = 4$ density profile (*Ostriker* 1964).

Additionally, the effect that accretion has on filaments, due to their delivery of additional mass as well as kinetic energy, is profound in controlling filament evolution (*Heitsch* 2013a,b; *Clarke et al.* 2016; *Smith et al.* 2016; *Clarke et al.* 2017; *Heigl et al.* 2018; *Clarke et al.* 2020; *Heigl et al.* 2020). The key effect is that of accretion driven turbulence, where a fraction of the kinetic energy of the accreted material is converted into turbulent energy. Thus an accreting filament gains mass while simultaneously gaining in turbulent

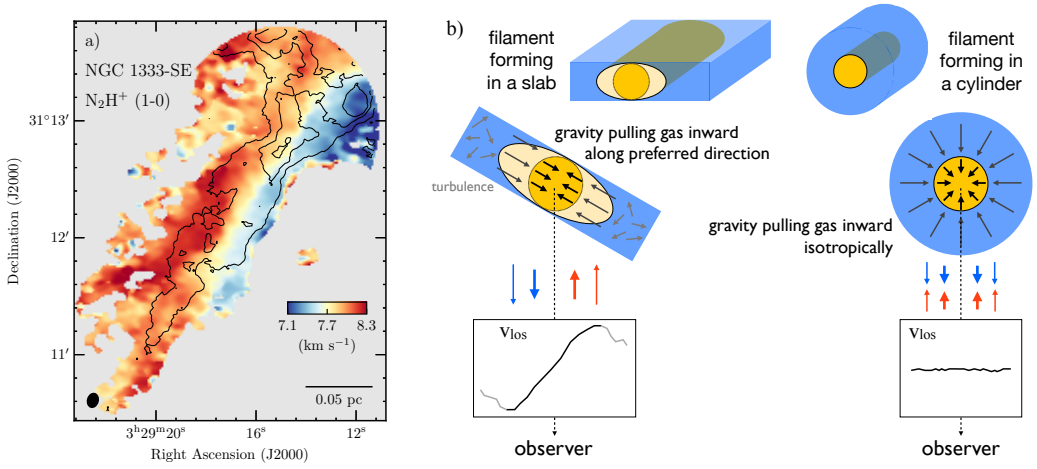

Fig. 6.— (a) Example of a consistent transverse velocity gradient observed in N_2H^+ (1–0) across a filament in the NGC 1333-SE region at $d \approx 300$ pc (adapted from *Dhabal et al.* 2018), which can be interpreted as accretion in a sheet-like cloud as illustrated in (b) (adapted from *Chen et al.* 2020a).

support, which may explain the observations that dense filaments are close to virial equilibrium (cf. *Arzoumanian et al.* 2013) and have a common half-power width $\sim$0.1 pc (cf. Fig. 7 and § 3.3 below). Moreover, this continuous input of energy and mass leads to the conclusion that hydrostatic equilibrium may never be achieved in filaments, unless the accretion timescale is considerably longer than the filament crossing time. Accretion also has a considerable impact on filament fragmentation into cores as discussed later.

3.2. Filamentary Substructures

3.2.1. Observational Evidence

A frequent feature of many dense molecular filaments is the presence of significant substructures observed in the form of velocity-coherent features, called *fibers*. The presence of fibers was first reported by *Hacar et al.* (2013) in the Taurus B211/B213 filament ($d \sim$140 pc), for which a friends-of-friends algorithm in velocity (FIVE) was used to identify at least 20 velocity-coherent components in N_2H^+ and $C^{18}O$. Subsequently, similar velocity-coherent components were detected in N_2H^+ in other regions, including the IRDC G035.39-00.33 (*Henshaw et al.* 2014), the NGC 1333 protocluster (*Hacar et al.* 2017a), IRDC G034.43+00.24 (*Barnes et al.* 2018a), the Orion A integral-shaped filament (*Hacar et al.* 2018), and the NGC 6334 main filament (*Shimajiri et al.* 2019b, see Fig. 8b below). The velocity-coherent substructures identified in NGC 1333 and Orion A are well separated in the plane of sky, however, and may differ in nature from those observed in Taurus and NGC 6334 which are intertwined. Moreover, not all molecular filaments consist of multiple fiber-like substructures. The Musca filament, for instance, is a 6-pc-long velocity-coherent filament with much less velocity substructure than the Taurus B211/3 filament, and may be interpreted as a single-fiber system (*Hacar et al.* 2016; *Cox et al.* 2016).

Interestingly, most of the line-identified fibers can also be detected in *Herschel* dust continuum maps when large-scale emission is filtered out, enhancing the contrast of small-scale structures in the data (cf. *Men'shchikov* 2013; *André et al.* 2014). Moreover, the *Herschel* data suggest that these fibers are somehow linked to fainter, magnetically-aligned striations often observed around the main filaments, almost perpendicular to their long axis. In the Taurus B211/B213 and Musca filaments, for instance, hair-like strands or spur-like features, which appear to be the tips of larger-scale striations, are visible in the immediate vicinity of the filaments, attached to their main body (*Palmeirim et al.* 2013; *Cox et al.* 2016; *Bonne et al.* 2020). This is suggestive of a direct physical connection between striations and fibers, and is consistent with the observed striations tracing accretion flows onto the main filaments, possibly influencing the formation of their fiber-like substructure.

3.2.2. Physical Origin

Numerical simulations have shown that the presence of fiber-like substructures is most likely linked to accretion flows onto the main filament. Both *Smith et al.* (2016) and *Clarke et al.* (2017) show that accretion from an inhomogeneous and turbulent medium leads to the formation of small substructures within larger parent filaments, albeit via two distinct mechanisms. *Smith et al.* (2016) show that the turbulence within a larger cloud leads to numerous small filaments forming independently of each other which are subsequently swept together into a single filament or accreted onto already formed filaments. This mechanism is termed **fragment and gather**. Meanwhile, *Clarke et al.* (2017) show that the turbulence driven by accretion of clumpy material leads to numerous coherent shocks and a strong vorticity field in a filament. This driven turbulence leads to the formation in situ of substructures similar to the **fray and fragment** mechanism proposed by *Tafalla and Hacar* (2015). It is currently unclear which formation mechanism

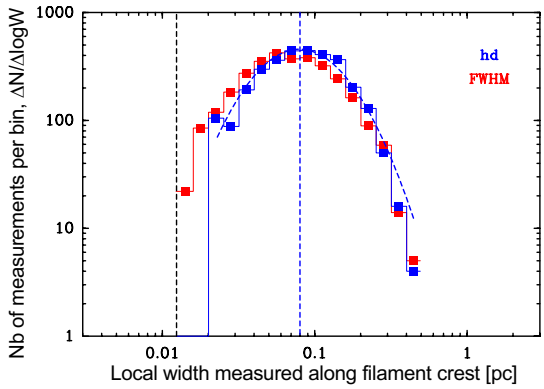

Fig. 7.— Distribution of local FWHM widths derived from more than 3000 independent radial profile measurements along the crests of 205 *Herschel* filaments in three nearby molecular clouds (Taurus, Ophiuchus, Pipe) at $d \sim 140$ pc (adapted from *Arzoumanian et al.* 2019). The blue and red histograms correspond to two methods of estimating the FWHM width. The dashed blue curve is a lognormal fit to the blue histogram, which peaks at the median width ∼0.08 pc (vertical blue dashed line). The black dashed line marks the *Herschel* resolution ∼0.012 pc in these regions.

for filamentary substructures is dominant and in which scenarios.

The substructures formed in simulations are reminiscent of the velocity-coherent fiber structures seen in observations (e.g., *Hacar et al.* 2013); although it must be noted that synthetic observations (*Clarke et al.* 2018) and purely numerical works (*Moeckel and Burkert* 2015; *Zamora-Avilés et al.* 2017) show that projected structural and velocity coherence are insufficient conditions for a real filament and high levels of caution must be applied when dealing with fibers.

3.3. The Common Width of Molecular Filaments

3.3.1. Observational Evidence

The filamentary structures detected with *Herschel* span broad ranges in length, central column density, and mass per unit length (e.g., *Schisano et al.* 2014; *Arzoumanian et al.* 2019). In contrast, detailed analysis of the radial column density profiles indicates that, at least in nearby (d <450 pc) molecular clouds, *Herschel* filaments are characterized by a narrow distribution of half-power widths with a typical value of ∼0.1 pc and a dispersion of less than a factor of 2 when the data are averaged over the filament crests (*Arzoumanian et al.* 2011, 2019). In particular, it is remarkable that molecular filaments appear to share approximately the same inner width in the *Herschel* data regardless of their mass per unit length $M_{\rm line}$, whether they are thermally *subcritical* with $M_{\rm line} \lesssim 0.5\,M_{\rm line,crit}$, *transcritical* with $0.5\,M_{\rm line,crit} \lesssim M_{\rm line} \lesssim 2\,M_{\rm line,crit}$, or *thermally supercritical* with $M_{\rm line} \gtrsim 2\,M_{\rm line,crit}$, where $M_{\rm line,crit} = 2\,c_s^2/G$ is the thermal value of the critical mass per unit length (e.g., *Ostriker* 1964), i.e., $\sim 16\,M_\odot$ pc^{-1} for a sound speed $c_{\rm s}$ ∼0.2 km s^{-1} or a gas temperature $T \approx$10 K.

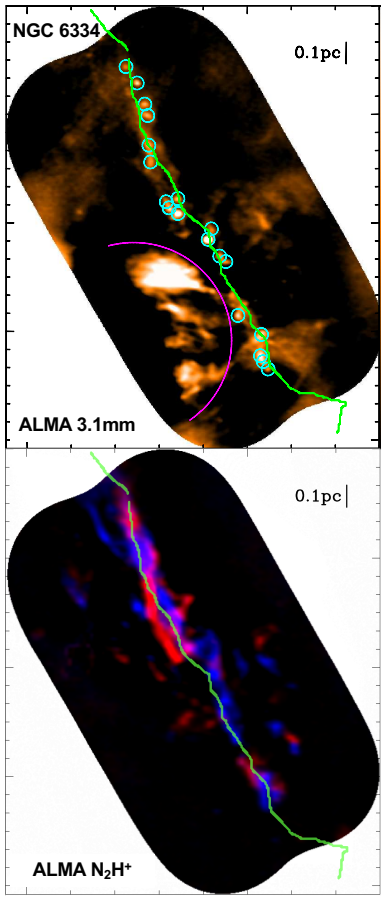

Fig. 8.— Dense cores (*top*) and intertwined fiber-like substructures (*bottom*) as viewed by ALMA in the massive NGC 6334 filament with $M_{\rm line} \sim 500\,M_\odot$ pc^{-1} (*Shimajiri et al.* 2019b). The top panel is a 3.1 mm dust continuum map. The bottom panel shows an overlay of two N_2H^+ (1–0) maps, integrated over two distinct velocity ranges separated by 1.1 km s^{-1}. Green curve shows the crest of the filament as traced by the DisPerSE algorithm in the APEX/ArTéMiS 350 μm dust continuum map of the region (*André et al.* 2016). The purple curve in the top panel marks the boundary of a compact HII region, whose expansion may be compressing the filament from the side.

Independent submillimeter continuum studies of filament widths in nearby clouds have generally confirmed this result (e.g., *Alves de Oliveira et al.* 2014; *Koch and Rosolowsky* 2015; *Salji et al.* 2015; *Rivera-Ingraham et al.* 2016). Measurements of filament widths obtained in molecular line tracers (e.g., *Pineda et al.* 2011; *Fernández-López et al.* 2014; *Panopoulou et al.* 2014; *Hacar et al.* 2018; *Monsch et al.* 2018; *Schmiedeke et al.* 2021) have been less consistent with the *Herschel* dust continuum results, however. For instance, using ^{13}CO emission, *Panopoulou et al.* (2014) found a broad distribution of widths in Taurus, with a peak of 0.4 pc. *Hacar et al.* (2018) found a median width of 0.035 pc for Orion "fibers" in the integral-shaped filament of Orion, combining N_2H^+ ALMA and IRAM 30-m observations. Likewise, *Schmiedeke et al.* (2021) found a typical width of 0.03 pc along two filaments in Perseus-B5

using combined VLA and GBT NH_3 observations. These differences can be attributed to the lower dynamic range of densities sampled by observations in any given molecular line tracer compared to dust observations (*Priestley and Whitworth* 2020, Shimajiri *et al.*, in prep.). More specifically, ^{12}CO or ^{13}CO data only trace low-density gas and cannot reliably measure the whole (column) density profile (hence the width) of a dense molecular filament. Likewise, commonly observed transitions of N_2H^+ or NH_3 only trace relatively high density gas (typically above the effective densities $n_{\rm eff}$ of the transitions – cf. *Shirley* 2015) and cannot reliably measure the whole profile of a filament either. In contrast, submillimeter dust continuum images obtained from space (with *Herschel*) achieve a significantly higher dynamic range and are sensitive to both the low density outer parts and the dense inner parts of filaments. While some changes in dust properties (emissivity and temperature) may occur in the interior of the densest filaments and affect the width measurements obtained in the dust continuum (cf. *Schmiedeke et al.* 2021), these effects appear to be rather modest (cf. *Schuller et al.* 2021). For moderately dense filaments, the most reliable molecular gas tracer seems to be the C^{18}O (1–0) line which results in widths approximately around 0.1 pc, in agreement with the dust continuum findings in both simulations and observations, albeit with a somewhat broader spread of values (*Clarke et al.* 2018; *Suri et al.* 2019; *Orkisz et al.* 2019).

Some concerns have been raised about the reliability of the filament widths found with *Herschel* (*Smith et al.* 2014; *Panopoulou et al.* 2017, 2022). In particular, *Panopoulou et al.* (2017) pointed out an apparent contradiction between the existence of a characteristic filament width and the essentially scale-free nature of the power spectrum of interstellar cloud images (well described by a single power law from ∼0.01 pc to ∼50 pc; *Miville-Deschênes et al.* 2010, 2016). However, *Roy et al.* (2019) showed that there is no contradiction given the only modest area filling factors ($\lesssim$ 10%) and column density contrasts (≤100% in most cases) derived by *Arzoumanian et al.* (2019) for the filaments seen in *Herschel* images. For realistic filament filling factors and column density contrasts, filamentary structures contribute only a negligible fraction of the image power spectra.

Another caveat pointed out by *Panopoulou et al.* (2017, 2022) is the potential presence of systematic biases in filament width measurements, especially those based on Gaussian fits. Indeed, the radial density profiles of molecular filaments often feature pronounced power-law wings with logarithmic slopes in the range $1.5 \leq p \leq 2.5$ and tend to be better represented by Plummer-like profiles than by Gaussian distributions (e.g., *Palmeirim et al.* 2013). As it is well known that the FWHM size of a power-law (scale-free) distribution convolved with a Gaussian beam is always slightly larger than the beam size (e.g., *Ladd et al.* 1991), the role of observational resolution must be considered with care. For cylindrical power-law density distributions with indices $1.5 \leq p \leq 2.5$, the apparent FWHM width is expected to be ∼5–90% larger than the beam size. The Hi-GAL filaments analyzed by (*Schisano et al.* 2014) have observed FWHM widths only ∼90% broader than the *Herschel* 500 μm beam size, consistent with power-law wings with $p \sim 1.5$ and either unresolved or non-existent flat inner density profiles. However, the *Herschel* 500 μm beam size (36.3″) corresponds to ∼0.2–0.5 pc at d ∼1–3 kpc and is not sufficient to resolve an inner width of ∼0.1 pc at the typical distances of Hi-GAL filaments. In contrast, the observed half-power widths of the nearby (d <450 pc) filaments studied by *Arzoumanian et al.* (2019) are a factor ∼2.5–8 broader than the *Herschel* 250 μm beam size (18.2″), inconsistent with scale-free density profiles. Moreover, performing numerous tests using synthetic data, *Arzoumanian et al.* (2019) showed that their method of measuring filament profiles and widths was reliable and free of significant biases, at least when the contrast of the filaments over the local background exceeds ∼50%, which is the case for ∼70% of the *Herschel* filament population they measured and >80% of star-forming filaments. These tests suggest that the typical half-power width ∼0.1 pc obtained through the analysis of the radial profiles of nearby *Herschel* filaments is robust. Nevertheless, there are sometimes large local deviations, by a factor of $\gtrsim$ 2–4, from the typical width (e.g., *Juvela et al.* 2012; *Ysard et al.* 2013).

The distribution of local widths found by *Arzoumanian et al.* (2019) for 205 molecular filaments in Taurus, Ophiuchus, Pipe (at d ∼140 pc) prior to averaging along the filament crests is well described by a lognormal function centered at 0.08 ± 0.01 pc with a standard deviation of 0.3 ± 0.02 dex, corresponding to a factor of ∼2 on either side of the median width (see Fig. 7). A very similar distribution of individual half-power widths was recently reported by *Schuller et al.* (2021) for the Orion integral-shaped filament. *Schuller et al.* (2021) further show that both the choice of the filament-tracing algorithm and the effect of uncertainties in dust properties have only a small influence on the derived column density profiles, hence the estimated filament widths. The median half-power diameter ∼0.1 pc measured with *Herschel* therefore appears to reflect the presence of a true common scale in the filamentary structure of molecular clouds. Further high-resolution submillimeter continuum studies are nevertheless required to confirm that the same common width also holds in clouds beyond a distance of ∼500 pc (see *André et al.* 2016; *Schuller et al.* 2021). Although no clear trend has been found concerning a possible time evolution of the filament width in a statistically significant sample of filamentary structures, tentative evidence of a weak correlation between local width and central density has been reported for a set of transverse cuts observed toward two Perseus filaments (*Schmiedeke et al.* 2021). This type of study also needs to be followed-up.

3.3.2. *Theoretical Interpretation*

Without extra support, isolated thermally supercritical filaments should undergo fast radial contraction on a free-

fall timescale (*Inutsuka and Miyama* 1992). However, there exists a population of 'wide', supercritical filaments where $M_{\rm line} \gg M_{\rm line,crit}$, such as the filament shown in Fig. 8 which has $M_{\rm line} \sim 500\,M_\odot\,{\rm pc}^{-1}$ and a half-power width $\sim$0.15 pc, suggesting that they cannot be so transient. There currently exists two categories of explanation for this: accretion driven turbulence and magnetic fields.

Heitsch (2013a) and *Hennebelle and André* (2013) propose that accretion driven turbulence may delay the moment of observational collapse and explain the observational decorrelation between filament width and peak column density (*Arzoumanian et al.* 2019). However, it cannot prevent radial gravitational collapse. This is supported by the simulations performed by *Heigl et al.* (2020) which show that unmagnetized accretion driven turbulence cannot contribute to the stability of the filament by increasing the critical line-mass as the turbulent pressure does not possess a radial profile, i.e. it cannot provide a supporting force, but does act to widen a filament. *Clarke et al.* (2017) show that this behavior changes when the accretion flow is highly inhomogeneous; the anisotropic, clumpy nature of the accreted material produces both sub-filament sub-structure and local regions of rotation. They show that this allows a thermally supercritical filament ($1.3\times M_{\rm line,crit}$) to remain wide and have a diameter of 0.12 pc. *Clarke et al.* (2020) show increasingly unstable filaments ($\sim 3\times M_{\rm line,crit}$) with comparably wide diameters. However, these simulations did not include filaments with $M_{\rm line} \gg M_{\rm line,crit}$, and so it is currently unclear to what line-mass a filament thus supported could be maintained.

Support from magnetic fields has been a natural answer to the question of supercritical filament widths (*Nagasawa* 1987; *Fiege and Pudritz* 2000a; *Tomisaka* 2014; *Seifried and Walch* 2015; *Inoue et al.* 2018). Observations indicate that some filaments are magnetically transcritical (*Li et al.* 2022, Pattle *et al.*, in this volume), suggesting the magnetic field may indeed play a significant role. Due to the anisotropy of a filament the magnetic field direction is the dominant decider of its role in support. Magnetic field configurations which have the field parallel to the filament's axial axis are highly effective at providing support against gravity as radial collapse requires gas movement perpendicular to the field lines. As noted above, this is rarely observed for the *ambient* magnetic field in the immediate vicinity of dense filaments. There is a hint, however, from recent high-resolution polarization observations with ALMA and SOFIA (*Dall'Olio et al.* 2019; *Pillai et al.* 2020) that there may be a transition from perpendicular field to parallel field orientation in the *interior* of some supercritical filaments. More systematic high-resolution polarization studies will be key to assessing whether this is a generic trend.

Perpendicular magnetic field configurations have been shown semi-analytically to provide support and may increase the critical line-mass to an arbitrarily large value depending on the field strength (*Tomisaka* 2014; *Kashiwagi and Tomisaka* 2021). This has not been seen in some simulations designed to investigate the impact of the magnetic field direction (*Seifried and Walch* 2015), but simulations considering the oblique-shock formation mechanism for filaments (*Inoue et al.* 2018) appear to be consistent with the result of *Tomisaka* (2014). The apparent disagreement may be due to the relatively weak field strength considered in the *Seifried and Walch* (2015) simulations. Further numerical work focused on this question would be highly beneficial. It should also be noted that the high magnetic field strength necessary to provide radial support to a filament when the field is perpendicular, may also curb filament fragmentation and core formation (*Hanawa et al.* 2017), which is in tension with the numerous highly fragmented super-critical filaments seen in observations (for example Fig. 8). When considering more complicated helical fields, one finds that the ratio of toroidal and poloidal components may increase or decrease the critical line-mass (see *Fiege and Pudritz* 2000a, for more details) It is thus of considerable interest to observationally determine the magnetic field geometry within the $\sim$0.1 pc filament width to better constrain theoretical works invoking supporting magnetic fields.

Both explanations, accretion driven turbulence and magnetic fields, show promise in answering the question of additional support; however, neither explanation is currently conclusive. Further work focused on this question is necessary, with particular attention paid to the limits of these support mechanisms as well as the combination and interaction of the two mechanisms.

3.4. The Filament-core Connection

Thanks to the high surface-brightness sensitivity and spatial dynamic range achievable from space, a big step forward with *Herschel* imaging surveys compared to earlier submillimeter ground-based observations has been the ability to *simultaneously* probe compact structures such as dense cores *and* larger-scale structures within the parent clouds such as filaments. This has provided, for the first time, an unbiased view of both the spatial distribution of dense cores and the link between dense cores and the texture of molecular clouds. In particular, *Herschel* GBS observations have shown that most ($75\%^{+15\%}_{-5\%}$) prestellar cores are located within filamentary structures of typical column densities $N_{\rm H_2} \gtrsim 7\times10^{21}\,{\rm cm}^{-2}$, corresponding to visual extinctions $A_{\rm V} \gtrsim 7$ mag (e.g., *André et al.* 2010; *Könyves et al.* 2015; *Marsh et al.* 2016). Moreover, most prestellar cores lie very close to the crest of their parent filament (e.g., *Bresnahan et al.* 2018; *Könyves et al.* 2020; *Ladjelate et al.* 2020), that is within the flat inner $<$0.1 pc portion of the filament radial profile (cf. *Arzoumanian et al.* 2011, 2019).

The column density transition above which prestellar cores are found in filaments is quite pronounced. Indeed, the observed core formation efficiency, defined as ${\rm CFE}_{\rm obs}(A_{\rm V}) = \Delta M_{\rm cores}(A_{\rm V})/\Delta M_{\rm cloud}(A_{\rm V})$ where $\Delta M_{\rm cores}(A_{\rm V})$ is the mass in the form of prestellar cores in a given bin of background $A_{\rm V}$ values and $\Delta M_{\rm cloud}(A_{\rm V})$ is the total cloud mass in the same bin, resembles a smooth step function when plotted against the "background" col-

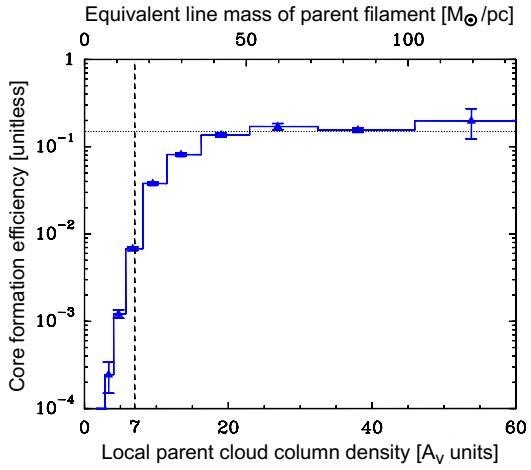

Fig. 9.— Prestellar core formation efficiency [$\mathrm{CFE}(A_\mathrm{V}) = \Delta M_\mathrm{cores}(A_\mathrm{V})/\Delta M_\mathrm{cloud}(A_\mathrm{V})$] in the Aquila molecular cloud (blue histogram with error bars) as a function of background column density expressed in A_V units using the simple conversion $N_{\mathrm{H}_2}(\mathrm{cm}^{-2}) = 0.94 \times 10^{21}\, A_\mathrm{V}$ (*Bohlin et al.* 1978). The latter is dominated by the column density of the parent filaments at high A_V. (From *Könyves et al.* 2015.)

umn density of the parent filaments (cf. Fig. 9 and *Könyves et al.* 2015). There is a natural interpretation of this column density transition for prestellar core formation in terms of simple theoretical expectations for the gravitational instability of nearly isothermal gas cylinders. Adopting the typical inner width $W_\mathrm{fil} \sim$0.1 pc measured for nearby molecular filaments with *Herschel* (*Arzoumanian et al.* 2011, 2019) and using the relation $M_\mathrm{line} \approx \Sigma_0 \times W_\mathrm{fil}$ between the central gas surface density Σ_0 and the mass per unit length M_line of a filament, there is a very good match between the transition at $A_\mathrm{V}^\mathrm{back} \sim$7 mag or $\Sigma_\mathrm{gas}^\mathrm{back} \sim 150\, M_\odot\,\mathrm{pc}^{-2}$ and the critical mass per unit length $M_\mathrm{line,crit} = 2\, c_\mathrm{s}^2/G \approx 16\, M_\odot\,\mathrm{pc}^{-1}$ of isothermal long cylinders in hydrostatic equilibrium for a sound speed $c_\mathrm{s} \sim 0.2\,\mathrm{km\,s}^{-1}$, i.e., a typical gas temperature $T \approx$10 K (*Ostriker* 1964). Therefore, the observed column density transition essentially corresponds to thermally transcritical filaments with line masses within a factor of $\sim$2 of $M_\mathrm{line,crit}$, which are prone to gravitational fragmentation along their length (*Inutsuka and Miyama* 1992, 1997; *Fischera and Martin* 2012).

It is important to stress that it is the *local* value of the mass per unit length which matters for the fragmentation of a particular filament segment, and that the above-mentioned transition does not correspond to a perfectly sharp threshold. While most prestellar cores appear to form in filaments that are locally transcritical or supercritical ($M_\mathrm{line} \geq M_\mathrm{line,crit}/2$), examples of prestellar cores in globally subcritical (but locally transcritical) filaments have been observed in regions such as Lupus, Cepheus, and Perseus (*Benedettini et al.* 2018; *Howard et al.* 2019; *Di Francesco et al.* 2020; *Pezzuto et al.* 2021). This is supported by simulations which show that a locally supercritical line-mass is a sufficient condition for fragmentation (*Chira et al.* 2018).

3.5. Core Separations Along Molecular Filaments

3.5.1. *Observations of Core Spacings*

The observed separations of dense cores along filaments are not consistent with the predictions of standard semi-analytic cylinder fragmentation models without turbulence or magnetic fields. Linear fragmentation models for infinitely long, isothermal equilibrium cylinders indeed predict a characteristic core spacing of $\sim 4\times$ the filament width (e.g., *Inutsuka and Miyama* 1992). In contrast, the spacing observed between *Herschel* prestellar cores is generally not periodic and the median value of the projected core separation is found to be close to the typical $\sim$0.1 pc half-power width of the parent filaments (e.g., *André et al.* 2014; *Könyves et al.* 2020). A few good examples of quasi-periodic chains of dense cores have also been found (see Fig. 10, *Tafalla and Hacar* 2015, and *Zhang et al.* 2020a), but again the corresponding characteristic spacing appears to be comparable to, rather than $\sim 4\times$ larger than, the diameter of the parent filament. Moreover, complementary high-resolution studies with interferometers (*Takahashi et al.* 2013; *Teixeira et al.* 2016; *Kainulainen et al.* 2013, 2017; *Shimajiri et al.* 2019b, see Fig. 8a) have provided some evidence of two distinct fragmentation modes within at least some thermally supercritical filaments: a) "cylindrical" fragmentation mode corresponding to clumps or groups of cores with a separation consistent with $\sim 4\times$ the filament width taking projection effects into account; and b) "spherical", Jeans-like fragmentation mode corresponding to a typical spacing $\lesssim$ 0.1 pc between cores (and within groups). This discrepancy between observations and simple theoretical predictions may be understood by realizing that real molecular filaments are not isolated cloud structures in perfect hydrostatic equilibrium. Dynamic fragmentation models therefore appear much more appropriate (see below).

3.5.2. *Interpretation of Observed Core Spacings*

Supplementing classical near-equilibrium models of filament fragmentation (*Stodólkiewicz* 1963; *Nagasawa* 1987; *Inutsuka and Miyama* 1992; *Fiege and Pudritz* 2000a; *Fischera and Martin* 2012; *Hanawa et al.* 2017, 2019), dynamic models using numerical simulations considering accretion, turbulence, and magnetic fields have recently been proposed to interpret the observed core spacings (*Seifried and Walch* 2015; *Clarke et al.* 2016, 2017; *Gritschneder et al.* 2017; *Clarke et al.* 2020).

When filaments are accreting from a turbulent medium, *Clarke et al.* (2017) showed that fragmentation appears in a two-tier manner where large-scale fragmentation (separation length-scales) occurs first, followed by small-scale fragmentation at the effective Jeans length, which is consistent with observations. For filaments in which gravitational energy dominates over turbulent energy, the large-scale fragmentation occurs at the cylindrical fragmentation length scale found by *Clarke et al.* (2016); when the two are roughly equivalent, the large scale fragmentation is de-

termined by the turbulence itself, i.e. those locations which happen to be predominately compressive, and is thus random. In both cases, two-tier fragmentation occurs as the large-scale gravity/turbulent fragmentation leads to local regions exceeding the critical line-mass, a necessary condition for fragmentation as shown by *Chira et al.* (2018), even while the filament may still be globally subcritical. Subsequently, as the filament continues to gain mass and the entire filament reaches the critical line-mass, smaller scale perturbations may collapse as greater sections of the filament becomes unstable and the local collapse time-scale decreases. Due to the complexity of this fragmentation it is difficult to statistically and robustly detect the presence of characteristic fragmentation length-scales with the low number of cores typically present in a filament (*Clarke et al.* 2019).

The formation of cores is also affected by the presence of sub-filaments (*Smith et al.* 2016; *Clarke et al.* 2020). Sub-filaments may act in two distinct manners: they may fragment independently of each other to form cores (termed *isolated* cores by *Clarke et al.* 2020) or they may form small hub systems which form a grouping of cores (termed *hub* cores by *Clarke et al.* 2020). These sub-filaments can then act as channels for mass into cores (*Smith et al.* 2016), such that hub cores are typically more massive than isolated cores (*Clarke et al.* 2020). Moreover, the intermediate fragmentation step of forming sub-filaments leaves no strong evidence of quasi-periodic fragmentation with most core spacings being located at approximately the effective

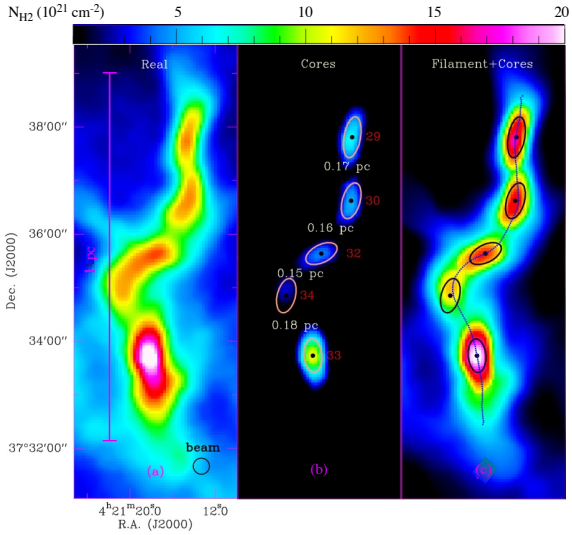

Fig. 10.— Quasi-periodic separations of dense cores along a transcritical filament in the California molecular cloud (from *Zhang et al.* 2020a). From left to right, the panels display the original column density map of the filament as derived from *Herschel* data at $18.2''$ resolution, and two filtered versions of this map emphasizing the dense cores identified along the filament with `getsources` (*Men'shchikov et al.* 2012), and the cores overlaid on the filament (after subtraction of the non-filamentary background), respectively.

Jeans length (*Clarke et al.* 2020).

Magnetic fields have typically been found to suppress filament fragmentation but the degree to which fragmentation is suppressed is dependent on the magnetic field orientation (*Nagasawa* 1987; *Fiege and Pudritz* 2000a; *Seifried and Walch* 2015; *Hanawa et al.* 2017, 2019). Axial magnetic field models suggest that there is still an expectation of quasi-periodic cores, but the spacing is larger than that expected from purely hydrodynamical models (*Nagasawa* 1987; *Seifried and Walch* 2015). Perpendicular fields may also lead to quasi-periodic cores with larger spacings but in cases where the magnetic field is fixed at large distances from the filament, even weak magnetic fields may completely suppress fragmentation (*Hanawa et al.* 2017). *Fiege and Pudritz* (2000b) showed that, for highly torodial fields, a fast magneto-instability may lead to fragmentation instead of gravity.

It is worth noting that other forms of fragmentation exist beyond gravo/magneto-instabilities. One such scenario is geometric fragmentation, where *spatial* rather than density perturbations may lead to fragmentation (*Gritschneder et al.* 2017). This process may occur on timescales comparable to other fragmentation processes and could lead to the formation of cores at any wavelength. Another process is that cores quickly form at the ends of filaments due to the end-dominated mode of global longitudinal collapse (*Bastien* 1983; *Pon et al.* 2012; *Clarke and Whitworth* 2015). Core formation due to global longitudinal collapse ought to produce massive cores/clumps preferentially toward the ends of filaments due to gravitational focusing. There is some observational evidence for such fragmentation (*Zernickel et al.* 2013; *Dewangan et al.* 2019; *Yuan et al.* 2020; *Bhadari et al.* 2020; *Liu et al.* 2020) and *Clarke et al.* (2020) found tentative signs of such core properties in their simulations of turbulent, accreting filaments.

3.6. From the Filament Line Mass Function to the Prestellar Core Mass Function

The mass function of molecular clouds (MCs) and CO clumps within MCs is known to be rather shallow, $\Delta N/\Delta \log M \propto M^{-0.6\pm0.2}$ (e.g., *Solomon et al.* 1987; *Blitz* 1993; *Kramer et al.* 1998; *Rice et al.* 2016), and significantly shallower than the Salpeter initial mass function (IMF, *Salpeter* 1955). This implies that most of the molecular gas mass in the Galaxy resides in the *most massive* MCs and within the MCs themselves in the most massive CO clumps. In contrast, the mass distribution of self-gravitating prestellar cores or prestellar *core mass function* (CMF) broadly resembles the stellar IMF in both shape and mass scale, (e.g., *Motte et al.* 1998; *Johnstone et al.* 2001; *Nutter and Ward-Thompson* 2007; *Alves et al.* 2007; *Könyves et al.* 2015; *Marsh et al.* 2016; *Di Francesco et al.* 2020; *Pezzuto et al.* 2021). The difference in shape between the observed mass distribution of MCs or CO clumps and that of prestellar cores may a priori arise from the use of different tracers, typically CO for clouds or clumps and dust continuum

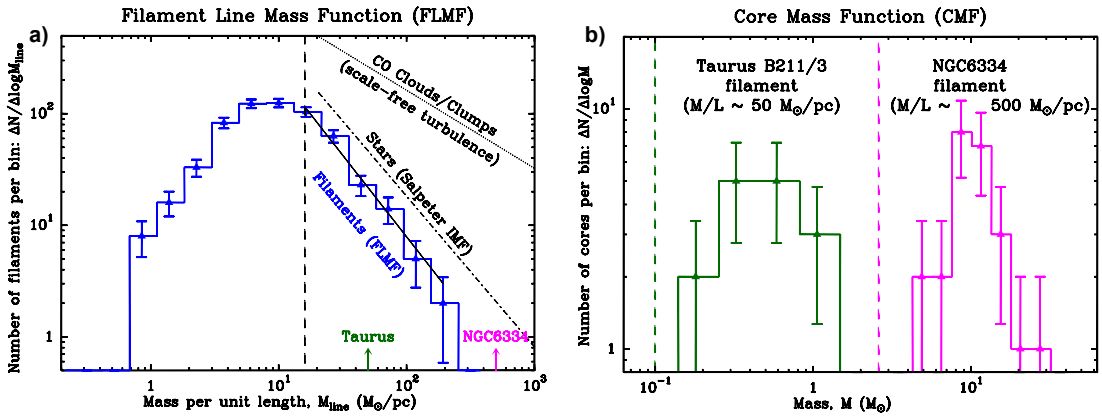

Fig. 11.— Potential role of filaments in the origin of the prestellar CMF and stellar IMF: As higher-mass cores form in higher-line mass filaments [panel (b), adapted from *Shimajiri et al.* 2019b and *Marsh et al.* 2016], the Salpeter slope of the global CMF and IMF may be inherited from the filament line mass function (FLMF) [panel (a), adapted from *André et al.* 2019].

for prestellar cores. However, millimeter/submillimeter dust continuum studies have also reported mass functions shallower than the Salpeter IMF for both small MCs/large clumps (e.g., *Ellsworth-Bowers et al.* 2015) and unbound starless cores (e.g., *Marsh et al.* 2016). The mass functions of the latter types of cloud structures therefore appear to genuinely differ from the IMF and prestellar CMF.

Recently, a good estimate of the filament mass function (FMF) and filament line mass function (FLMF) in nearby molecular clouds has been derived using a comprehensive study of filament properties from *Herschel* Gould Belt survey observations (*Arzoumanian et al.* 2019; *André et al.* 2019). The FLMF is well fit by a power-law distribution in the supercritical mass per unit length regime (above 16 $\mathrm{M_\odot\,pc^{-1}}$), $\Delta N/\Delta \log M_{\rm line} \propto M_{\rm line}^{-1.6\pm0.1}$ (see Fig. 11a). The FMF is very similar in shape to the FLMF and also follows a power-law distribution at the high-mass end (for $M_{\rm tot} > 15\,M_\odot$), $\Delta N/\Delta \log M_{\rm tot} \propto M_{\rm tot}^{-1.4\pm0.1}$, which is significantly steeper than the MC mass function. Both the FLMF and the FMF are reminiscent of the form of the IMF at the high-mass end ($M_\star \geq 1\,M_\odot$), which scales as the Salpeter power law $dN/d\log M_\star \propto M_\star^{-1.35}$ in the same format. Thus, molecular filaments may represent the key evolutionary step in the hierarchy of cloud structures at which a steep Salpeter-like mass distribution is established. The filament mass function differs in a fundamental way from the MC mass function in that most of the filament mass lies in *low-mass* filaments. In particular, this result implies that most of the mass of star-forming filaments lies in thermally transcritical filaments with line masses within a factor 2 of the critical value $M_{\rm line,crit}$. Interestingly, the numerical study of *Abe et al.* (2021) shows that the FLMF resulting from the type-O filament formation mechanism introduced in § 2.2.2 quickly becomes Salpeter-like and similar to the observed FLMF (see Fig. 5 above). The same FLMF shape is also seen in type-C induced filaments, but for the pure type-G mechanism *Abe et al.* (2021) report a significantly narrower FLMF which peaks at the (thermal) critical line-mass.

The most massive prestellar cores identified with *Herschel* (with masses between $M \sim 2$ and $10\,\mathrm{M_\odot}$) tend to be spatially segregated in the highest column density parts/filaments of the clouds, suggesting that the prestellar CMF is not homogeneous *within* a given cloud but depends on the local column density (or line mass) of the parent filaments (*Könyves et al.* 2020; see also *Shimajiri et al.* 2019b). In Orion B, for instance, there is a marked trend for the prestellar CMF to broaden and shift to higher masses in higher density areas (*Könyves et al.* 2020). This supports the view that the global prestellar CMF results from the superposition of the CMFs produced by individual filaments (*Lee et al.* 2017; *André et al.* 2019).

The close link between the FMF (or FLMF) and the prestellar CMF may be understood if we recall that the thermally supercritical filaments observed with *Herschel* in nearby clouds have a typical inner width $W_{\rm fil} \sim 0.1$ pc and are virialized with $M_{\rm line} \sim \Sigma_{\rm fil} \times W_{\rm fil} \sim M_{\rm line,vir} \equiv 2\,\sigma_{\rm tot}^2/G$, where $\sigma_{\rm tot}$ is equivalent to the effective sound speed (*Fiege and Pudritz* 2000c; *Arzoumanian et al.* 2013). This implies that the effective Bonnor-Ebert mass $M_{\rm BE,eff} \sim 1.3\,\sigma_{\rm tot}^4/(G^2\Sigma_{\rm fil})$ scales roughly as $\Sigma_{\rm fil}$ or $M_{\rm line}$ in supercritical filaments. Thus, higher-mass cores may form in higher $M_{\rm line}$ filaments, as indeed suggested by observations (*Shimajiri et al.* 2019b, see Fig. 11b). If the CMF produced by a single supercritical filament were a narrow δ function peaked at $M_{\rm BE,eff}$, then there would be a direct correspondence between the FLMF and the prestellar CMF (cf. *André et al.* 2014). In reality, the prestellar CMF generated by a single filament is expected to be broader than a δ function (*Inutsuka* 2001), and observationally it appears to broaden as $M_{\rm line}$ increases (*Könyves et al.* 2020), although for statistical reasons, this is difficult to constrain very accurately. The global prestellar CMF therefore results from a "convolution" of the FMF with the CMFs produced by individual filaments (*Lee et al.* 2017). It can be shown, however, that the high-mass end of the global CMF is primarily

driven by the power-law shape of the FLMF in the supercritical regime and depends only weakly on the breadths of the individual CMFs (cf. Appendix B of *André et al.* 2019).

4. DENSE CORES IN MOLECULAR CLOUDS

Dense, gravitationally bound molecular cores are the immediate precursors of stars. Generally speaking, "dense cores" can be used to refer to all overdense (relative to the background) structures at sub-pc scale, while "clumps" usually represent pc-scale complex structures that may further fragment into multiple cores. Following previous authors (*di Francesco et al.* 2007; *André et al.* 2014), we define *starless* cores as those that show no evidence of the presence of an embedded protostar, via the observational detection of a compact infrared or millimeter emission source, or outflows in molecular line emission, in contrast to *protostellar* cores. Cores that appear unstable to gravitational collapse are categorized as *prestellar* (see *André et al.* 2000; *Ward-Thompson et al.* 2007). This section reviews, from both observational and theoretical studies, the most recent updates on the properties of dense cores, which set up the initial conditions of subsequent protostellar evolution.

4.1. Large Area Surveys in Star-forming Regions

Cores are generally embedded within molecular clouds. Large-area, high-resolution surveys of dust and gas are thus essential in improving our understanding of the internal state of star-forming regions down to the core scale. While the advanced continuum studies have provided an unprecedented view of the physical properties in star-forming regions from cloud to core, the dynamic information probed by spectroscopic observations is critical to complete the picture. Here we review the most updated results from survey-style studies performed in recent years.

4.1.1. Dust Continuum Surveys

Over the past decade, large surveys of the continuum emission from dust have provided numerous insights into the structure of star-forming clouds across a wide range of spatial scales. With $\sim 15''$ angular resolution at 200 μm of the *Herschel* Space Observatory, the *Herschel* Gould Belt Survey (HGBS; see review in *André et al.* 2014) mapped, at 70–500 μm, large areas of star-forming molecular clouds within $\sim$ 500 pc of the Sun. As already described in Sect. 3.4, these observations revealed that dense cores are found primarily within ubiquitous filamentary structures in molecular clouds, with most prestellar cores in particular located within transcritical or supercritical filaments (*Könyves et al.* 2015, 2020; *Benedettini et al.* 2018; *Bresnahan et al.* 2018; *Ladjelate et al.* 2020; *Pezzuto et al.* 2021).

The JCMT SCUBA-2 Gould Belt Legacy Survey (GBS) (*Ward-Thompson et al.* 2007) mapped the densest regions of the Gould Belt clouds visible from the northern hemisphere, at 450 and 850 μm with higher (8–14$''$) resolution. While JCMT SCUBA-2 is less sensitive than *Herschel* to extended, lower column density material, JCMT GBS detects primarily the densest starless cores, more likely to be prestellar (*Ward-Thompson et al.* 2016). Core mass estimates tend to assume a specific power-law dependence of the dust emission with wavelength, often setting the dust emissivity, $\beta = 2$ or similar. Using the full range of continuum emission afforded by both *Herschel* and JCMT observations, (*Sadavoy et al.* 2013) showed evidence for a lower value of β indicative of grain growth in cores. Regions of low β may be correlated with local temperature peaks in NGC 1333 (*Chen et al.* 2016). Better understanding of where and when dust properties evolve will enable more precise measurements of core masses, as well as improving our understanding of the process of grain evolution from cloud to core.

Toward more distant regions, the *Herschel* infrared Galactic Plane Survey has provided comprehensive source catalogs toward the Galactic Plane (Hi-GAL; *Molinari et al.* 2016; *Elia et al.* 2021), although without sufficient spatial resolution to resolve the cores. Nevertheless, IR-dark structures can in principle be considered as prestellar core candidates (e.g., *Sanhueza et al.* 2019), though most of the IR-dark studies are at clump scales.

4.1.2. Molecular Line Surveys of Dense Gas

In the past years, high-resolution and wide-coverage molecular line surveys of intermediate and higher density gas tracers have been performed in nearby star-forming regions, the Galactic plane, and toward the Galactic center to complement ongoing surveys of dust continuum emission. These line surveys provide the necessary kinematic information required to fully assess the stability of cores and filaments, identify rotation and evaluate the evolution of angular momentum from large to small scales, and investigate the role of accretion in the mass evolution of filaments and cores.

The kinematic transition from cloud to filament and core has often been traced by rotational line emission from CO and CO isotopologues, such as ^{13}CO and C^{18}O, at millimeter to submillimeter wavelengths. Toward some Gould Belt clouds, JCMT GBS observations of the CO and isotopologues of the (3–2) rotational transitions ($\approx$14$''$ resolution) were used to examine the interaction between outflows and star-forming gas (*White et al.* 2015; *Drabek-Maunder et al.* 2016), and informed virial analyses of dense cores identified in these regions (*Pattle et al.* 2015). In order to resolve spatially individual cores along with their kinematics, surveys like the CARMA-NRO Orion survey (*Kong et al.* 2018) use a combination of interferometer and single dish observations to discern structures on 8$''$ (3300 au) scales in the Orion molecular cloud, while retaining sensitivity to large-scale structures. Toward more distant regions, single dish CO surveys such as the FOREST unbiased Galactic plane imaging survey with the Nobeyama 45-m telescope (FUGIN; *Umemoto et al.* 2017) are sensitive to molecular gas clumps on scales of $\sim$ 1 pc, and masses $\sim$ 100 $M_\odot$ at

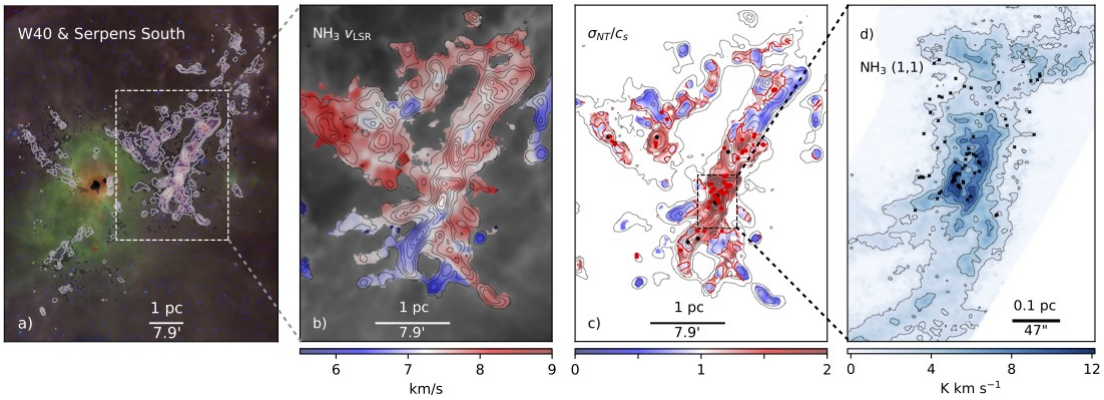

Fig. 12.— Zooming in on the W40 and Serpens South star-forming regions: a) WISE 22 μm, 12 μm, and 4.6 μm (RGB), overlaid with $N(\mathrm{H_2})$ (grayscale; *Herschel* GBS) and $\mathrm{NH_3}$ integrated intensity contours (white; GAS) at 32″ (0.07 pc) resolution. b) $N(\mathrm{H_2})$ (grayscale; *Herschel* GBS) and $\mathrm{NH_3}$ integrated intensity contours (gray; GAS), with $\mathrm{NH_3}$-derived v_{LSR} (colorscale). c) Ratio of non-thermal velocity dispersion to sound speed in $\mathrm{NH_3}$, adapted from *Friesen et al.* (2016). d) Dense gas surrounding the Serpens South young stellar cluster in $\mathrm{NH_3}$ (1,1) at 5″ (0.01 pc) resolution (*Friesen et al.*, in prep), highlighting dense cores and compact substructures within filaments. Millimeter sources detected with ALMA are shown (*Plunkett et al.* 2018). In all plots, a distance of 437 pc is assumed (*Ortiz-León et al.* 2018).

10 kpc.

More recently, sensitive $\mathrm{NH_3}$ observations by the Green Bank Ammonia Survey (GAS; *Friesen et al.* 2017) have enabled analysis of the cloud-core transition in a single dense gas tracer ($n_{\mathrm{eff}} = 7.9 \times 10^2$ cm^{-3} to produce a 1 K km s^{-1} spectral line at $T = 15$ K; *Shirley* 2015). GAS takes advantage of the multiple-pixel K-band Focal Plane Array (KFPA) at the 100-m Green Bank Telescope to survey nearby star-forming regions within ~ 500 pc at 32″ angular resolution (0.02 pc to 0.07 pc spatial resolution), with a total areal coverage of nearly four square degrees across ~ 12 clouds (*Pineda et al.* in prep.; *Friesen et al.* 2017; *Keown et al.* 2017; *Redaelli et al.* 2017). These high sensitivity observations show substantial evidence for multiple velocity components in the dense gas (*Chen et al.* 2020c; *Choudhury et al.* 2020, 2021). While past observations revealed a sharp transition between the supersonic molecular cloud and the quiescent dense core (*Pineda et al.* 2010), wider-scale mapping has shown that larger areas of subsonic linewidth are also identified in dense gas within low-mass star forming regions (*Friesen et al.* 2016, see Fig. 12). Furthermore, kinematic transitions between the turbulent cloud and dense core may be more gradual, shown by fitting of multiple velocity components across core edges in L1688 (*Choudhury et al.* 2021, see also Sect. 4.2.2 below).

Using Serpens South as an example, Fig. 12 compares the spatial distribution of dust (traced by thermal continuum emission) and dense gas (traced by $\mathrm{NH_3}$; *Friesen et al.* 2016, 2017) from cloud to core scales, and demonstrates the correlation between YSOs (traced by high-resolution millimeter continuum emission observed with ALMA) and dense cores of the hub-filament system. The gas kinetic information traced by $\mathrm{NH_3}$ also reveals the transition from super- to sub-sonic gas motions over extended scales in filaments and around the dense cores (panel c), although as noted above, these transitions from supersonic turbulence to quiescent, velocity-coherent cores may not be as sharp as expected based on these maps.

Using the same tracer, the KFPA Examinations of Young STellar Object Natal Environments (KEYSTONE; *Keown et al.* 2019) mapped $\mathrm{NH_3}$ (and $\mathrm{H_2O}$ maser) emission toward more distant high mass star forming regions, while the Radio Ammonia Midplane Survey (RAMPS; *Hogge et al.* 2018) targeted portions of the Galactic plane. The angular resolution of these single dish studies is less able to resolve individual cores at kpc distances, however.

The CARMA (Combined Array for Research in Millimeter-wave Astronomy) Large Area Star Formation Survey (CLASSy; *Storm et al.* 2014) probe higher density material in emission from $\mathrm{N_2H^+}$ (1–0), with $n_{\mathrm{eff}} = 6.7 \times 10^3$ cm^{-3}. Utilizing the high angular resolution ($\approx 7''$ at ~ 90 GHz) and sensitivity at a wide range of spatial scales of CARMA, CLASSy mapped subregions in the Perseus and Serpens Molecular Clouds to cover a range of star-forming activity levels (*Storm et al.* 2014; *Lee et al.* 2014b; *Fernández-López et al.* 2014; *Storm et al.* 2016). Further investigations toward five subregions covered by CLASSy are presented in *Dhabal et al.* (2018) as CLASSy-II, which combined lines covered by CLASSy ($\mathrm{N_2H^+}$, HCN, and $\mathrm{HCO^+}$) with additional optically thin dense gas tracers $\mathrm{H^{13}CO^+}$ and $\mathrm{H^{13}CN}$ to test whether the observed kinematics in CLASSy represents the bulk property of the material making up the filaments. In general, both the CLASSy and CLASSy-II observations support the existence of finer structures within dense filaments and the presence of velocity gradients across them (see e.g., Sect. 3.1 and Fig. 6).

Other high-resolution, wide-coverage maps provide a coherent picture of the gas dynamics in both nearby (e.g.,

Hacar et al. 2018) and Galactic (e.g., *Sokolov et al.* 2018) star-forming regions. Combining several molecular lines, including ^{13}CO and C^{18}O for larger-scale diffuse gas, and N_2H^+, HCO^+, SO, and CS, the TRAO (Taeduk Radio Astronomy Observatory) survey of Filaments, the Universal Nursery of Stars (FUNS) aims to provide complete pictures of the kinematics and chemistry in filaments and cores within 10 Gould Belt Clouds with $\approx 50''$ angular resolution at ~ 100 GHz (*Chung et al.* 2019, 2021). In L1478 in the California molecular cloud, cores traced by N_2H^+ tend to lie in supercritical filaments as expected, but differ in how well their kinematic properties match that of their embedding filaments (*Chung et al.* 2019). Systematic shifts seen in core $v_{\rm LSR}$ as traced by N_2H^+ and C^{18}O in hub systems differ from previous results in the Perseus molecular cloud (*Kirk et al.* 2007). Kinematic studies such as these suggest core formation in filaments may follow multiple mechanisms, depending on the environment.

4.2. Core-environment Interaction

4.2.1. Defining Core Boundaries

Different methods have been developed to identify and isolate the emission from dense molecular cores, and they are applied to continuum or spectral line data, involving both 2D images and 3D data cubes. Since many stars form in complex, clustered environments (see reviews by *Krumholz et al.* 2014; *Reipurth et al.* 2014), disentangling emission from cores from that of their parent clouds, including complex large-scale background and filamentary structures, can be challenging. The assignment of emission to one source compared with another, and the method of assessment of background vs. source flux, among other algorithmic decisions, can thus affect strongly the derived core properties, including radius and mass, although to date systematic comparisons of different methods are rare, partly because different methods are best matched to regions of varying complexity.

Previous methods introduced in *André et al.* (2014) for extracting sources in *Herschel* continuum data included CuTEx (Curvature Thresholding Extractor; *Molinari et al.* 2011), CSAR (Cardiff Sourcefinding AlgoRithm; *Kirk et al.* 2013b), and `getsources` (*Men'shchikov et al.* 2012). CuTEx assesses curvature via second-order differentiation of the image brightness in, e.g., thermal continuum emission maps. This allows the disentanglement of closely-spaced, compact sources in clustered environments, but is less likely to detect unbound, more diffuse objects than `getsources` (*Bresnahan et al.* 2018), where multi-wavelength images are spatially-filtered and background-subtracted to identify sources of interest. Deblending of apparently overlapping sources in the image plane is enabled by `getsources`, as well as by dendrogram algorithms like `astrodendro` (*Rosolowsky et al.* 2008) in velocity space when applied to 3D position-position-velocity molecular line emission cubes. Other than in `getsources`, emission is assigned to individual sources at each pixel (or voxel, in `astrodendro`), following various thresholding or segmentation rules. More recently, *Berry* (2015) introduced `FellWalker`, which defines the peaks and boundaries of sources based on local gradients.

We note that the most appropriate method for identifying structures depends on the data and science goals. Generally speaking, with *Herschel*'s multi-wavelength data, `getsources` is preferred (e.g., *Könyves et al.* 2015, 2020; *Marsh et al.* 2014, 2016), while `FellWalker` could provide better estimate on core boundaries when cores are well-separated, as in the case of JCMT GBS (*Kirk et al.* 2016; *Mowat et al.* 2017). Though `getsources` only returns the elliptical footprint of the core area instead of the actual boundary as provided by `FellWalker`, uncertainties in core boundary results in only a factor of a few error in mass estimation (for density profile following $\rho(r) \propto r^{-2}$, and thus mass $m(r) \propto r$) and thus `getsources` may be preferred for CMF/IMF studies because of its better performance on finding small cores in clustered environment. In particular, *Lane et al.* (2016) applied both `getsources` and `FellWalker` on their JCMT Orion A data, and concluded `getsources` is more robust on highlighting small, compact cores when there is substantial background emission. Also, as demonstrated in *Goodman et al.* (2009) and *Storm et al.* (2014), clump-finding algorithms like `Cloudprops` (*Rosolowsky and Leroy* 2006) and `clumpfind` (*Williams et al.* 1994) work best for small-scale segmentation in sparse fields that have resolved separations between objects, while dendrogram-type analysis is more appropriate to study features across a wide range of spatial scales.

With the complex filamentary structures in star-forming regions revealed by recent observations, background subtraction becomes an important topic in core definition, particularly since dense, potentially prestellar cores are strongly associated with filaments (see §3.4). Also, filamentary structures that overlap with noisy fluctuations could appear to be core-like, which further introduces complications for source extraction routines (*Men'shchikov* 2013). Indeed, numerous algorithms have been developed and adopted to identify and characterize filamentary structures in both the diffuse ISM and dense molecular clouds in recent years, including the Rolling Hough Transform (RHT; *Clark et al.* 2014), Discrete Persistent Structures Extractor (DisPerSE; *Sousbie* 2011), `getfilaments` (as part of the `getsources` package; *Men'shchikov* 2013), FilFinder (*Koch and Rosolowsky* 2015), template matching (TM; *Juvela* 2016), and `RadFil` (*Zucker and Chen* 2018). However, these routines generally work independently of the core identification algorithms, and a joint approach like `getsf`, a recent improvement of `getsources` and `getfilaments` (*Men'shchikov* 2021), is desirable.

Because the strength of molecular line emission depends on density along with the total column density, maps of different molecular line transitions are biased toward varying ranges in density and column density. Applying source extraction algorithms to line emission from the denser gas

tracers described above therefore can simplify the identification and disentangling of core emission from the environment, as there is less contamination from diffuse gas along the line of sight. Spectral line observations also allow for core identification in one additional dimension (i.e., the position-position-velocity, or PPV space). This functionality is available for PPV data cubes in both `clumpfind` (*Williams et al.* 1994) and `astrodendro` (*Rosolowsky et al.* 2008), and each have been widely adopted (e.g., *Ikeda et al.* 2007; *Friesen et al.* 2009; *Duarte-Cabral et al.* 2012; *Keown et al.* 2017; *Nakamura et al.* 2017; *Takemura et al.* 2021). Alternatively, *Storm et al.* (2014) developed a new non-binary dendrogram algorithm to allow for grouping more than two objects, thus providing a more statistically meaningful way to represent hierarchical structure. This approach has been adopted in follow-up studies using the isolated hyperfine component of N_2H^+ from the CLASSy survey (*Lee et al.* 2014b; *Storm et al.* 2016).

While identifying structures in PPV space could be more desirable because of the additional dimension of information, structures in PPV space may not always be consistent with actual three-dimensional structures (in position-position-position, or PPP space; e.g., *Ballesteros-Paredes and Mac Low* 2002; *Burkhart et al.* 2013; *Beaumont et al.* 2013; *Clarke et al.* 2018). Furthermore, the hyperfine structures in the emission lines of traditional dense gas tracers like N_2H^+ and NH_3 can make structure identification in PPV space less sensitive. In some cases, structure analyses can be applied to single, isolated hyperfine components (e.g., in the N_2H^+ 1–0 line). In other cases, the hyperfine line structure can be fit assuming initially a single velocity component, and a data cube reconstructed with a single Gaussian line (e.g., NH_3). In practice, many structure analyses of molecular line observations still identify cores in the integrated intensity maps (e.g. *Chen et al.* 2019b).

In simulations, the complete 3D information in principle makes defining the core boundaries more straightforward. Core-defining methods in theoretical studies are therefore more diverse, as most theoretical works either prescribed their own core-identification routines (e.g., *Gammie et al.* 2003), or focused on the properties and/or evolution of the star-forming gas in general instead of highlighting cores. In general, methods based on density contours are the most common, like the popular `clumpfind` (e.g., *Padoan et al.* 2007; *Schmidt et al.* 2010; *Bleuler and Teyssier* 2014; *Li et al.* 2015; *Pelkonen et al.* 2021). In contrast, `astrodendro` was mostly used in simulations for characterizing the hierarchy structures instead of defining cores (*Beaumont et al.* 2013; *Burkhart et al.* 2013), with a few exceptions (*Smullen et al.* 2020; *Clarke et al.* 2020). On the other hand, *Dib et al.* (2007) developed a clump-finding algorithm based on a density threshold criterion and a friends-of-friends approach. This is similar to the HOP algorithm (*Eisenstein and Hut* 1998) adopted in *Hennebelle* (2018), *Ntormousi and Hennebelle* (2019), and *Hennebelle et al.* (2019), though *Hennebelle et al.* (2019) pointed out that these "cores" may be too dense and clustered compared to observed cores. Alternatively, the core-finding method GRID-core (Gravitational potential Identification of cores) uses the contours of the local gravitational potential to identify core boundaries (*Gong and Ostriker* 2011; *Chen and Ostriker* 2014, 2015, 2018; *Gong and Ostriker* 2015), because the gravitational potential is more directly linked to the fundamental physics during core evolution. A similar approach was adopted by *Smith et al.* (2009), who noted that using the gravitational potential instead of density yields smoother core boundaries. Last but not least, recent work by *Kuznetsova et al.* (2018, 2019, 2020) considered "sink patches" to record gas properties in the immediate surrounding of the sink particles in the simulations, which in principle resemble star-forming cores.

4.2.2. *Stability and Evolution of Dense Cores from Observations*

The stability of starless and prestellar cores is often assessed via a virial analysis, where the second derivative of the moment of inertia $\ddot{I}$ is given by

$$\frac{1}{2}\ddot{I} = 2\Omega_K + \Omega_G + \Omega_M + \Omega_P \,, \tag{1}$$

and Ω_K, Ω_G, Ω_M, and Ω_P are the internal energy, gravitational potential energy, magnetic energy, and energy due to external pressure, respectively. The gravitational and external pressure terms are negative, while the internal energy and magnetic energy terms are positive. A core is considered to be virially unstable and may collapse if $\ddot{I} < 0$.

In practice, most often a comparison is made between the internal and gravitational potential energy terms only, and the virial parameter $\alpha_{\rm vir}$ defined for a core of mass M and radius R such that $\alpha_{\rm vir} = 5\sigma_v^2 R/a\,GM$ (*Bertoldi and McKee* 1992), where σ_v is the velocity dispersion of the core, and can include thermal motions only, or thermal and non-thermal contributions if kinematic data are available; and a is a correction factor of order unity that accounts for the radial density profile ($a = 1$ for uniform density spheres and $a = 1.22$ for a critical Bonnor-Ebert sphere (BES); see *Singh et al.* 2021).

Given the recent availability of large surveys of matched continuum and molecular line data toward many nearby clouds described in Sect. 4.1, studies have begun to address the full virial equation to investigate core stability (*Pattle et al.* 2015; *Seo et al.* 2015; *Pattle* 2016; *Kirk et al.* 2017b; *Chen et al.* 2019b; *Kerr et al.* 2019). When including (presumed supportive) non-thermal motions in the full analysis, the internal kinetic energy term is not balanced by the gravitational term for many cores in nearby clouds, and they are instead bound by the external pressure (e.g., *Kirk et al.* 2017b; *Kerr et al.* 2019). In most studies, the external pressure is assumed to be a confining pressure derived from turbulent motions in the embedding cloud, but *Gómez et al.* (2021) point out that it can also be interpreted as ram pressure from a collapsing, larger-scale envelope. We do not address the contributions from magnetic fields in detail here, although recent polarization surveys are starting

to probe core-scale magnetic field structures across multiple regions. Instead, we refer the reader to recent reviews of the state-of-the-art theory and observations of magnetic fields in *Hennebelle and Inutsuka* (2019), *Pattle and Fissel* (2019), *Pudritz and Ray* (2019), and Pattle *et al.* in this volume.

Chen et al. (2019b) identified a set of 'coherent cores' in GAS NH_3 data toward the Ophiuchus and Taurus molecular clouds that were defined by both peaks in H_2 column density as well as an observed transition in the size-linewidth relation (the 'transition to coherence'; *Goodman et al.* 1993; *Pineda et al.* 2010). These selection criteria identify a subset of core-like sources that appear confined by external pressure, rather than bound virially by their self-gravity. This subsonic velocity dispersion in high-density regions has also been reported in numerical simulations (*Gong and Ostriker* 2011), who pointed out that such feature could be due to a combination of low post-shock velocities and the spatially limited scale highlighted by density.

Turbulence sometimes dissipates on much broader scales, however, as indicated by chains of velocity-coherent cores in the Taurus L1495/B213 filament (*Tafalla and Hacar* 2015) and larger-scale deviations from the size-linewidth relation in filaments. Moreover, *Pineda et al.* (2021) found that within the velocity-coherent core Barnard 5, the ions (traced by N_2H^+) display a higher level of turbulence than neutrals (traced by NH_3). Assuming these two molecules trace similar volumes, this can be explained if the magnetic field within Barnard 5 is oscillating. Since the ions are more strongly coupled to the magnetic field, this would produce a larger velocity dispersion in N_2H^+. Better understanding toward the decay and transport of turbulence in core-forming regions is still needed.

Several analyses, focused on high-mass (and more distant) star forming regions, reported very low values ($\ll 1$) of the virial parameter (*Kauffmann et al.* 2013; *Urquhart et al.* 2014; *Traficante et al.* 2018a,b; *Keown et al.* 2019). This result would imply that these objects are not in equilibrium and that they would last for a fraction of the free-fall time. However, *Singh et al.* (2019) introduced a method to measure more directly the gravitational term from H_2 column density maps, negating the need to quantify a core radius. Applying this method to Gould Belt clouds mapped by both the HGBS and GAS, *Singh et al.* (2021) show that by including bulk motion in the kinematic term, larger cores and clumps have virial parameters closer to the stable value. This result shows that it is easy to underestimate the virial parameter, and provides a potential solution to the very low values of the virial parameter previously reported.

The observational result that many cores do not appear gravitationally bound may seem to be in conflict with models of core formation via gravitational instability of nearly isothermal filaments discussed in the previous section, but gravitational instability models proposed for self-gravitating prestellar cores are not inconsistent with the view that unbound cores form via turbulent cloud motions in the first place and a fraction of them grow (and eventually collapse) by gravitational instability. Based on MHD simulations, *Chen et al.* (2020b) propose that the pressure-confined, coherent objects represent an early phase in core evolution, where dense structures form via turbulent cloud motions, turbulence dissipates within the dense structures, and some fraction become gravitationally unstable and eventually collapse (see also *Seo et al.* 2015; *Pattle* 2016). Core formation in simulations is discussed in more detail in the following section.

4.2.3. *Core Formation and Evolution in Simulations*

It is well-established that dense cores are mostly associated with filaments (see the review by *André et al.* 2014, and §3.4). This lends support to the core formation scenario that supercritical filaments would fragment longitudinally into cores, or groups of cores (see Sect. 3 for details). This filament-fragment-to-core model has been studied extensively using both analytic approaches (*Inutsuka and Miyama* 1992, 1997; *Inutsuka* 2001; *Lee et al.* 2017) and numerical simulations (*Seifried and Walch* 2015; *Gritschneder et al.* 2017; *Clarke et al.* 2017, 2020). Numerical simulations of accreting filaments showed that the fragmentation behavior can either grow from internal perturbation of an accreting filament (*Clarke et al.* 2016) or originate from the clumpy nature of the accreting turbulent gas (*Clarke et al.* 2016, 2017). Indeed, the growth of structures could be enabled by nonlinear perturbations induced by turbulence at all scales. Several kinematic and structural studies of star-forming clouds also suggest that these systems may be undergoing global collapse (e.g., *Beuther et al.* 2015b; *Csengeri et al.* 2017; *Hacar et al.* 2017b; *Barnes et al.* 2018b; *Jackson et al.* 2019; *Treviño-Morales et al.* 2019; *Nony et al.* 2021). *Vázquez-Semadeni et al.* (2019) elucidate these multiscale, non-homologous collapses with scale-dependent timescales as the scenario of global hierarchical collapse (GHC). In this picture, structures are continuously feeding their substructures while they accrete from their parent structures (see also *Gómez and Vázquez-Semadeni* 2014; *Naranjo-Romero et al.* 2015; *Vázquez-Semadeni et al.* 2017).

While the geometry differs, the GHC scenario is consistent with recent simulation results that dense cores and filaments develop simultaneously (e.g., *Chen and Ostriker* 2014, 2015; *Van Loo et al.* 2014; *Gong and Ostriker* 2015), in contrast to the two-step, filament fragmentation scenario that has long been adopted in semi-analytic static models. In particular, the anisotropic contraction model described in *Chen and Ostriker* (2014, 2015) enables rapid core formation even in strongly magnetized media and without ambipolar diffusion, consistent with the abundant observational examples of magnetically supercritical cores.

While numerical simulations on star formation have been significantly improved in the past decade, theoretical investigations on simulated dense cores are relatively sparse. Since numerical simulations are limited by finite resolution, insertion of sink particles has become a com-

mon practice to replace the densest structures in simulations (e.g., *Hubber et al.* 2013; *Bleuler and Teyssier* 2014). With star formation being the primary interest in most of the numerical works, detailed structures of the dense gas (which could be identified as cores) are not necessarily analyzed even when dense cores were identified during the course of the simulation in order to evaluate sink insertion and accretion (e.g., *Ballesteros-Paredes et al.* 2015; *Bertelli Motta et al.* 2016; *Lee and Hennebelle* 2018; *Bate* 2019). In addition, spatial resolution at sub-pc scale is necessary for proper star-forming core identification and inspection, which is computationally expensive to achieve in large-scale, cluster-type simulations constructed at a few tens of pc (e.g., *Lee and Hennebelle* 2016; *He et al.* 2019). By far, few numerical simulations have covered such wide dynamic ranges (see e.g., *Padoan et al.* 2016; *Kuffmeier et al.* 2018; *Grudić et al.* 2021; also see Sect. 5.2.2).

Some cluster-type simulations have identified dense cores and analyzed their statistical properties (*Padoan et al.* 2001; *Galván-Madrid et al.* 2007; *Smith et al.* 2009; *Hennebelle* 2018; *Ntormousi and Hennebelle* 2019; *Pelkonen et al.* 2021), with the goal of providing a potential link between the CMF and the IMF. However, few existing works have tried to actually link the properties of the cores to those of the stars. *Kuznetsova et al.* (2018) analyzed the gas "patches" from which sink particles accrete and explain the outcome of the stellar mass spectrum as a consequence of Bondi-Hoyle accretion from the reservoir. *Colman and Teyssier* (2020) identified tidally protected regions around newly-formed sink particles and found a good correlation with the final mass of the stars. Nonetheless, *Pelkonen et al.* (2021) analyzed bound cores around sink particles from simulations described in *Haugbølle et al.* (2018) and suggested that the final mass of sink particles, though exhibiting a correlation with the reservoir mass, accretes not only from the bound reservoir and does not accrete the totality of the latter either (e.g., *Smith et al.* 2009). This is in line with the mass accretion scenario proposed in *Padoan et al.* (2020), that the final stellar mass is dominated by pc-scale turbulent flows instead of the mass of the parent core. However, it is worth noting that *Padoan et al.* (2020) focused on massive star-forming cores which, because of the significant feedback effects, shall have weaker correlation between core mass and stellar mass compared to low-mass regime (see e.g., *Beuther et al.* 2007).

4.3. Dynamic Properties of Dense Cores

4.3.1. Infall

Those subset of cores that become gravitationally unstable should then collapse to form protostars. Core collapse models have been developed both analytically and numerically. Self-similar solutions of spherically symmetric starless core collapse predict the infall velocity evolution and mass accretion rates given initial density profiles. *Whitworth and Summers* (1985) showed that broad families of self-similar solutions, including the Larson-Penston (LP) model (*Larson* 1969; *Penston* 1969), and the singular isothermal sphere model (SIS; *Shu* 1977), can be described by two parameters that reflect the initial gravitational instability of the core, and the significance of the external bounding pressure. Models that are initially stable against collapse, with little influence due to external pressure, evolve quasi-statically toward instability. Contraction motions in an initially unstable core will be enhanced by external compression, leading to more rapid evolution and larger infall speeds. Since measured core density profiles tend to follow the common $\rho \propto r^{-2}$ profile at larger radii, testing theoretical collapse scenarios requires high spatial resolution to resolve and model the inner density and velocity profiles.

From observed molecular line emission profiles, it is difficult to get a direct indication of gravity-driven infall, because rotation and outflows may also produce comparable kinematic signatures, and the interpretation usually depends on comparisons to numerical models that involve various assumptions on gas properties (density, temperature, chemical abundance, etc.). However, it has long been proposed that the opaque infalling gas in the foreground cloud could generate redshifted absorption against the continuum emission from the central protostar. The resulting *inverse P-Cygni profile*, with emission on the blueshifted side of the central velocity and absorption on the redshifted side, can therefore be used as an unambiguous indicator of inward motion of the foreground matter (*Leung and Brown* 1977).

In general, starless and protostellar cores show more evidence for inward rather than outward motions (*Mardones et al.* 1997; *Lee and Myers* 2011), with largely subsonic infall speeds where measured. In pointed, single-dish line surveys, between 10% and 25% of starless cores in nearby molecular clouds show blue-shifted line asymmetries indicative of infall or inflow (*Lee et al.* 1999, 2004; *Sohn et al.* 2007; *Tsitali et al.* 2015; *Campbell et al.* 2016), although these studies do not all have common core selection criteria. In a broad survey of cores in Perseus, *Campbell et al.* (2016) find that starless cores more massive than their Jeans mass are more likely to show infall line signatures. *Keown et al.* (2016) show that measured infall speeds vary with tracer and position across low mass cores L492, L694-2, and L1521F, as is expected for several contracting core scenarios, such that the true magnitude of the infall motions may not be accurately measured via single-pointing surveys.

The identification of inward and outward gas motions via the detection of blue- or red-shifted, self-absorbed optically thick emissions relative to an optically thin counterpart, however, relies on high-enough spatial resolution to reduce the contamination from outflows and foreground large-scale clouds (*Di Francesco et al.* 2001), and thus has thrived as ALMA became available (e.g., *Pineda et al.* 2012; *Lee et al.* 2014a; *Evans et al.* 2015; *Mottram et al.* 2017; *Su et al.* 2019). With ALMA, we are now better able to probe the structure and kinematics of the innermost regions of dense cores, potentially identifying the infall velocity at the radius where the density profile transitions be-

tween distinct radial power-law slopes ($\sim 10^2 - 10^4$ au) to test collapse model predictions. Toward more evolved, protostellar cores, *Maureira et al.* (2017) identify both rotation and infall in the First Hydrostatic Core (FHSC) candidate L1451-mm at 1000 au scales with ALMA, again finding subsonic infall speeds of ~ 0.17 km s^{-1} (see also *Tsitali et al.* 2013).

Note that radiative transfer modeling of the protostellar envelope with chemical abundance profiles of the corresponding molecules is still required to properly constrain the infall kinematics from the observed line profile (e.g., *Yang et al.* 2020). Measurements of infall speeds through the inverse P-Cygni technique range from subsonic to supersonic, with values ~0.4–0.8 km s^{-1} at $r \sim 100$ au toward some sources (*Pineda et al.* 2012; *Su et al.* 2019). Detailed measurements of infall speeds as a function of radius will help constrain collapse profiles. Toward B335, HCN and HCO$^+$ line profiles at 50 au scales are fitted well by an inside-out collapse model where $v_{\rm inf} \propto r^{-0.5}$ (*Evans et al.* 2015).

Moving toward more detailed infall analyses, *Keto et al.* (2015) predict the emission line profiles of H_2O (1_{10}–1_{01}) and $C^{18}O$ (1–0) in the prestellar core L1544 for several core collapse models, and find only the quasi-static contraction of an initially unstable BES is in agreement with observations. In this model, the maximum infall velocity remains subsonic, and infall motions extend $\sim 1.6\times10^4$ au (0.08 pc) across the core. Similarly, *Koumpia et al.* (2020) use radiative transfer modeling of several infall models to predict line profiles of dense gas tracers N_2H^+ and H_2D^+ across several starless cores. They find that while the SIS model is clearly a poor match to cores without central point sources, a larger survey is needed to discern between other core contraction models.

4.3.2. *Rotation*

Rotation is critical in the core collapse process leading to the creation of protostellar systems. A well-known problem is that molecular cloud cores have far greater angular momentum (by 6–7 orders of magnitude) than is measured in individual stars (*McKee and Ostriker* 2007). Indeed, if angular momentum conservation holds during core collapse, large disks develop very fast (before the Class 0 stage) in hydrodynamic simulations, in contradiction with observations (e.g., *Maury et al.* 2010; *Segura-Cox et al.* 2018; *Maury et al.* 2019). Magnetic braking has been considered as the main mechanism for cores to lose angular momentum, but it can be too efficient, such that no disk could form during core collapse and protostellar formation. Non-ideal MHD effects could provide a way to allow for the decoupling between core material and magnetic field (see the review by *Li et al.* 2014b). The angular momentum of dense cores, L, is therefore an important quantity in shaping the outcome of subsequent evolution.

The size-dependence of the total specific angular momentum, $J \equiv L/M$, at sub-pc scales ($\sim 0.01-1$ pc) within cores and clumps is long-known and well-established from early observations (*Goodman et al.* 1993; *Caselli et al.* 2002; *Pirogov et al.* 2003). Recent interferometric observations (*Chen et al.* 2007; *Tobin et al.* 2011; *Yen et al.* 2015b) and numerical simulations (*Chen and Ostriker* 2018) confirmed and extended this trend down to scales ~ 0.001 pc. These studies revealed a power-law correlation between J and the core size, R, such that $J \propto R^\alpha$, with $\alpha \approx 1.5$ (see the left panel of Fig. 13; also see reviews by *Belloche* 2013 and *Li et al.* 2014b).

The $J - R$ correlation over three orders of magnitude in spatial scales is puzzling, and may suggest that gas motion in cores originates at scales much larger than the core size (*Walch et al.* 2010; *Chen and Ostriker* 2018). This is inconsistent with the classical theory, which envisioned cloud cores to form after losing magnetic and turbulent support from the cloud material (*Shu et al.* 1987). In fact, in addition to the $J - R$ correlation, the ratio between rotational energy and gravitational energy (β_E; see the definition in *Goodman et al.* 1993) is typically ~ 0.02 and is relatively independent of core/clump size. *Chen and Ostriker* (2018) estimated the rotational-to-kinetic energy ratio in simulated cores, and found that the ratio between rotational energy and the total gas kinetic energy, $E_{\rm rot}/E_K \sim 0.1$ on average, is also independent of core/clump size. These results show that rotation is not dominant dynamically within dense cores.

Calculations of J, as in Fig. 13 (left), generally assume a constant density for the core, which may contribute to the scatter in the observed data points if the included cores have varying radial density profiles. In addition, linear fitting of the observed velocity gradient across individual cores is commonly adopted to estimate the core's angular momentum, which is based on the assumption of rigid-body rotation. However, recent high-spectral resolution ($\Delta v \approx 0.025$ km s^{-1}) observations by *Chen et al.* (2019a) found that while the fitted linear velocity gradients across their dense core targets nicely agree with the $J \propto R^{1.5}$ correlation (see the colored symbols in the left panel of Fig. 13), the detailed gas structures in the PV space are not consistent with rigid-body rotation (see also *Belloche et al.* 2002). Magnetic braking is especially important at r <1000 au, and therefore these observations give support to turbulence (or some cloud-core interaction) as the main driver of the core's angular momentum, which we discuss in more detail later (Sect. 4.3.3).

Instead of using a single-value estimate of total angular momentum for the entire core, observing the spatial and temporal evolution of angular momentum within one core is more challenging but has become feasible recently. Early work by *Yen et al.* (2010, 2011) combined multiple observations with different molecular lines to probe the radial profile of the specific angular momentum within individual cores, $j(r) = r \times \delta v$, in the B335 Bok globule. In the case of rigid-body rotation and uniform density the total specific angular momentum corresponds to the radial specific angular momentum at that scale, $J = j(R)$, while for other cases

there is a normalization correction (see *Pineda et al.* 2019). While the data points were sparse, the transition from rotation ($j \propto r^{\alpha}$) to infall ($j \approx$ constant) was clear, which was later confirmed with numerical modeling (*Kurono et al.* 2013) and extended to ~ 10 au scale by additional ALMA observations (*Yen et al.* 2015a). *Ohashi et al.* (2014) also reported that the $j(r)$ profile of the inner core is almost flat for L1527 IRS down to 54 au.

While interferometers like ALMA and SMA provide the necessary angular resolution at high frequencies ($\gtrsim 100$ GHz) for studying gas kinematics at $10 - 10^3$ au scales (e.g., *Yen et al.* 2013, 2017; *Tobin et al.* 2018), observations toward the innermost envelopes (~ 5000 au or 0.01 pc) are difficult because of the dynamic range needed over broad spatial scales. *Pineda et al.* (2019) re-analyzed NH_3 data from VLA, and resolved the complete radial profile of the specific angular momentum $j(r)$ in three young objects down to several hundreds of au. The inferred angular momentum profile follows a relation $j \propto r^{1.8}$, indicating that the core is close to rigid-body rotation ($j \propto r^2$) while the imprint from the initial turbulence is still present. More recently, *Gaudel et al.* (2020) combined IRAM PdBI and 30-meter observations with two molecular lines to probe dense gas kinematics in 12 protostellar envelopes between ~50–5000 au. They found a similar trend that $j \propto r^{1.6}$ above 1600 au and $j \approx$ constant between 50–1600 au.

We note that angular momentum conservation during the collapse is usually invoked as a simple explanation for the regime with flat j distribution, while *Takahashi et al.* (2016) proposed a model that considers the widening of the region during the collapse to account for a regime of constant angular momentum regardless of its initial distribution. On the other hand, measurements of velocity gradient at 1000 au scale around young objects do present a wide range of angular momentum, showing possible varieties of disk-forming conditions (e.g., *Yen et al.* 2015b). Nevertheless, the observed angular momentum could have large uncertainties due to projection effects, as suggested by *Zhang et al.* (2018) via synthetic observations.

4.3.3. The origin of angular momentum in cores

There are various proposals for the origin of angular momentum at the core scale, which are not mutually exclusive. We roughly categorize them into (1) anisotropic accretion, (2) large-scale rotation in the parent structure, and (3) local turbulence.

Kuznetsova et al. (2019, 2020) followed the angular momenta within the immediate surrounding of forming protostars in both HD and MHD simulations, and concluded that episodic accretion from filaments onto cores induced by multi-directional flows around the cores dominates the gas dynamics at core scales. This suggests the star-forming environment is highly heterogeneous, which has been noted in previous simulations by *Kuffmeier et al.* (2017, 2018). Considering that cores form from filament fragmentation, *Misugi et al.* (2019) proposed a model that conserves the angular momentum originated from larger scales during the anisotropic contraction that forms the filaments and the further axial fragmentation that leads to the formation of cores. They pointed out that the observed specific angular momentum within cores could be reproduced by simulated cores formed from filament fragmentation if the velocity structure within the filament follows a one-dimensional Kolmogorov power spectrum or with an anisotropic model with more power in the transverse direction.

Observations have shown stellar spin alignment in some open clusters (*Corsaro et al.* 2017; *Kovacs* 2018), and coherent global rotation was shown for one of those clusters (*Kamann et al.* 2019). Nevertheless, numerical simulations suggest that the stellar spin alignment happens only when the global rotation of the star-forming clump is significant with respect to the turbulence (*Corsaro et al.* 2017). Alternatively, alignment could also occur within sub-clusters if the rotation at larger scales is less important (*Rey-Raposo and Read* 2018). Furthermore, if core-embedding filaments have non-zero angular momenta as suggested by a recent observation (*Hsieh et al.* 2021), it is possible that cores inherit rotation from their parent filaments. This behaviour is consistent with the observations of the massive infrared dark cloud G28.37+0.07, where outflows (as a proxy of rotation axis) are aligned mostly perpendicular to the parent filaments (*Kong et al.* 2019).

However, angular momenta within cores do not seem to always align with the large-scale rotation. For example, the rotating cores in the Orion A cloud do not seem to be correlated to the rotation of the large-scale filament (*Tatematsu et al.* 2016). In general, protostellar outflows (which are theoretically perpendicular to the disk plane) are not aligned with their parent structures (*Stephens et al.* 2017) and ambient magnetic field directions (*Hull et al.* 2013). The same rotation-magnetic field misalignment is also found in simulated cores by *Chen and Ostriker* (2018), who concluded that cores must acquire rotational motions from local turbulence so that their rotational axes are independent of the magnetic field directions. This is consistent with the results discussed in *Kuznetsova et al.* (2019), who showed that the angular momenta of individual cores are not strongly affected by the rotation of the parent cloud. *Hennebelle* (2018) also pointed out that core rotation may be primarily inherited from the initial turbulence within the core itself.

As originally pointed out by *Burkert and Bodenheimer* (2000), the observed rotation-like features of a linear velocity gradient may arise from sampling of turbulence at a range of scales. Since, $J = L/M \sim R \cdot v_{\rm rot}$, the correlation $J \propto R^{1.5}$ simply suggests that $v_{\rm rot} \propto R^{0.5}$ (*Chen and Ostriker* 2018). Such a relation is similar to the so-called Larson relation of turbulent interstellar medium, that the turbulent velocities (traced by spectral linewidth along the line of sight) increase roughly with $\ell^{1/2}$ where ℓ is the size of the system. Taken together, these results thus suggest that the rotational velocity in cores is inherited from the overall turbulent cascade.

We note that it is possible that angular momentum at

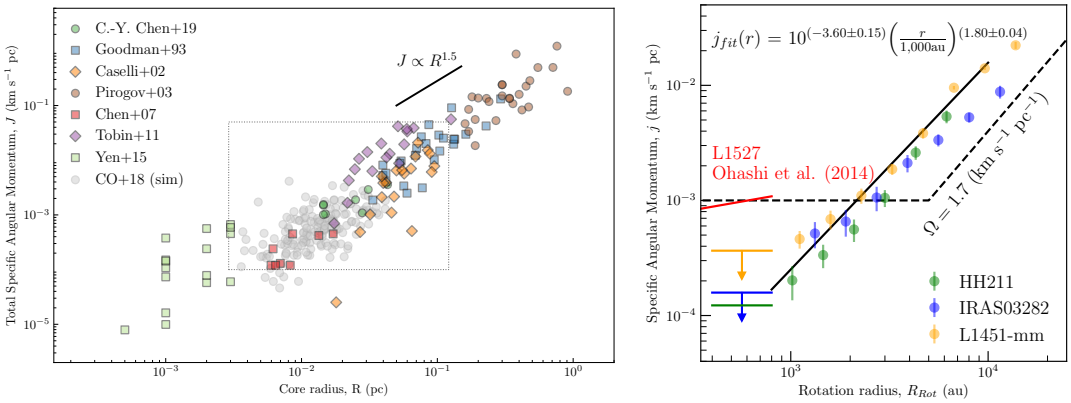

Fig. 13.— *Left:* The total specific angular momentum−size ($J - R$) correlation for a sample of dense cores (adapted from *Chen et al.* 2019a). The dashed box marks the region shown in the right panel. *Right:* Radial profile of the specific angular momentum, $j(r)$, for three YSOs (*Pineda et al.* 2019). Solid black line shows the best-fit power-law relation to the data between 800 and 10,000 au. The dash curve shows the previously proposed specific angular momentum profile (*Belloche* 2013).

core scale does not transport all the way to the disk-forming scale, and the rotation of the protostellar disk is independent of that in the core/envelope (see recent observations by *Chen et al.* 2019a). This would require a separate mechanism for disks to gain angular momenta, or the outward transport of angular momentum from the inner part by magnetic fields differs significantly between individual cores/envelopes. A highly-magnetized core with identical initial angular momentum likely forms a significantly smaller disk than a weakly-magnetized core (see e.g., *Li et al.* 2014b).

Gaudel et al. (2020) found difference of rotation direction of the outer core with respect to that of the inner core, which suggests that the rotation of the disk itself might not be inherited from the turbulence of the environment directly. *Verliat et al.* (2020) proposed a model that forms a disk without any initial rotation with respect to the geometric center of a prestellar core, or even without any turbulence. Since the angular momentum is defined with respect to a certain point, it can be easily generated during the core collapse as long as there exists some asymmetry in density or velocity that deviates the collapse from the original center of mass. The rotation thus generated is not related to the larger scale kinematics, but to density perturbations.

4.3.4. *Fragmentation*

One of the unknowns to understand the star formation process is the determination of how dense cores fragment during the star formation process (see Offner *et al.* in this volume). This is important since it can change the mapping between the CMF and the IMF (e.g. *Goodwin et al.* 2008), and it can also affect the properties of multiple systems (e.g. *Offner et al.* 2010; *Walch et al.* 2012). Several observations of samples of *starless* cores have attempted to determine the degree of fragmentation by carrying out relatively shallow dust continuum observations with interferometers (*Schnee et al.* 2010; *Dunham et al.* 2016; *Kirk et al.* 2017a; *Tokuda et al.* 2020; *Zhang et al.* 2021; *Sahu et al.* 2021), yielding a small number of continuum detections. Despite this low number of detections, these results are mostly compatible with the predictions (using synthetic observations) from numerical simulations of turbulent fragmentation (e.g., *Offner et al.* 2012; *Kirk et al.* 2017a).

The multi-scale fragmentation study by *Pokhrel et al.* (2018) indicates that the number of observed fragments is generally lower than expected from thermal Jeans fragmentation. This suggests that the mass scale of fragment formation is somewhat larger than the thermal Jeans mass, as is the case in magnetized clumps/cores with mildly supercritical mass-to-magnetic-flux ratios (*Das et al.* 2021).

ALMA observations of the L1521F protostellar core (*Tokuda et al.* 2014) revealed arc-like features and high-density substructures in different molecular transitions, suggesting dynamic gas interaction. Other efforts have focused on deeper observations of dense gas in the Barnard 5 region (*Pineda et al.* 2015; *Schmiedeke et al.* 2021; *Pineda et al.* 2021), which revealed the presence of fragmenting narrow filaments in the process of forming a wide separation quadruple system. The substructures found in this region are at scales much smaller than the Jeans scale, and therefore these observations reveal directly the turbulent fragmentation process within a core.

Recent deep ALMA observations of the prestellar core L1544 have revealed fragmentation in the inner 1500 au radius of a truly starless core (*Caselli et al.* 2019). These fragments (also called 'kernels') are detected at densities higher than 10^6 cm^{-3}, where the dense core density profile is smooth and flat. These observations are in agreement with non-ideal MHD simulations of a contracting dense core, for which the synthetic interferometric observations are a good match of the observations. This result highlights the need for deeper interferometric observations of additional presetellar cores to test fragmentation scenarios.

5. FROM CORES TO ACCRETING DISKS: IMPLICATION FROM KINEMATICS

The classical picture of star formation focuses on the material in an isolated parental dense core that undergoes gravitational collapse (*Larson* 1969; *Shu* 1977; *Terebey et al.* 1984). In addition, all the material used to form stars and planets must pass through the dense core. In this scenario, star- and disk-formation can be studied in numerical simulations of isolated/closed boxes, allowing the implementation of a range of physical processes (e.g., *Zhao et al.* 2018; *Machida and Basu* 2019; *Marchand et al.* 2020).

However, as discussed in the previous sections (e.g., Sect. 3.4), *Herschel* observations have consolidated the result that molecular clouds are highly sub-structured. While there are isolated cores (e.g., Bok globules), it is well established that most dense cores are harbored in filaments (see also *André et al.* 2014). As such, most cores do not form and will not evolve in isolation, and the interplay between dense cores and molecular clouds must be understood to improve our understanding of star and planet formation.

In this section we discuss how the dense core material is delivered to the disk forming scales. We present the observational and numerical evidence that disks cannot be considered as isolated entities detached from the dense gas at larger scales. The large scale environment is important to fully capture the disk- and star-formation process.

5.1. Non-axisymmetric Accretion onto Disks

The evidence for velocity coherent narrow structures funneling material, 'streamers', around young stellar objects (YSOs) at different evolutionary stages is growing. The kinematic structure of streamers combines a smooth velocity gradient (driven by gravity) and some amount of rotation. Therefore, modelling is required to truly confirm their nature. Here we present and discuss different examples of streamers at different evolutionary stages. We divide the discussion based on the observationally-defined Classes of YSOs (*Lada* 1987; *André et al.* 2000; *Dunham et al.* 2014), from deeply embedded, envelope-dominated protostars with high ratios of submillimeter to bolometric luminosity (Class 0), to more evolved protostars in which the circumstellar envelope no longer dominates and the central star+disk system is visible in the near-infrared (Class I), to pre-main sequence stars with protoplanetary disks and negligible circumstellar envelopes (Class II).

5.1.1. Highly Embedded Class 0 Protostars

Non-axisymmetric structures around Class 0 objects were observed with *Spitzer*, and they were interpreted as the result of the collapse of non-equilibrium structures (*Tobin et al.* 2010). Initial observations suggesting the presence of accretion streamers in young Class 0 objects (Serpens SMM1 and Serp-emb-8) were presented by *Le Gouellec et al.* (2019). These ALMA dust continuum polarization observations at 870 μm, with a resolution better than 150 au, revealed the presence of two magnetically-aligned filamentary features reaching down to the disk scales. The authors suggest that at least one of these features might indeed be related to accretion streamers. Unfortunately, there are no complementary molecular line observations that could confirm the nature of the accretion stream.

Recently, NOEMA observations of a Class 0 source in Perseus (Per-emb-2) revealed the presence of a large scale streamer (*Pineda et al.* 2020). These observations detected the streamer in molecular line emission, but not in the (less sensitive) dust continuum emission. The derived velocity map in the streamer is smooth and shows a streamer that begins at ≈10,000 au from the central YSO (beyond the classical dense core seen in NH_3 and N_2H^+). It displays a velocity gradient well matched by a model of free-falling material and rotation. Figure 14 shows the velocity derived using HC_3N, while the dense core traced with N_2H^+ is shown in contours. The estimated average infall rate from the streamer onto the disk forming scales is 10^{-6} $M_\odot$ yr^{-1}, which is comparable to the current protostellar accretion rate of 7×10^{-7} $M_\odot$ yr^{-1} (*Frimann et al.* 2017; *Hsieh et al.* 2019). This suggests that the streamer could modify protostellar accretion by funnelling extra material to the central region.

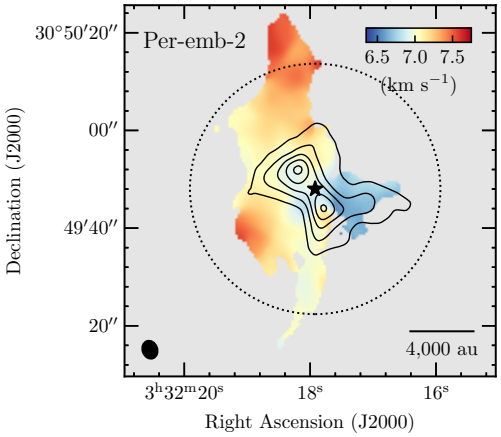

Fig. 14.— A large scale streamer and the dense core around Per-emb-2. The centroid velocity from HC_3N (10–9) is in the background, original data from *Pineda et al.* (2020). Dense core as traced in integrated intensity of N_2H^+ (1–0) are shown in contours. Beam size and scale bar are shown in bottom left and right corner, respectively.

A similar analysis was performed for Lupus 3-MMS (*Thieme et al.* 2022), which highlights the presence of multiple accretion streams seen in $C^{18}O$ with ALMA. A total of four different structures are well modelled with infall models (including rotation), with a total infall rate on the streamers of $0.5 - 1.1 \times 10^{-6}$ $M_\odot$ yr^{-1}. This is the first case of multiple streamers modeled in a single source.

Recently, observations of molecular line emission revealed more streamers toward B335 (*Cabedo et al.* 2021), Per-emb-8 (*Segura-Cox et al.*, in prep.) and IRAS16293A (*Murillo et al.* 2022). In particular, it is surprising that the

detection of the streamer in the well-studied IRAS16293A had remained unidentified, highlighting the relevance of re-evaluating previous observations in view of these new features.

5.1.2. *Class I YSOs*

The surprising observations of rings and gaps in the disk around HL Tau with ALMA (*ALMA Partnership et al.* 2015) suggested that planet formation might already be ongoing in these early stages. Therefore, several observations have focused on studying the disk properties and their relation with the surrounding envelope. ALMA observations of HL Tau revealed an accretion stream of ≈200 au in length (*Yen et al.* 2019), that brings material down to the disk-forming scales in an asymmetrical fashion. Figure 15 shows the extent of the gas disk kinematics and the streamer, as traced with HCO^+ (3–2), while the rings and gaps in the disk are marked by the contours. Using a parametric modelling of the kinematics, *Yen et al.* (2019) show that the gas kinematics of the streamer are a combination of infall and rotation. Recently, *Garufi et al.* (2022) also detected the streamer in CS (5–4) with ALMA, which when combined with HCO^+ allows for a good fit of the emission using a streamline model as in the Class 0 case (*Pineda et al.* 2020). Moreover, *Garufi et al.* (2022) presents evidence for shocks, which are usually traced in SO and SO_2 in disks (*Sakai et al.* 2014), that would mark the interaction region between disk and streamer. This example shows that the streamer delivers material to the disk, which is then transported through the disk without perturbing the dust structures in the midplane.

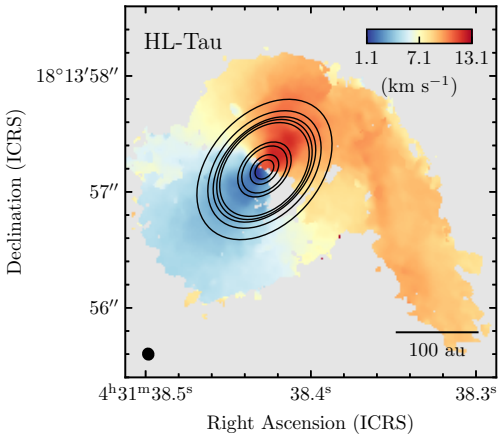

Fig. 15.— The streamer and disk around HL Tau. The centroid velocity from HCO^+ (3–2) is in the background, original data from *Yen et al.* (2019). Dust continuum rings and gaps in the disk, as identified in *ALMA Partnership et al.* (2015), are shown in contours. Beam size and scale bar are shown in bottom left and right corner, respectively.

In a similar way, the youngest Class I disk with rings (IRS 63; *Segura-Cox et al.* 2020) also presents a clear streamer detected in HCO^+ (*Segura-Cox et al.* 2022). This streamer is also well described with a streamline model, and the derived streamer infall rate is comparable with the accretion rate. This is a second example of rings identified in dust emission, which are unperturbed by the streamer infall, and with clear evidence of shocks thanks to the detection of bright SO emission where streamer and disk meet. Further analysis of the gas disk could shed some more light on how the streamer would modify the gas disk.

Finally, NOEMA observations revealed the presence of a streamer in H_2CO and $C^{18}O$ toward the Class I object Per-emb-50 (*Valdivia-Mena et al.* 2022). This streamer has an extent >2,000 au and is well described with a streamline model, confirming that this material is infalling to the central disk scales. The derived streamer infall rate is comparable to the accretion rate derived from NIR spectroscopy (*Fiorellino et al.* 2021), which once again points to the relevant role of streamers in the accretion process of young stars. Also, *Valdivia-Mena et al.* (2022) quantify the infall rate along the streamer, showing that the variations are within a factor of ≈ 3 from the average value and systematically above the current protostellar accretion rate.

5.1.3. *Class II Objects*

Recently, streamers have been identified toward Class II objects. Despite the low level of envelope surrounding them, sensitive ALMA observations have revealed the presence of gas streamers. In the case of SU Aur, a long tail (≈3000 au at a distance of 158 pc) is detected in CO (2–1) with ALMA (*Akiyama et al.* 2019) with a coherent centroid velocity map. This suggests that the structure is associated with a single infall event, although the original discovery paper suggested that a collision with a (sub)stellar intruder or a gaseous blob was probably the most plausible explanation. Complementary SPHERE observations of SU Aur ruled out a recent close encounter or the ejection of a dust clump for their origin (*Ginski et al.* 2021), suggesting that material is falling onto the central system (see Fig. 16). Moreover, these observations revealed that more than one streamer is approaching the disk. This source represents one of the clearest examples of late accretion onto a disk. Apart from SU Aur, there are at least two other stars in the L1517 cloud that show similar patterns of external streamers: AB Aur (*Grady et al.* 1999) and GM Aur (*Huang et al.* 2021).

Similarly, new ALMA observations of DG Tau revealed the presence of two streamers reaching the disk (*Garufi et al.* 2022), and one of these streamers was previously identified as an accretion flow in an outflow/wind study (*Güdel et al.* 2018). The streamers are detected in the CO (2–1) and CS (5–4) molecular lines and extend from ≈300 au in projected distance down to the disk edge. The molecular line observations allow for a determination of a smooth velocity gradient in the streamers, which are well modelled with streamlines. The presence of these streamers shows the emission landing on the disk, and the landing spot on the disk is identified with typical shock tracers (SO and SO_2). This again supports the idea that streamers can deliver ma-

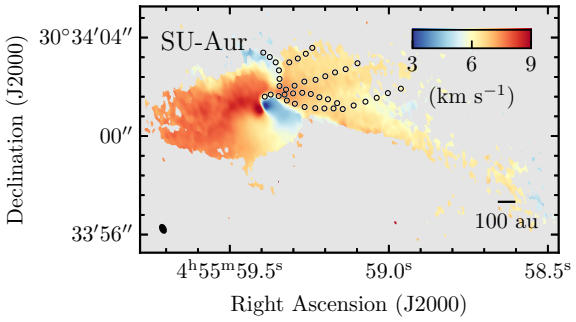

Fig. 16.— Several streamers toward SU Aur identified in CO and scattered light images. The centroid velocity from CO (3–2) is in the background, reprocessed data from *Ginski et al.* (2021); *Akiyama et al.* (2019). The disk rotation is clearly seen in the central region, while several streamers are seen, both kinematically and in scattered light images. The circles show the streamers identified in the SPHERE scattered light images (*Ginski et al.* 2021). The long streamer extending south-west matches very well the streamer previously seen in HST Coronagraphic observations (*Grady et al.* 2001).

terial down to the disk itself.

High resolution ALMA observations of [BHB2007] 1 (*Alves et al.* 2020) show a nearly edge-on gapped disk in dust continuum emission. The complementary molecular line observations revealed two streamers identified in the CO (2–1) transition from ≈2,000 au down to the disk edge. A follow-up analysis of VLA and NACO observations confirmed the presence of a substellar object (*Zurlo et al.* 2021). This presents further evidence that the presence of a streamer does not hinder the formation of companions.

5.2. Numerical Simulations

Considering that streamers have been observed for YSOs of Class 0, I, and II, it raises the question whether all streamers emerge through the same mechanism or whether there are differences depending on the evolutionary stage of the objects. As there is little information about the origin of streamers available yet, one of the key questions is whether streamers actually correspond to streams of gas or whether their origin is of a different kind. In this subsection, we provide an overview of currently suggested mechanisms that can explain the presence of such streamers.

5.2.1. Accretion Channels from Core to Disk

Numerical simulations of Bonnor-Ebert spheres using smoothed particle hydrodynamics (SPH) showed that the perturbations generated by the turbulence velocity would end up in irregular streams feeding the central disk (*Walch et al.* 2010). Similarly, numerical simulations including turbulence and magnetic fields (*Seifried et al.* 2013, 2015) showed that turbulence causes accretion onto the disk along distinct channels during the deeply embedded stage, in contrast to the previous picture that considered a coherent rotational structure during the collapse phase. Several MHD simulations from different groups also confirm the presence of channeled accretion along magnetized accretion streamers (e.g., *Joos et al.* 2013; *Li et al.* 2014a; *Masson et al.* 2016; *Kuffmeier et al.* 2017; *Matsumoto et al.* 2017; *Zhao et al.* 2018; *Lam et al.* 2019; *Hennebelle et al.* 2020). While different types of streamers have been seen in models already in the past ∼ ten years (Fig. 17), relatively little work has been done in analyzing the properties and effects of accretion streamers. Carrying out parameter studies using isolated core collapse models, the focus has been more on studying how effects such as (non-)ideal MHD (e.g., *Tomida et al.* 2015; *Masson et al.* 2016; *Wurster et al.* 2016) including the effect of the ionization degree (*Wurster et al.* 2018; *Kuffmeier et al.* 2020a), turbulence (e.g *Seifried et al.* 2012; *Joos et al.* 2013; *Gray et al.* 2018; *Wurster and Lewis* 2020), orientation of the magnetic field with respect to the total angular momentum vector (e.g., *Joos et al.* 2012; *Krumholz et al.* 2013; *Tsukamoto et al.* 2018; *Hirano et al.* 2020), or the grain size distribution (*Zhao et al.* 2016; *Marchand et al.* 2020) affect the size of circumstellar disks. Therefore, modelers and theorists have not paid much attention to streamers as they presumably violate the picture of symmetrical collapse and as they are difficult to approximate in simpler 2D or 1D models.

Core collapse models that start with an initially perturbed velocity distribution of the gas in the spherical core frequently show the presence of accretion streamers that feed the young disk with fresh material from the dense core (e.g., *Walch et al.* 2010; *Seifried et al.* 2013; *Seifried and Walch* 2015; *Joos et al.* 2013; *Hennebelle et al.* 2020; *Zhao et al.* 2018). Carrying out a parameter study including different levels of initial turbulence, *Mignon-Risse et al.* (2021) found that the streamers were wider for higher levels of initial turbulence, possibly caused by turbulent reconnection (e.g., *Lazarian and Vishniac* 1999; *Santos-Lima et al.* 2013).

5.2.2. Streamers from Interstellar Scales to Protostellar Scales

While collapse models have become increasingly sophisticated in terms of including more physics in the simulations, they have fundamental limitations in their setups as highly idealized initial and boundary conditions remain. Since stars form inside the large-scale environment defined by MCs, and because some streamers are seen reaching out beyond the dense core (*Pineda et al.* 2020), a more realistic framework for star formation would include the larger-scale environments of the MC in which stars are embedded.

Although several specifically designed parameter studies investigated infall onto an existing disk (*Vorobyov et al.* 2015; *Bae et al.* 2015; *Lesur et al.* 2015; *Lee et al.* 2021; *Kuznetsova et al.* 2022), only a few groups studied disk formation while covering the dynamical range from (giant) MC scales down to the disk in one self-consistent model. *Bate* (2018) and *Lebreuilly et al.* (2021) independently carried out population synthesis studies of the formation of in-

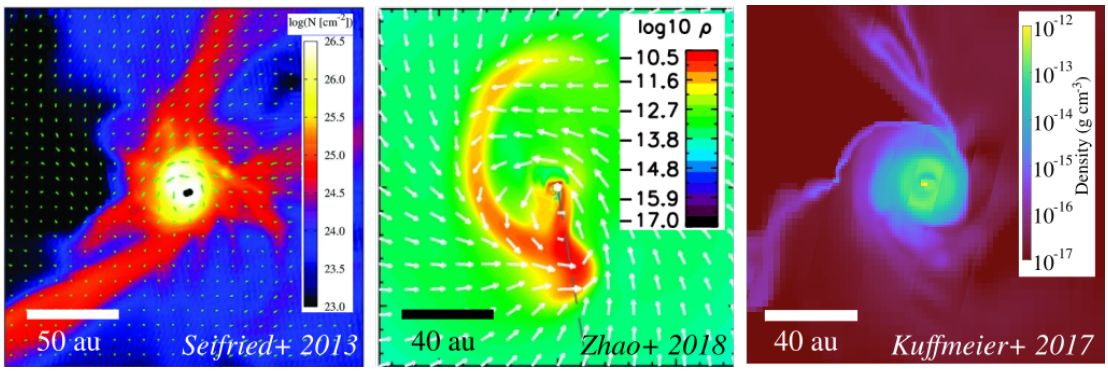

Fig. 17.— Streamers around disks in different MHD simulations. These simulations include different setups, but similar streamers emerge as a result of asymmetric infall. The left panel shows results from simulations first presented in *Seifried et al.* (2013), the middle results presented in *Zhao et al.* (2018), and the right panel results first presented in *Kuffmeier et al.* (2017).

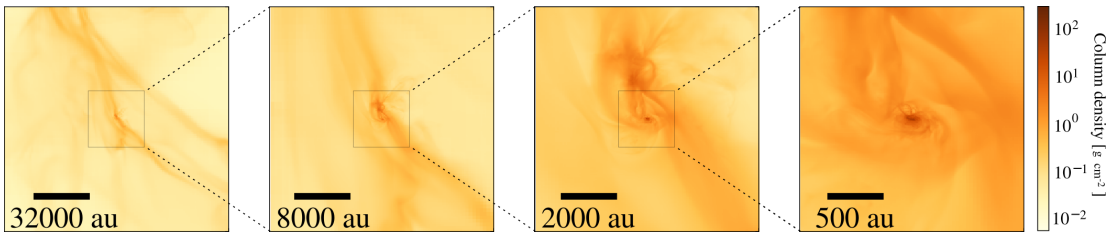

Fig. 18.— Zoom-in onto a forming protostar that is embedded in a turbulent birth environment of a MC. It shows the presence of a bridge connecting the central protostar with the parental molecular cloud. The snapshot is taken from multi-scale MHD models by *Kuffmeier et al.* (2019).

dividual disks in stellar clusters that emerged from the collapse of a massive clump of 100–1000 $M_\odot$ in mass and about 0.1 to 1 pc in length. *Bate* (2018) carried out SPH models without magnetic fields, *Lebreuilly et al.* (2021) models with non-ideal MHD using adaptive mesh refinement (AMR). While these models show the presence of accretion streamers and provide first statistical constraints on disk formation, they cannot take into account the dynamics on MC scales that are responsible for inflow (see Sect. 3.1).

To cover the range of scales from the MC down to the disk (see Fig. 19 and *Padoan et al.* 2020; *Pelkonen et al.* 2021, see also sections 3.1 or 4.2.2), *Kuffmeier et al.* (2016) started a sequence of papers started their models from a MC of $\sim 10^5$ $M_\odot$ in mass and (40 pc)^3 in volume and analyzed the star-disk formation process in 3D MHD zoom-in simulations with a resolution down to 0.06 au (*Kuffmeier et al.* 2018), which marks the largest spatial coverage so far (see Fig. 18 for a zoom-in onto a deeply embedded protostar forming in a filament; *Kuffmeier et al.* 2019). Their models (*Kuffmeier et al.* 2017) confirm that accretion within the core scale happens via accretion channels (*Seifried et al.* 2013). They also predicted the possibility of replenishing the disk (and thereby the mass reservoir for planet formation) with material that was originally not gravitationally bound to the collapsing core (as observed for Per-emb-2 *Pineda et al.* 2020). Regardless of the (significant) differences in the physics and spatial coverage of these models (*Kuffmeier et al.* 2017; *Bate* 2018; *Lebreuilly et al.* 2021), they agree on the key result that disk formation is a heterogeneous, environmentally dependent process.

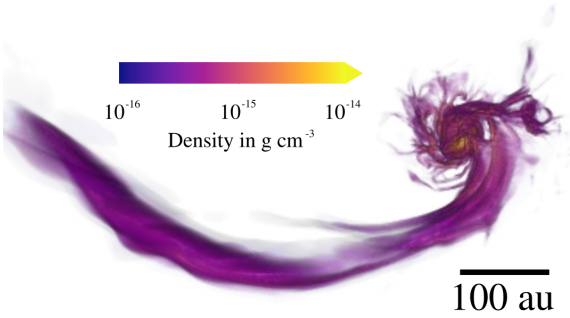

Fig. 19.— A streamer feeding an embedded disk (visualization made by using data from *Kuffmeier et al.* 2019).

5.2.3. *Late Interaction with the Protostellar Environment*

Stellar encounters can lead to the formation of spiral- or tail-like structures that may resemble the aforementioned accretion streamers. It is important to highlight that there are other mechanisms that can cause the formation of streamer-like structures.

Gas Capture

Filamentary arms around YSOs might arise after the initial collapse phase if the star experiences an encounter

with interstellar gas (*Bate* 2018). The scenario was tested more in parameter studies adopting a setup of cloudlet-infall/capture with the codes PLUTO (*Dullemond et al.* 2019) and AREPO (*Kuffmeier et al.* 2020b, 2021). Sweeping up gas via Bondi-Hoyle accretion can lead to the formation of filamentary arms that can appear as accretion streamers. Interestingly, a (late) encounter can even induce the formation of a new, second-generation disk (*Kuffmeier et al.* 2020b) that is likely misaligned with the primordial disk from the initial protostellar collapse (*Bate* 2018; *Kuffmeier et al.* 2021). Infall may therefore not only rejuvenate primordial disks, but also induce new misaligned disks that can explain shadows in scattered light observations of some systems (e.g., *Avenhaus et al.* 2014; *Marino et al.* 2015; *Benisty et al.* 2017, 2018; *Casassus et al.* 2018; *Ginski et al.* 2021).

Stellar Fly-By

We point out that a spiral or tail-like structure around a disk may not necessarily be associated with infall. It can also be a consequence of the interaction of a star-disk system with an external perturber, such as a binary component or a stellar fly-by. The possibility of an external star that perturbs the disk has been studied and discussed already for a few decades (e.g., *Clarke and Pringle* 1993; *Pfalzner* 2003). Recent hydrodynamical models show that a star that encounters an existing star-disk system triggers a spiral structure (*Vorobyov et al.* 2017; *Cuello et al.* 2020). When such a structure is observed from the 'right' angle, it resembles the aforementioned accretion streamers proposed for Z CMa (*Dong et al.* 2022). Apart from that, perturbations by stellar companions in the disk might be responsible for tearing up the disk, and hence induce misalignment of inner and outer disks (e.g., *Nealon et al.* 2020b) similar to disk tearing in accretion disks around black holes (e.g., *Nixon et al.* 2012). However, it is difficult for an external perturber alone to tear up protostellar/-planetary disks because of the low viscosity in these disks (*Gonzalez et al.* 2020; *Nealon et al.* 2020a; *Smallwood et al.* 2021). An external large-scale streamer around a misaligned outer disk might therefore hint at second-generation disk formation (see also Sect. 4.3 on misalignment in *Pinte et al.* 2022).

6. CONCLUSIONS AND FUTURE CHALLENGES

Here, we summarize the coherent picture of the overall star formation process arising from the current observations and models. Thanks to a new array of observations, we are now able to better connect the anisotropic flow of material through different levels of structures in the hierarchical ISM. In particular, the high spatial dynamic range of submillimeter dust continuum images from *Herschel* and *Planck* has been essential to connecting column density structures observed across a wide range of scales from giant HI and HII bubbles to filaments and protostellar cores. Large molecular line surveys have been crucial in providing kinematic tests of filament formation and accretion models (see Sects. 2 and 3), and tracing gas motions and angular momentum from cloud to core and disk scales (see Sects. 4 and 5). In parallel, analytic models and numerical simulations provide detailed predictions that can be tested directly against observational results. Over this wide range of scales, bubbles, filaments, cores, and disks appear to be fundamental, interconnected levels of ISM structures, differing in their 3D geometry and dominated by different physics (see sketch in Fig. 20). Specifically, compressive turbulent flows driven by the quasi-spherical expansion of large bubbles dominate on $\sim$1–100 pc scales, generating shock-compressed layers of magnetized molecular gas. Dense, self-gravitating filaments form within these shock-compressed layers on $\sim$pc scales as a result of the combined action of magnetic fields and large-scale flows. The gravo-turbulent fragmentation of self-gravitating filaments leads to the formation of rotating prestellar cores on $\lesssim$ 0.1 pc scales. Eventually, the gravitational collapse of rotating, non-axisymmetric dense cores produces protostellar systems with ringed disks and infalling streamers on $\lesssim$ 1000 au scales.

In contrast to other scenarios, our proposed picture (cf. Fig. 20) emphasizes the role of geometrical effects at different scales in the process. It also provides new clues toward understanding the origin of 1) the core/star formation inefficiency, 2) the stellar initial mass function (IMF), and 3) the angular momentum of protostellar systems.

Observations suggest a connection between the expanding bubbles in the ISM (in HII and HI) and the formation of dense filamentary structures, though detailed numerical investigations are needed to provide more direct comparisons to the observed bubble-filament connection. Additional observational and theoretical studies are also required to understand the possible evolutionary link between atomic and molecular filaments and the role of HII regions (i.e., formation and/or feedback) on the surrounding filamentary ISM.

While multiple mechanisms for filament formation have been presented, the current data are consistent with filaments being formed from converging flows within magnetized shock-compressed layers (type-O/C mechanisms in Fig. 4) with further mass growth due to gravity. The critical feature of filament formation is thus one of compressive flows. Several scenarios have been invoked to explain the origin of velocity-coherent fibers within filaments. These fibers are commonly, but not universally, observed, and observational tests are needed that can distinguish between, e.g., fragment-and-gather and fray-and-fragment models.

The filament line mass function (FLMF – Fig. 11a) appears as an important property of the population of molecular filaments. The critical line mass for nearly isothermal filaments sets a natural transition for the core formation efficiency within filamentary molecular clouds, between a regime with negligible formation of prestellar cores at low densities in subcritical filaments and a regime with relatively efficient core formation at high densities in thermally supercritical filaments (Fig. 9). The shape of the prestellar core mass function, and by extension that of the stellar

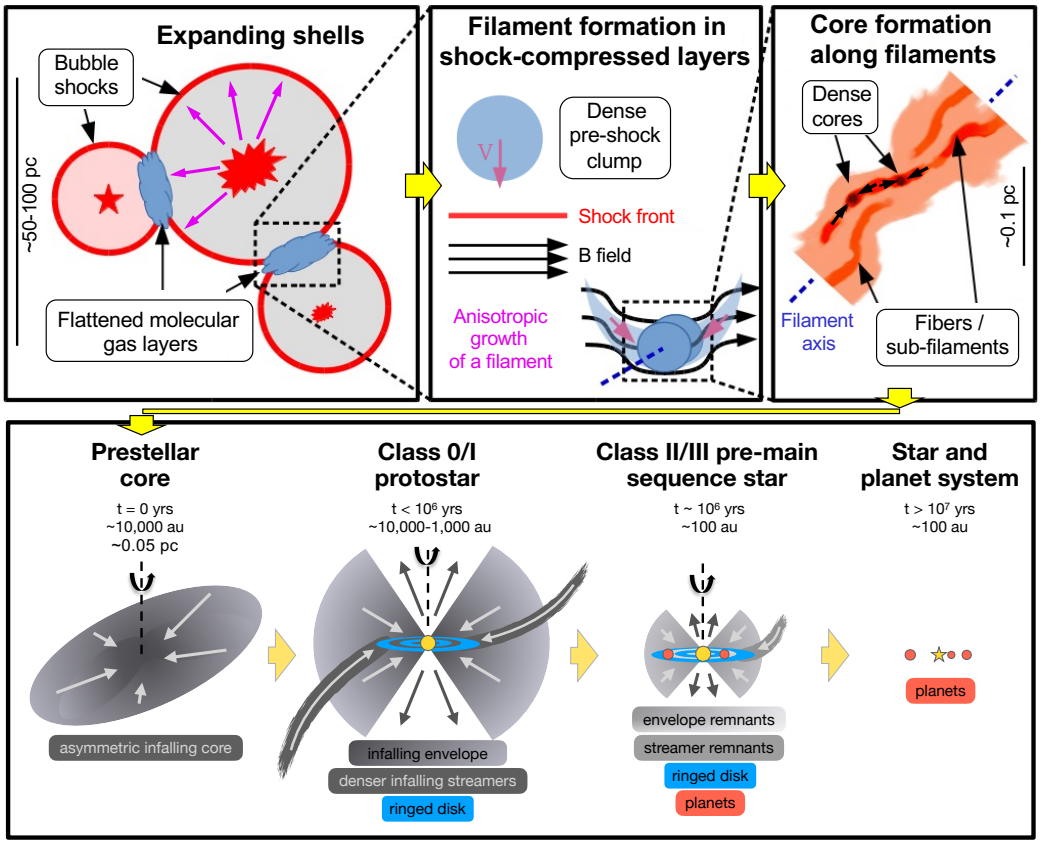

Fig. 20.— Sketch of the star-formation process on various scales, emphasizing the anisotropic growth of dense structures in the cold ISM leading to the formation of stars and planetary systems. It highlights the role of large-scale expanding bubbles in compressing interstellar matter in flattened gas layers and producing molecular filaments, which themselves form rotating dense cores through axial gravo-turbulent fragmentation (top row, see Sects. 2 and 3). The sketch also emphasizes the role of angular momentum and non-axisymmetric streamers at core/disk scales (bottom row adapted from *Segura-Cox et al.*, in prep.); the classical dense core and these streamers coexist at different evolutionary stages of protoplanetary disk formation (see Sects. 4 and 5). The orientation of the streamers is not necessarily aligned with the rotation axis of the dense core, but it does follow a trajectory consistent with free-fall and rotation.

IMF, may be partly inherited from the FLMF (see Sect. 3.6). Observed core spacings do not generally follow the simple periodic predictions of gravitational fragmentation models within near-equilibrium cylindrical filaments. Filamentary fragmentation likely unfolds over multiple scales where either gravitational fragmentation of supercritical filaments, or gravity-induced turbulence dominate.

Prestellar cores are primarily found within thermally transcritical or supercritical filaments. One of the key properties of cores is the amount of rotation present, which is directly related to the origin of the angular momentum. The total angular momentum seen in cores is consistent with being dominated by the turbulent motions injected at the largest scales and may be partly inherited from the formation and fragmentation process of the parent filaments (e.g. Sect 4.3.3 and Fig. 13). While resolved observations of cores revealed clear differential rotation, the scale on which specific angular momentum is constant (and gravity dominates) is just being resolved at smaller radii than previously suggested (<1,000 au). Therefore, magnetic braking must be quite important to explain the small disk radii observed around Class 0 objects.

With the spatial resolution in nearby regions made possible with interferometers, we can now measure infall and rotation within cores and follow the gas from core to disk. Observations on these scales have revealed a new component: streamers. The detection of streamers has modified our view of the mass delivery at core/disk scales. The sketch at the bottom of Fig. 20 starts with a prestellar core, which has begun gravitational collapse. The next stage shows the classical picture of the dense core feeding the disk and with the addition of possible multiple streamers. Later on, once most of the surrounding envelope is gone, some late accretion events would be driven by streamers. Since streamers deliver material non-axisymmetrically to disks, they may be in part responsible for luminous outbursts, and help solve the YSO luminosity problem. Streamers could play an important role in the formation and evolution of disks, since in addition to the sudden mass delivery at small scales, these streamers likely bring a different amount (or orientation) of angular momentum to the disk-forming scales, which has a direct relation to the maximum disk size. Stream-

ers might bring grains which have not undergone as much grain-growth as in the classical inner envelope, changing the fraction of small grains at disk scales, which also has a direct role in the disk formation process. Similarly, streamers are particularly abundant in chemically fresh (carbon rich) species in the gas phase, which would directly affect the chemistry and gas phase composition of material available during planet formation.

Future Challenges: Determining the role of magnetic fields in the formation and evolution of filaments remains one of the main challenges for future observations and models. Further insight will be achieved thanks to ongoing and planned polarization surveys at far-infrared and submillimeter wavelengths with SOFIA-HAWC+, SCUBA2-POL2, and NIKA2-POL, and in the future with a space-based high-dynamic-range polarimeter such as Millimetron or the Origins Space Telescope. Combined with gas kinematics surveys on the same spatial scales, the new polarization data will provide critical tests of the models of filament formation within magnetized shock-compressed layers.

Systematic dust polarization studies at sub-arcmin resolution will determine whether magnetic fields remain perpendicular to the long axis of star-forming filaments or typically switch to a parallel configuration in their dense $\sim$0.1 pc interior. This will have profound implications for our understanding of filament stability and fragmentation into prestellar cores. The scales involved in filament fragmentation are difficult to assess statistically given the small numbers of cores found in any individual filament. The importance of gravo-turbulence in filament evolution and fragmentation is highlighted by dynamic models with and without B-fields, and future observational analyses with millimeter and submillimeter interferometers such as ALMA and NOEMA will continue to test these models.

Characterizing critical stages in protostellar evolution, such as the break in the specific angular momentum profile of individual protostellar cores (e.g., Fig. 13b), is a crucial challenge for future interferometric studies of gas kinematics at core scale. Given the complexity in chemistry, evolutionary stages, and kinematics, the interpretation of these observations will critically depend on the comparison with synthetic line observations from simulated dense cores.

Current observational evidence and theoretical models indicate that streamers are dominated by free-falling motions, however, it is still unknown how often and for how long streamers affect the disk scales. Moreover, there is a strong need for further observations to better quantify the roles of streamers, while also determining if there are environmental factors. In addition, since there are many different paths in which numerical simulations are able to generate streamer-looking features and non-axisymmetric accretion flows, it is crucial to post-process different numerical simulations to establish which of the possible scenarios for their origin provides a better match to the observations. One of the biggest challenges for modelers in the upcoming years will be to provide better constraints on the kinematics of streamers. Multi-scale, multi-physics simulations covering a large physical range should provide important constraints on the origin of chemical differences between streamers and dense cores, and help to diagnose observable tracers of streamers via synthetic observations.

Acknowledgments JEP acknowledges the support by the Max Planck Society. AZ acknowledges the support of the Institut Universitaire de France (IUF). PhA acknowledges support from "Ile de France" regional funding (DIM-ACAV+) and from the French national programs on stellar and ISM physics (PNPS and PCMI). SDC is supported by the Ministry of Science and Technology (MoST) in Taiwan through grant MoST 108-2112-M-001-004-MY2. YNL acknowledges funding from the Ministry of Science and Technology, Taiwan (109-2636-M-003-001 and 110-2124-M-002-012), the grant for Yushan Young Scholar from the Ministry of Education, Taiwan. JDS acknowledges funding from the European Research Council under the Horizon 2020 Framework Program via the ERC Consolidator Grant CSF-648505. MK acknowledges funding from the European Union's Framework Programme for Research and Innovation Horizon 2020 (2014-2020) under the Marie Skłodowska-Curie Grant Agreement No. 897524. This work was performed under the auspices of the U.S. Department of Energy (DOE) by Lawrence Livermore National Laboratory under Contract DE-AC52-07NA27344 (C.-Y.C).

REFERENCES

Abe D. et al., 2021 *ApJ*, *916*, 2, 83.
Akiyama E. et al., 2019 *AJ*, *157*, 4, 165.
ALMA Partnership et al., 2015 *ApJL*, *808*, 1, L3.
Alves F. O. et al., 2020 *ApJL*, *904*, 1, L6.
Alves J. et al., 2007 *A&A*, *462*, 1, L17.
Alves de Oliveira C. et al., 2014 *A&A*, *568*, A98.
André P. et al., 2000 *Protostars and Planets IV* (V. Mannings, A. P. Boss, and S. S. Russell), p. 59.
André P. et al., 2010 *A&A*, *518*, L102.
André P. et al., 2014 *Protostars and Planets VI* (H. Beuther, R. S. Klessen, C. P. Dullemond, and T. Henning), p. 27.
André P. et al., 2016 *A&A*, *592*, A54.
André P. et al., 2019 *A&A*, *629*, L4.
Areal M. B. et al., 2019 *PASA*, *36*, e049.
Arzoumanian D. et al., 2011 *A&A*, *529*, L6.
Arzoumanian D. et al., 2013 *A&A*, *553*, A119.
Arzoumanian D. et al., 2018 *PASJ*, *70*, 5, 96.
Arzoumanian D. et al., 2019 *A&A*, *621*, A42.
Arzoumanian D. et al., 2021 *A&A*, *647*, A78.
Arzoumanian D. et al., 2022 *arXiv e-prints*, arXiv:2201.04267.
Auddy S. et al., 2016 *ApJ*, *831*, 1, 46.
Avenhaus H. et al., 2014 *ApJ*, *781*, 87.
Bae J. et al., 2015 *ApJ*, *805*, 1, 15.
Ballesteros-Paredes J. and Mac Low M.-M., 2002 *ApJ*, *570*, 2, 734.
Ballesteros-Paredes J. et al., 2015 *MNRAS*, *452*, 1, 566.
Barnes A. T. et al., 2018a *MNRAS*, *475*, 4, 5268.
Barnes P. J. et al., 2018b *ApJ*, *866*, 1, 19.

Bastien P., 1983 *A&A*, *119*, 1, 109.
Bate M. R., 2018 *MNRAS*, *475*, 4, 5618.
Bate M. R., 2019 *MNRAS*, *484*, 2, 2341.
Baug T. et al., 2018 *ApJ*, *852*, 2, 119.
Beaumont C. N. et al., 2013 *ApJ*, *777*, 2, 173.
Belloche A., 2013 *EAS Publications Series*, vol. 62 of *EAS Publications Series* (P. Hennebelle and C. Charbonnel), pp. 25–66.
Belloche A. et al., 2002 *A&A*, *393*, 927.
Benedettini M. et al., 2018 *A&A*, *619*, A52.
Benisty M. et al., 2017 *A&A*, *597*, A42.
Benisty M. et al., 2018 *A&A*, *619*, A171.
Berry D. S., 2015 *Astronomy and Computing*, *10*, 22.
Bertelli Motta C. et al., 2016 *MNRAS*, *462*, 4, 4171.
Bertoldi F. and McKee C. F., 1992 *ApJ*, *395*, 140.
Beuther H. et al., 2007 *Protostars and Planets V* (B. Reipurth, D. Jewitt, and K. Keil), p. 165.
Beuther H. et al., 2015a *A&A*, *584*, A67.
Beuther H. et al., 2015b *A&A*, *581*, A119.
Bhadari N. K. et al., 2020 *ApJ*, *899*, 2, 167.
Bleuler A. and Teyssier R., 2014 *MNRAS*, *445*, 4, 4015.
Blitz L., 1993 *Protostars and Planets III* (E. Levy and J. Lunine), pp. 125–161.
Bohlin R. C. et al., 1978 *ApJ*, *224*, 132.
Bonne L. et al., 2020 *A&A*, *644*, A27.
Bracco A. et al., 2020a *A&A*, *644*, A5.
Bracco A. et al., 2020b *A&A*, *644*, L3.
Bresnahan D. et al., 2018 *A&A*, *615*, A125.
Brown A. G. A. et al., 1995 *A&A*, *300*, 903.
Burkert A. and Bodenheimer P., 2000 *ApJ*, *543*, 2, 822.
Burkhart B. et al., 2013 *ApJ*, *770*, 2, 141.
Cabedo V. et al., 2021 *A&A*, *653*, A166.
Campbell J. L. et al., 2016 *ApJ*, *819*, 2, 143.
Casassus S. et al., 2018 *MNRAS*, *477*, 4, 5104.
Caselli P. et al., 2002 *ApJ*, *572*, 1, 238.
Caselli P. et al., 2019 *ApJ*, *874*, 1, 89.
Chen C.-Y. and Ostriker E. C., 2014 *ApJ*, *785*, 1, 69.
Chen C.-Y. and Ostriker E. C., 2015 *ApJ*, *810*, 2, 126.
Chen C.-Y. and Ostriker E. C., 2018 *ApJ*, *865*, 1, 34.
Chen C.-Y. et al., 2017 *ApJ*, *847*, 2, 140.
Chen C.-Y. et al., 2019a *MNRAS*, *490*, 1, 527.
Chen C.-Y. et al., 2020a *MNRAS*, *494*, 3, 3675.
Chen H. H.-H. et al., 2019b *ApJ*, *877*, 2, 93.
Chen H. H.-H. et al., 2020b *arXiv e-prints*, arXiv:2006.07325.
Chen M. C.-Y. et al., 2016 *ApJ*, *826*, 1, 95.
Chen M. C.-Y. et al., 2020c *ApJ*, *891*, 1, 84.
Chen X. et al., 2007 *ApJ*, *669*, 2, 1058.
Chira R. A. et al., 2018 *A&A*, *610*, A62.
Choudhury S. et al., 2020 *A&A*, *640*, L6.
Choudhury S. et al., 2021 *A&A*, *648*, A114.
Chung E. J. et al., 2019 *ApJ*, *877*, 2, 114.
Chung E. J. et al., 2021 *ApJ*, *919*, 1, 3.
Clark S. E. and Hensley B. S., 2019 *ApJ*, *887*, 2, 136.
Clark S. E. et al., 2014 *ApJ*, *789*, 1, 82.
Clarke C. J. and Pringle J. E., 1993 *MNRAS*, *261*, 1, 190.
Clarke S. D. and Whitworth A. P., 2015 *MNRAS*, *449*, 2, 1819.
Clarke S. D. et al., 2016 *MNRAS*, *458*, 1, 319.
Clarke S. D. et al., 2017 *MNRAS*, *468*, 2, 2489.
Clarke S. D. et al., 2018 *MNRAS*, *479*, 2, 1722.
Clarke S. D. et al., 2019 *MNRAS*, *484*, 3, 4024.
Clarke S. D. et al., 2020 *MNRAS*, *497*, 4, 4390.
Colman T. and Teyssier R., 2020 *MNRAS*, *492*, 4, 4727.
Corsaro E. et al., 2017 *Nature Astronomy*, *1*, 0064.
Cox N. L. J. et al., 2016 *A&A*, *590*, A110.
Csengeri T. et al., 2017 *A&A*, *600*, L10.
Cuello N. et al., 2020 *MNRAS*, *491*, 1, 504.
Daigle A. et al., 2007 *ApJ*, *661*, 1, 285.
Dall'Olio D. et al., 2019 *A&A*, *626*, A36.
Das I. et al., 2021 *A&A*, *649*, L13.
Dawson J. R. et al., 2008 *MNRAS*, *387*, 1, 31.
Deharveng L. et al., 2015 *A&A*, *582*, A1.
Dewangan L. K., 2021 *MNRAS*, *504*, 1, 1152.
Dewangan L. K. et al., 2019 *ApJ*, *877*, 1, 1.
Dhabal A. et al., 2018 *ApJ*, *853*, 2, 169.
Dhabal A. et al., 2019 *ApJ*, *876*, 2, 108.
Di Francesco J. et al., 2001 *ApJ*, *562*, 2, 770.
di Francesco J. et al., 2007 *Protostars and Planets V* (B. Reipurth, D. Jewitt, and K. Keil), p. 17.
Di Francesco J. et al., 2020 *ApJ*, *904*, 2, 172.
Dib S. et al., 2007 *ApJ*, *661*, 1, 262.
Doi Y. et al., 2020 *ApJ*, *899*, 1, 28.
Dong R. et al., 2022 *Nature Astronomy*, *6*, 331.
Drabek-Maunder E. et al., 2016 *MNRAS*, *457*, 1, L84.
Duarte-Cabral A. et al., 2012 *A&A*, *543*, A140.
Dullemond C. P. et al., 2019 *A&A*, *628*, A20.
Dunham M. M. et al., 2014 *Protostars and Planets VI* (H. Beuther, R. S. Klessen, C. P. Dullemond, and T. Henning), p. 195.
Dunham M. M. et al., 2016 *ApJ*, *823*, 2, 160.
Ehlerová S. and Palouš J., 2013 *A&A*, *550*, A23.
Ehlerová S. and Palouš J., 2016 *A&A*, *587*, A5.
Eisenstein D. J. and Hut P., 1998 *ApJ*, *498*, 1, 137.
Elia D. et al., 2021 *MNRAS*, *504*, 2, 2742.
Ellsworth-Bowers T. P. et al., 2015 *ApJ*, *805*, 2, 157.
Evans N. J. I. et al., 2015 *ApJ*, *814*, 1, 22.
Federrath C., 2016 *MNRAS*, *457*, 1, 375.
Fernández-López M. et al., 2014 *ApJL*, *790*, 2, L19.
Fiege J. D. and Pudritz R. E., 2000a *MNRAS*, *311*, 1, 85.
Fiege J. D. and Pudritz R. E., 2000b *MNRAS*, *311*, 1, 105.
Fiege J. D. and Pudritz R. E., 2000c *ApJ*, *544*, 830.
Fiorellino E. et al., 2021 *A&A*, *650*, A43.
Fischera J. and Martin P. G., 2012 *A&A*, *542*, A77.
Friesen R. K. et al., 2009 *ApJ*, *697*, 2, 1457.
Friesen R. K. et al., 2013 *MNRAS*, *436*, 2, 1513.
Friesen R. K. et al., 2016 *ApJ*, *833*, 2, 204.
Friesen R. K. et al., 2017 *ApJ*, *843*, 1, 63.
Frimann S. et al., 2017 *A&A*, *602*, A120.
Fukui Y. et al., 2021 *PASJ*, *73*, S1.
Galván-Madrid R. et al., 2007 *ApJ*, *670*, 1, 480.
Gammie C. F. et al., 2003 *ApJ*, *592*, 1, 203.
Garufi A. et al., 2022 *A&A*, *658*, A104.
Gaudel M. et al., 2020 *A&A*, *637*, A92.
Ginski C. et al., 2021 *ApJL*, *908*, 2, L25.
Goldsmith P. F. et al., 2008 *ApJ*, *680*, 428.
Gómez G. C. and Vázquez-Semadeni E., 2014 *ApJ*, *791*, 2, 124.
Gómez G. C. et al., 2018 *MNRAS*, *480*, 3, 2939.
Gómez G. C. et al., 2021 *MNRAS*, *502*, 4, 4963.
Gong H. and Ostriker E. C., 2011 *ApJ*, *729*, 2, 120.
Gong M. and Ostriker E. C., 2015 *ApJ*, *806*, 1, 31.
Gonzalez J.-F. et al., 2020 *MNRAS*, *499*, 3, 3837.
Goodman A. A. et al., 1993 *ApJ*, *406*, 528.
Goodman A. A. et al., 2009 *Nature*, *457*, 7225, 63.
Goodman A. A. et al., 2014 *ApJ*, *797*, 1, 53.
Goodwin S. P. et al., 2008 *A&A*, *477*, 3, 823.
Grady C. et al., 2001 *AAS Meeting Abstracts*, vol. 199, p. 60.15.
Grady C. A. et al., 1999 *ApJL*, *523*, 2, L151.

Gray W. J. et al., 2018 *MNRAS*, *473*, 2, 2124.
Gritschneder M. et al., 2017 *ApJ*, *834*, 2, 202.
Grudić M. Y. et al., 2021 *MNRAS*, *506*, 3, 3239.
Güdel M. et al., 2018 *A&A*, *620*, L1.
Hacar A. et al., 2013 *A&A*, *554*, A55.
Hacar A. et al., 2016 *A&A*, *587*, A97.
Hacar A. et al., 2017a *A&A*, *606*, A123.
Hacar A. et al., 2017b *A&A*, *602*, L2.
Hacar A. et al., 2018 *A&A*, *610*, A77.
Haid S. et al., 2019 *MNRAS*, *482*, 3, 4062.
Hanawa T. et al., 2017 *ApJ*, *848*, 1, 2.
Hanawa T. et al., 2019 *ApJ*, *881*, 2, 97.
Haugbølle T. et al., 2018 *ApJ*, *854*, 1, 35.
He C.-C. et al., 2019 *MNRAS*, *489*, 2, 1880.
Heigl S. et al., 2018 *MNRAS*, *474*, 4, 4881.
Heigl S. et al., 2020 *MNRAS*, *495*, 1, 758.
Heiles C., 1984 *ApJS*, *55*, 585.
Heitsch F., 2013a *ApJ*, *769*, 2, 115.
Heitsch F., 2013b *ApJ*, *776*, 1, 62.
Heitsch F. et al., 2009 *ApJ*, *695*, 1, 248.
Hennebelle P., 2013 *A&A*, *556*, A153.
Hennebelle P., 2018 *A&A*, *611*, A24.
Hennebelle P. and André P., 2013 *A&A*, *560*, A68.
Hennebelle P. and Inutsuka S.-i., 2019 *Front. Astron. Space Sci.*, *6*, 5.
Hennebelle P. et al., 2019 *ApJ*, *883*, 2, 140.
Hennebelle P. et al., 2020 *A&A*, *635*, A67.
Hennemann M. et al., 2012 *A&A*, *543*, L3.
Henshaw J. D. et al., 2014 *MNRAS*, *440*, 2860.
Heyer M. et al., 2008 *ApJ*, *680*, 1, 420.
Heyer M. et al., 2016 *MNRAS*, *461*, 4, 3918.
Heyer M. et al., 2020 *MNRAS*, *496*, 4, 4546.
Hirano S. et al., 2020 *ApJ*, *898*, 2, 118.
Hogge T. et al., 2018 *ApJS*, *237*, 2, 27.
Howard A. D. P. et al., 2019 *MNRAS*, *489*, 1, 962.
Hsieh C.-H. et al., 2021 *ApJ*, *908*, 1, 92.
Hsieh T.-H. et al., 2019 *ApJ*, *884*, 2, 149.
Huang J. et al., 2021 *ApJS*, *257*, 1, 19.
Hubber D. A. et al., 2013 *MNRAS*, *430*, 4, 3261.
Hull C. L. H. et al., 2013 *ApJ*, *768*, 2, 159.
Ikeda N. et al., 2007 *ApJ*, *665*, 2, 1194.
Inoue T. and Fukui Y., 2013 *ApJL*, *774*, 2, L31.
Inoue T. and Inutsuka S.-i., 2009 *ApJ*, *704*, 1, 161.
Inoue T. and Inutsuka S.-i., 2012 *ApJ*, *759*, 1, 35.
Inoue T. and Inutsuka S.-i., 2016 *ApJ*, *833*, 1, 10.
Inoue T. et al., 2018 *PASJ*, *70*, S53.
Inutsuka S.-i., 2001 *ApJL*, *559*, 2, L149.
Inutsuka S.-I. and Miyama S. M., 1992 *ApJ*, *388*, 392.
Inutsuka S.-i. and Miyama S. M., 1997 *ApJ*, *480*, 2, 681.
Inutsuka S.-i. et al., 2015 *A&A*, *580*, A49.
Jackson J. M. et al., 2019 *ApJ*, *870*, 1, 5.
Johnstone D. et al., 2001 *ApJ*, *559*, 1, 307.
Joos M. et al., 2012 *A&A*, *543*, A128.
Joos M. et al., 2013 *A&A*, *554*, A17.
Juvela M., 2016 *A&A*, *593*, A58.
Juvela M. et al., 2012 *A&A*, *541*, A12.
Kainulainen J. et al., 2013 *A&A*, *557*, A120.
Kainulainen J. et al., 2017 *A&A*, *600*, A141.
Kalberla P. M. W. et al., 2016 *ApJ*, *821*, 2, 117.
Kalberla P. M. W. et al., 2017 *A&A*, *607*, A15.
Kamann S. et al., 2019 *MNRAS*, *483*, 2, 2197.
Kandori R. et al., 2020 *ApJ*, *900*, 1, 20.
Kashiwagi R. and Tomisaka K., 2021 *ApJ*, *911*, 2, 106.
Kauffmann J. et al., 2013 *ApJ*, *779*, 2, 185.
Keown J. et al., 2016 *ApJ*, *833*, 1, 97.
Keown J. et al., 2017 *ApJ*, *850*, 1, 3.
Keown J. et al., 2019 *ApJ*, *884*, 1, 4.
Kerr R. et al., 2019 *ApJ*, *874*, 2, 147.
Keto E. et al., 2015 *MNRAS*, *446*, 4, 3731.
Kim C.-G. and Ostriker E. C., 2018 *ApJ*, *853*, 2, 173.
Kirk H. et al., 2007 *ApJ*, *668*, 2, 1042.
Kirk H. et al., 2013a *ApJ*, *766*, 2, 115.
Kirk H. et al., 2015 *ApJ*, *802*, 2, 75.
Kirk H. et al., 2016 *ApJ*, *817*, 2, 167.
Kirk H. et al., 2017a *ApJ*, *838*, 2, 114.
Kirk H. et al., 2017b *ApJ*, *846*, 2, 144.
Kirk J. M. et al., 2013b *MNRAS*, *432*, 2, 1424.
Kitsionas S. and Whitworth A. P., 2007 *MNRAS*, *378*, 2, 507.
Koch E. W. and Rosolowsky E. W., 2015 *MNRAS*, *452*, 4, 3435.
Kong S. et al., 2018 *ApJS*, *236*, 2, 25.
Kong S. et al., 2019 *ApJ*, *874*, 1, 104.
Könyves V. et al., 2015 *A&A*, *584*, A91.
Könyves V. et al., 2020 *A&A*, *635*, A34.
Koumpia E. et al., 2020 *A&A*, *643*, A61.
Kovacs G., 2018 *A&A*, *612*, L2.
Kramer C. et al., 1998 *A&A*, *329*, 249.
Krumholz M. R. et al., 2013 *ApJL*, *767*, 1, L11.
Krumholz M. R. et al., 2014 *Protostars and Planets VI* (H. Beuther, R. S. Klessen, C. P. Dullemond, and T. Henning), p. 243.
Kuffmeier M. et al., 2016 *ApJ*, *826*, 1, 22.
Kuffmeier M. et al., 2017 *ApJ*, *846*, 1, 7.
Kuffmeier M. et al., 2018 *MNRAS*, *475*, 2, 2642.
Kuffmeier M. et al., 2019 *A&A*, *628*, A112.
Kuffmeier M. et al., 2020a *A&A*, *639*, A86.
Kuffmeier M. et al., 2020b *A&A*, *633*, A3.
Kuffmeier M. et al., 2021 *A&A*, *656*, A161.
Kumar M. S. N. et al., 2020 *A&A*, *642*, A87.
Kumar M. S. N. et al., 2022 *A&A*, *658*, A114.
Kurono Y. et al., 2013 *ApJ*, *765*, 2, 85.
Kuznetsova A. et al., 2018 *ApJ*, *868*, 1, 50.
Kuznetsova A. et al., 2019 *ApJ*, *876*, 1, 33.
Kuznetsova A. et al., 2020 *ApJ*, *893*, 1, 73.
Kuznetsova A. et al., 2022 *arXiv e-prints*, arXiv:2202.05301.
Lada C. J., 1987 *Star Forming Regions*, vol. 115 (M. Peimbert and J. Jugaku), p. 1.
Ladd E. F. et al., 1991 *ApJ*, *382*, 555.
Ladjelate B. et al., 2020 *A&A*, *638*, A74.
Lam K. H. et al., 2019 *MNRAS*, *489*, 4, 5326.
Lane J. et al., 2016 *ApJ*, *833*, 1, 44.
Larson R. B., 1969 *MNRAS*, *145*, 271.
Lazarian A. and Vishniac E. T., 1999 *ApJ*, *517*, 2, 700.
Le Gouellec V. J. M. et al., 2019 *ApJ*, *885*, 2, 106.
Lebreuilly U. et al., 2021 *ApJL*, *917*, 1, L10.
Lee C.-F. et al., 2014a *ApJ*, *786*, 2, 114.
Lee C. W. and Myers P. C., 2011 *ApJ*, *734*, 1, 60.
Lee C. W. et al., 1999 *ApJ*, *526*, 2, 788.
Lee C. W. et al., 2004 *ApJS*, *153*, 2, 523.
Lee K. I. et al., 2014b *ApJ*, *797*, 2, 76.
Lee Y.-N. and Hennebelle P., 2016 *A&A*, *591*, A30.
Lee Y.-N. and Hennebelle P., 2018 *A&A*, *611*, A88.
Lee Y.-N. et al., 2017 *ApJ*, *847*, 2, 114.
Lee Y.-N. et al., 2021 *A&A*, *648*, A101.
Lesur G. et al., 2015 *A&A*, *582*, L9.

Leung C. M. and Brown R. L., 1977 *ApJL*, *214*, L73.
Li D. and Goldsmith P. F., 2012 *ApJ*, *756*, 12.
Li P. S. and Klein R. I., 2019 *MNRAS*, *485*, 4, 4509.
Li P. S. et al., 2015 *MNRAS*, *452*, 3, 2500.
Li P. S. et al., 2022 *MNRAS*, *510*, 4, 6085.
Li Z.-Y. et al., 2014a *ApJ*, *793*, 2, 130.
Li Z. Y. et al., 2014b *Protostars and Planets VI* (H. Beuther, R. S. Klessen, C. P. Dullemond, and T. Henning), p. 173.
Liu T. et al., 2020 *MNRAS*, *496*, 3, 2790.
Liu X.-L. et al., 2021 *A&A*, *646*, A137.
Machida M. N. and Basu S., 2019 *ApJ*, *876*, 2, 149.
Malinen J. et al., 2016 *MNRAS*, *460*, 2, 1934.
Marchand P. et al., 2020 *ApJ*, *900*, 2, 180.
Mardones D. et al., 1997 *ApJ*, *489*, 2, 719.
Marino S. et al., 2015 *ApJL*, *798*, L44.
Marsh K. A. et al., 2014 *MNRAS*, *439*, 4, 3683.
Marsh K. A. et al., 2016 *MNRAS*, *459*, 1, 342.
Masson J. et al., 2016 *A&A*, *587*, A32.
Matsumoto T. et al., 2015 *ApJ*, *801*, 2, 77.
Matsumoto T. et al., 2017 *ApJ*, *839*, 1, 69.
Mattern M. et al., 2018 *A&A*, *619*, A166.
Maureira M. J. et al., 2017 *ApJ*, *838*, 1, 60.
Maury A. J. et al., 2010 *A&A*, *512*, A40.
Maury A. J. et al., 2019 *A&A*, *621*, A76.
McClure-Griffiths N. M. et al., 2006 *ApJ*, *652*, 1339.
McKee C. F. and Ostriker E. C., 2007 *ARA&A*, *45*, 1, 565.
Men'shchikov A., 2013 *A&A*, *560*, A63.
Men'shchikov A., 2021 *A&A*, *649*, A89.
Men'shchikov A. et al., 2012 *A&A*, *542*, A81.
Mignon-Risse R. et al., 2021 *A&A*, *652*, A69.
Misugi Y. et al., 2019 *ApJ*, *881*, 1, 11.
Miville-Deschênes M.-A. et al., 2010 *A&A*, *518*, L104.
Miville-Deschênes M.-A. et al., 2016 *A&A*, *593*, A4.
Moeckel N. and Burkert A., 2015 *ApJ*, *807*, 1, 67.
Molinari S. et al., 2010 *PASP*, *122*, 889, 314.
Molinari S. et al., 2011 *A&A*, *530*, A133.
Molinari S. et al., 2016 *A&A*, *591*, A149.
Monsch K. et al., 2018 *ApJ*, *861*, 2, 77.
Motte F. et al., 1998 *A&A*, *336*, 150.
Motte F. et al., 2018 *ARA&A*, *56*, 41.
Mottram J. C. et al., 2017 *A&A*, *600*, A99.
Mowat C. et al., 2017 *MNRAS*, *467*, 1, 812.
Murillo N. M. et al., 2022 *A&A*, *658*, A53.
Myers P. C., 2009 *ApJ*, *700*, 2, 1609.
Nagai T. et al., 1998 *ApJ*, *506*, 1, 306.
Nagasawa M., 1987 *Progress of Theoretical Physics*, *77*, 3, 635.
Nakamura F. et al., 2017 *ApJ*, *837*, 2, 154.
Naranjo-Romero R. et al., 2015 *ApJ*, *814*, 1, 48.
Nealon R. et al., 2020a *MNRAS*, *491*, 3, 4108.
Nealon R. et al., 2020b *MNRAS*, *499*, 3, 3857.
Nixon C. et al., 2012 *ApJL*, *757*, 2, L24.
Nony T. et al., 2021 *A&A*, *645*, A94.
Ntormousi E. and Hennebelle P., 2019 *A&A*, *625*, A82.
Ntormousi E. et al., 2011 *ApJ*, *731*, 1, 13.
Nutter D. and Ward-Thompson D., 2007 *MNRAS*, *374*, 4, 1413.
Offner S. S. R. et al., 2010 *ApJ*, *725*, 2, 1485.
Offner S. S. R. et al., 2012 *MNRAS*, *420*, 1, L53.
Ohashi N. et al., 2014 *ApJ*, *796*, 2, 131.
Orkisz J. H. et al., 2019 *A&A*, *624*, A113.
Ortiz-León G. N. et al., 2018 *ApJL*, *869*, 2, L33.
Ostriker J., 1964 *ApJ*, *140*, 1056.
Padoan P. and Nordlund Å., 1999 *ApJ*, *526*, 1, 279.
Padoan P. et al., 2001 *ApJ*, *553*, 1, 227.
Padoan P. et al., 2007 *ApJ*, *661*, 2, 972.
Padoan P. et al., 2016 *ApJ*, *822*, 1, 11.
Padoan P. et al., 2017 *ApJ*, *840*, 1, 48.
Padoan P. et al., 2020 *ApJ*, *900*, 1, 82.
Palmeirim P. et al., 2013 *A&A*, *550*, A38.
Palmeirim P. et al., 2017 *A&A*, *605*, A35.
Panopoulou G. V. et al., 2014 *MNRAS*, *444*, 2507.
Panopoulou G. V. et al., 2017 *MNRAS*, *466*, 2529.
Panopoulou G. V. et al., 2022 *A&A*, *657*, L13.
Pattle K., 2016 *MNRAS*, *459*, 3, 2651.
Pattle K. and Fissel L., 2019 *Front. Astron. Space Sci.*, *6*, 15.
Pattle K. et al., 2015 *MNRAS*, *450*, 1, 1094.
Pelkonen V. M. et al., 2021 *MNRAS*, *504*, 1, 1219.
Penston M. V., 1969 *MNRAS*, *144*, 425.
Peretto N. et al., 2006 *A&A*, *445*, 3, 979.
Peretto N. et al., 2014 *A&A*, *561*, A83.
Pezzuto S. et al., 2021 *A&A*, *645*, A55.
Pfalzner S., 2003 *ApJ*, *592*, 2, 986.
Pilbratt G. L. et al., 2010 *A&A*, *518*, L1.
Pillai T. G. S. et al., 2020 *Nature Astronomy*, *4*, 1195.
Pineda J. E. et al., 2010 *ApJL*, *712*, 1, L116.
Pineda J. E. et al., 2011 *ApJL*, *739*, L2.
Pineda J. E. et al., 2012 *A&A*, *544*, L7.
Pineda J. E. et al., 2015 *Nature*, *518*, 7538, 213.
Pineda J. E. et al., 2019 *ApJ*, *882*, 2, 103.
Pineda J. E. et al., 2020 *Nature Astronomy*, *4*, 1158.
Pineda J. E. et al., 2021 *ApJ*, *912*, 1, 7.
Pinte C. et al., 2022 *arXiv e-prints*, arXiv:2203.09528.
Pirogov L. et al., 2003 *A&A*, *405*, 639.
Planck Collaboration Int. XXXII, 2016 *A&A*, *586*, A135.
Planck Collaboration Int. XXXIII, 2016 *A&A*, *586*, A136.
Planck Collaboration Int. XXXV, 2016 *A&A*, *586*, A138.
Plunkett A. L. et al., 2018 *A&A*, *615*, A9.
Pokhrel R. et al., 2018 *ApJ*, *853*, 1, 5.
Pon A. et al., 2012 *ApJ*, *756*, 2, 145.
Priestley F. D. and Whitworth A. P., 2020 *MNRAS*, *499*, 3, 3728.
Pudritz R. E. and Kevlahan N. K. R., 2013 *RSPTA*, *371*, 2003, 20120248.
Pudritz R. E. and Ray T. P., 2019 *Front. Astron. Space Sci.*, *6*, 54.
Ragan S. E. et al., 2014 *A&A*, *568*, A73.
Rathjen T.-E. et al., 2021 *MNRAS*, *504*, 1, 1039.
Recchi S. et al., 2014 *MNRAS*, *444*, 2, 1775.
Redaelli E. et al., 2017 *ApJ*, *850*, 2, 202.
Reipurth B. et al., 2014 *Protostars and Planets VI* (H. Beuther, R. S. Klessen, C. P. Dullemond, and T. Henning), p. 267.
Rey-Raposo R. and Read J. I., 2018 *MNRAS*, *481*, 1, L16.
Rice T. S. et al., 2016 *ApJ*, *822*, 1, 52.
Rivera-Ingraham A. et al., 2016 *A&A*, *591*, A90.
Robitaille J. F. et al., 2018 *A&A*, *617*, A101.
Rosolowsky E. and Leroy A., 2006 *PASP*, *118*, 842, 590.
Rosolowsky E. W. et al., 2008 *ApJ*, *679*, 2, 1338.
Roy A. et al., 2019 *A&A*, *626*, A76.
Sadavoy S. I. et al., 2013 *ApJ*, *767*, 2, 126.
Sahu D. et al., 2021 *ApJL*, *907*, 1, L15.
Sakai N. et al., 2014 *Nature*, *507*, 7490, 78.
Salji C. J. et al., 2015 *MNRAS*, *449*, 2, 1782.
Salpeter E. E., 1955 *ApJ*, *121*, 161.
Samal M. R. et al., 2018 *A&A*, *617*, A67.
Sanhueza P. et al., 2019 *ApJ*, *886*, 2, 102.
Santos-Lima R. et al., 2013 *MNRAS*, *429*, 4, 3371.
Schisano E. et al., 2014 *ApJ*, *791*, 27.

Schmidt W. et al., 2010 *A&A*, *516*, A25.
Schmiedeke A. et al., 2021 *ApJ*, *909*, 1, 60.
Schnee S. et al., 2010 *ApJ*, *718*, 1, 306.
Schuller F. et al., 2021 *A&A*, *651*, A36.
Segura-Cox D. M. et al., 2018 *ApJ*, *866*, 2, 161.
Segura-Cox D. M. et al., 2020 *Nature*, *586*, 7828, 228.
Segura-Cox D. M. et al., 2022 *In prep.*
Seifried D. and Walch S., 2015 *MNRAS*, *452*, 3, 2410.
Seifried D. et al., 2012 *MNRAS*, *423*, 1, L40.
Seifried D. et al., 2013 *MNRAS*, *432*, 4, 3320.
Seifried D. et al., 2015 *MNRAS*, *446*, 3, 2776.
Seo Y. M. et al., 2015 *ApJ*, *805*, 2, 185.
Shimajiri Y. et al., 2014 *A&A*, *564*, A68.
Shimajiri Y. et al., 2019a *A&A*, *623*, A16.
Shimajiri Y. et al., 2019b *A&A*, *632*, A83.
Shirley Y. L., 2015 *PASP*, *127*, 949, 299.
Shu F. H., 1977 *ApJ*, *214*, 488.
Shu F. H. et al., 1987 *ARA&A*, *25*, 23.
Singh A. et al., 2019 *ApJ*, *878*, 1, 22.
Singh A. et al., 2021 *ApJ*, *922*, 1, 87.
Smallwood J. L. et al., 2021 *MNRAS*, *508*, 1, 392.
Smith R. J. et al., 2009 *MNRAS*, *396*, 2, 830.
Smith R. J. et al., 2014 *MNRAS*, *445*, 3, 2900.
Smith R. J. et al., 2016 *MNRAS*, *455*, 4, 3640.
Smullen R. A. et al., 2020 *MNRAS*, *497*, 4, 4517.
Sohn J. et al., 2007 *ApJ*, *664*, 2, 928.
Sokolov V. et al., 2018 *A&A*, *611*, L3.
Soler J. D. and Hennebelle P., 2017 *A&A*, *607*, A2.
Soler J. D. et al., 2016 *A&A*, *596*, A93.
Soler J. D. et al., 2020 *A&A*, *642*, A163.
Solomon P. M. et al., 1987 *ApJ*, *319*, 730.
Sousbie T., 2011 *MNRAS*, *414*, 1, 350.
Spitzer L., 1978 *Physical processes in the interstellar medium*.
Stephens I. W. et al., 2017 *ApJ*, *846*, 1, 16.
Stodólkiewicz J. S., 1963 *AcA*, *13*, 30.
Storm S. et al., 2014 *ApJ*, *794*, 2, 165.
Storm S. et al., 2016 *ApJ*, *830*, 2, 127.
Su Y.-N. et al., 2019 *ApJ*, *885*, 2, 98.
Suri S. et al., 2019 *A&A*, *623*, A142.
Tafalla M. and Hacar A., 2015 *A&A*, *574*, A104.
Tahani M. et al., 2018 *A&A*, *614*, A100.
Tahani M. et al., 2019 *A&A*, *632*, A68.
Takahashi S. et al., 2013 *ApJ*, *763*, 57.
Takahashi S. Z. et al., 2016 *MNRAS*, *463*, 2, 1390.
Takemura H. et al., 2021 *PASJ*.
Tatematsu K. et al., 2016 *PASJ*, *68*, 2, 24.
Teixeira P. S. et al., 2016 *A&A*, *587*, A47.
Terebey S. et al., 1984 *ApJ*, *286*, 529.
Thieme T. J. et al., 2022 *ApJ*, *925*, 1, 32.
Tobin J. J. et al., 2010 *ApJ*, *712*, 2, 1010.
Tobin J. J. et al., 2011 *ApJ*, *740*, 1, 45.
Tobin J. J. et al., 2018 *ApJ*, *856*, 2, 164.
Tokuda K. et al., 2014 *ApJL*, *789*, 1, L4.
Tokuda K. et al., 2020 *ApJ*, *899*, 1, 10.
Tomida K. et al., 2015 *ApJ*, *801*, 2, 117.
Tomisaka K., 2014 *ApJ*, *785*, 1, 24.
Tomisaka K. and Ikeuchi S., 1983 *PASJ*, *35*, 2, 187.
Tomisaka K. et al., 1981 *Ap&SS*, *78*, 2, 273.
Traficante A. et al., 2018a *MNRAS*, *473*, 4, 4975.
Traficante A. et al., 2018b *MNRAS*, *477*, 2, 2220.
Treviño-Morales S. P. et al., 2019 *A&A*, *629*, A81.
Tritsis A. and Tassis K., 2016 *MNRAS*, *462*, 4, 3602.
Tsitali A. E. et al., 2013 *A&A*, *557*, A98.
Tsitali A. E. et al., 2015 *A&A*, *575*, A27.
Tsukamoto Y. et al., 2018 *ApJ*, *868*, 1, 22.
Umemoto T. et al., 2017 *PASJ*, *69*, 5, 78.
Urquhart J. S. et al., 2014 *MNRAS*, *443*, 2, 1555.
Vaidya B. et al., 2013 *MNRAS*, *433*, 2, 1258.
Valdivia-Mena M. T. et al., 2022 *Sub.*
Van Loo S. et al., 2014 *ApJ*, *789*, 1, 37.
Vázquez-Semadeni E. et al., 2017 *MNRAS*, *467*, 2, 1313.
Vázquez-Semadeni E. et al., 2019 *MNRAS*, *490*, 3, 3061.
Verliat A. et al., 2020 *A&A*, *635*, A130.
Vestuto J. G. et al., 2003 *ApJ*, *590*, 2, 858.
Vorobyov E. I. et al., 2015 *A&A*, *573*, A5.
Vorobyov E. I. et al., 2017 *A&A*, *608*, A107.
Walch S. et al., 2010 *MNRAS*, *402*, 4, 2253.
Walch S. et al., 2012 *MNRAS*, *419*, 1, 760.
Wang J.-W. et al., 2020a *ApJ*, *905*, 2, 158.
Wang J.-W. et al., 2020b *ApJ*, *888*, 1, 13.
Ward-Thompson D. et al., 2007 *PASP*, *119*, 858, 855.
Ward-Thompson D. et al., 2016 *MNRAS*, *463*, 1, 1008.
Wareing C. J. et al., 2016 *MNRAS*, *459*, 2, 1803.
Wareing C. J. et al., 2019 *MNRAS*, *485*, 4, 4686.
White G. J. et al., 2015 *MNRAS*, *447*, 2, 1996.
Whitworth A. and Summers D., 1985 *MNRAS*, *214*, 1.
Williams G. M. et al., 2018 *A&A*, *613*, A11.
Williams J. P. et al., 1994 *ApJ*, *428*, 693.
Wu B. et al., 2017 *ApJ*, *835*, 2, 137.
Wurster J. and Lewis B. T., 2020 *MNRAS*, *495*, 4, 3795.
Wurster J. et al., 2016 *MNRAS*, *457*, 1, 1037.
Wurster J. et al., 2018 *MNRAS*, *476*, 2, 2063.
Xu J.-L. et al., 2017 *Ap&SS*, *362*, 9, 175.
Xu J.-L. et al., 2018 *A&A*, *609*, A43.
Xu S. et al., 2019 *ApJ*, *878*, 2, 157.
Yang Y.-L. et al., 2020 *ApJ*, *891*, 1, 61.
Yen H.-W. et al., 2010 *ApJ*, *710*, 2, 1786.
Yen H.-W. et al., 2011 *ApJ*, *742*, 1, 57.
Yen H.-W. et al., 2013 *ApJ*, *772*, 1, 22.
Yen H.-W. et al., 2015a *ApJ*, *812*, 2, 129.
Yen H.-W. et al., 2015b *ApJ*, *799*, 2, 193.
Yen H.-W. et al., 2017 *ApJ*, *834*, 2, 178.
Yen H.-W. et al., 2019 *ApJ*, *880*, 2, 69.
Ysard N. et al., 2013 *A&A*, *559*, A133.
Yuan L. et al., 2020 *A&A*, *637*, A67.
Zamora-Avilés M. et al., 2017 *MNRAS*, *472*, 1, 647.
Zavagno A. et al., 2010 *A&A*, *518*, L81.
Zavagno A. et al., 2020 *A&A*, *638*, A7.
Zernickel A. et al., 2013 *A&A*, *554*, L2.
Zhang G.-Y. et al., 2020a *A&A*, *642*, A76.
Zhang S. et al., 2018 *MNRAS*, *480*, 4, 5495.
Zhang S. et al., 2020b *A&A*, *637*, A40.
Zhang S. et al., 2021 *A&A*, *646*, A25.
Zhao B. et al., 2016 *MNRAS*, *460*, 2, 2050.
Zhao B. et al., 2018 *MNRAS*, *473*, 4, 4868.
Zucker C. and Chen H. H.-H., 2018 *ApJ*, *864*, 2, 152.
Zucker C. et al., 2015 *ApJ*, *815*, 1, 23.
Zurlo A. et al., 2021 *ApJ*, *912*, 1, 64.